Liquid Impingement Erosion Performance

of

Low Plasticity Burnished Ti6Al4V

Dina Ma

A Thesis

in

The Department

of

Mechanical and Industrial Engineering

Presented in Partial Fulfillment of Requirements

for the Degree of the Master of Applied Science (Mechanical Engineering) at

Concordia University Montreal, Quebec, Canada

June, 2014

CONCORDIA UNIVERSITY

School of Graduate Studies

This is to certify that the thesis prepared

By: Dina Ma

Entitled: Liquid Impingement Erosion Performance of Low Plasticity Burnished Ti6Al4V

and submitted in partial fulfillment of the requirements for the degree of

Master of Applied Science (Mechanical Engineering)

complies with the regulations of the University and meets the accepted standards with respect to originality and quality.

Signed by the final examining committee:

Dr. L. Kadem Chair

Dr. S. Durham Examiner

Dr. S. Narayanswamy Examiner

Dr. M. Medraj, Dr. M. Pugh Supervisor

Approved by _____

Chair of Department or Graduate Program Director

_____

Dean of Faculty

Date: _____

Abstract

In power generation industry, inlet fog cooling is used for the turbine inlet cooling (TIC). However, this approach also leads to liquid impingement erosion (LIE) of the rotating blades in the compressor, resulting in performance degradation and reduction of service life of gas turbines.

Previous studies have introduced Laser shock peening (LSP) and shot peening (SP) as potential solutions for LIE of Ti64. However, no study has been done on the LIE performance of the low plasticity burnished Ti64.

Full factorial design of experiments was conducted to investigate the effects of LPB process parameters (Feed Rate, Spindle Velocity, Number of Passes, Pressure) on the residual stress distribution, microhardness and surface roughness of Ti64. The surface microhardness and the surface roughness of the Ti64 were improved after the LPB treatment. Moreover, a large magnitude of compressive residual stress layer was induced by LPB treatment on the surface of the Ti64. However, the results of the LIE tests showed that LPB treatment has little or no effect on the LIE performance of Ti64.

Acknowledgements

I would like to express my sincere gratitude and appreciation to my thesis supervisors Dr. Mamoun Medraj and Dr. Martin Pugh for their time, suggestions, support and encouragements during my MASc project at Concordia University.

My sincere thanks also goes to Dr. Dmytro Kevorko, Dr. Yasser El-Shaer, Mazen Samara and Robert Oliver for their supports and help throughout my experimental work.

I would like to thank all the TMG group members, particularly Ahmad Mostafa, Yi Jie, Bolariewa Komolafe, Guy-Joel Rocher, and Hany Kiros for their constant help and suggestions during my research and thesis revision.

In addition, financial support from NSERC through a CRIAQ-Rolls Royce project is gratefully acknowledged.

I would also like to thank all my friends for their support and encouragement.

Last but not least, special love and gratitude goes to my family for all of the sacrifices that they have made on my behalf. I would never have been able to stand at this point of my life without their unwavering love, endless support and devoted encouragement.

Table of Contents

List of Figures

List of Tables

Chapter 1

Introduction

Gas turbines suffer from both decreasing output power and efficiency as the ambient temperature increases because the air becomes less dense (which results in less mass flow rate). Gas turbine inlet air fog cooling is considered as a cost-effective solution [1]. Fog cooling is done by spraying micro-scale water droplets into the gas turbine inlet [2]. Some of the droplets, through evaporation, absorb heat from the air, while the remaining droplets enter the compressor as overspray, which leads to further cooling of the compressor [1]. However, this particular approach causes Liquid Impingement Erosion (LIE) of the compressor blades, as shown in Figure 1-1 [3], resulting in performance degradation and a reduction in service life of the compressor blades.

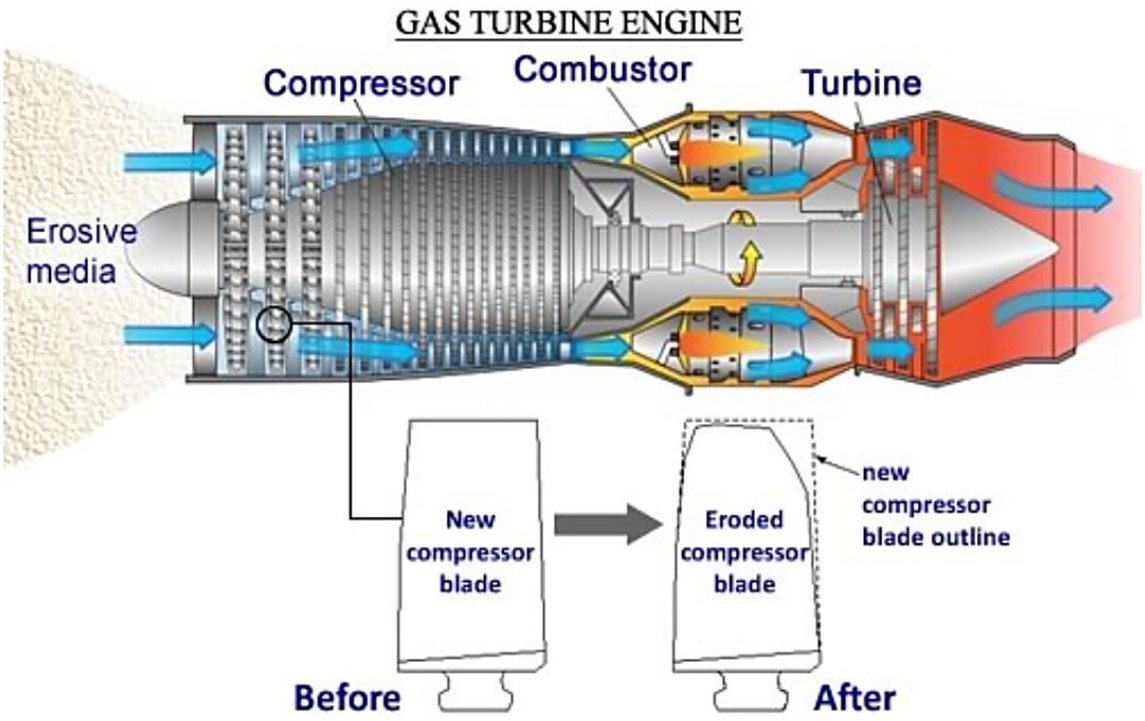

Figure 1-1 Gas Turbine Engine [3].

This study will look at current methods used to improve LIE resistance and the potential of low plasticity burnishing to reduce the compressor blade erosion. The objective will be to study the parameter of LPB and design a process which can later be tested for its use in improving LIE performance.

Chapter 2
Literature Review

2.1 Turbine inlet cooling and droplet-induced erosion

2.1.1 Turbine inlet cooling

In the power generation industry, ambient air temperature plays a very important role in the performance of gas turbines. Meher-Homji *et al.* [1] found that, 1°F increase in the ambient temperature leads to 0.3-0.5% decrease in the gas turbine output power. This particular correlation between the output power of a gas turbine and the ambient temperature was also confirmed by the U.S. Department of Energy [4]. They reported a loss of 9% in the output capacity of gas turbines in the summer time, when there is a relatively higher ambient temperature, compared to that of the winter time. This was attributed to the decrease in the air density commensurate with an increase in the ambient temperature [2]. Thus, the actual mass of intake air decreases, since each gas turbine is designed to intake a fixed volume of air [2]. As a result, the gas turbine efficiency and the output power capacity decrease [2].

Therefore, there is a need for turbine inlet cooling (TIC); to cool the intake air before it enters into the turbine compressor. Inlet fog cooling is the most popular method being used since it has been proven to be the most effective method, cost-wise [5]. During the fog cooling process, as shown in Figure 2-1 [5], micro-scale water droplets are sprayed into the turbine inlet and they absorb the heat from the air by evaporation. Some of the droplets do not evaporate and they enter into the compressor (overspray) with the air, leading to further cooling [1]. However, this approach also leads to liquid impingement erosion (LIE) of the rotating blades in the compressor, resulting in performance degradation and reduction in service life of the compressor blades [6, 7].

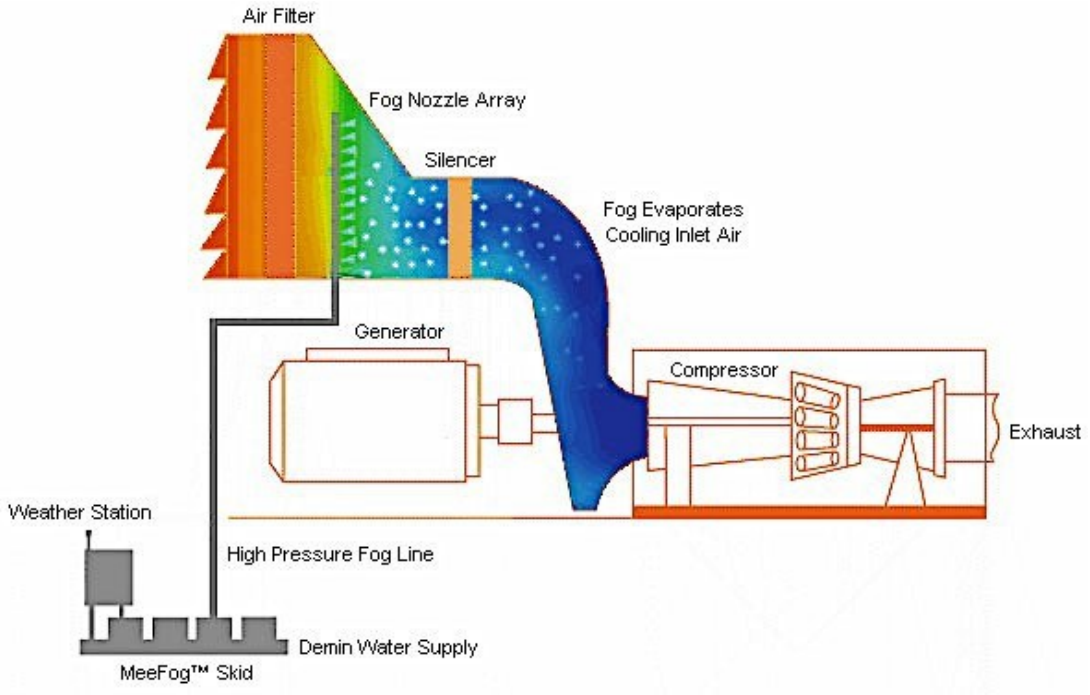

Figure 2-1 Image of typical gas turbine inlet cooling (TIC) [5].

2.1.2 Liquid impingement erosion (LIE) mechanism

Thus far, LIE has been treated as a purely mechanical phenomenon [8]. Several theories [8–11] have been put forward to understand LIE damage. Most of these theories are based on the concept of water-hammer pressure and shock wave propagation. Water-hammer pressure refers to the high pressure generated as a result of the collision of high velocity water droplets with the target solid surface, coupled with the compressibility of the liquid droplet [11]. The high velocity impacts of the water droplets develop stress concentrations in the solid workpiece. Thus, stress waves are induced and transmitted beneath the target surface [9, 11].

Generally, the evolution of LIE damage follows its initiation by a ductile fracture mechanism (microvoid nucleation, growth and coalescence). A general description of the erosion damage is illustrated in Figure 2-2 [12]. It is mainly divided into 4 stages: surface

roughening, formation of small pits and micro cracks, crack propagation and formation of larger pits, and material removal.

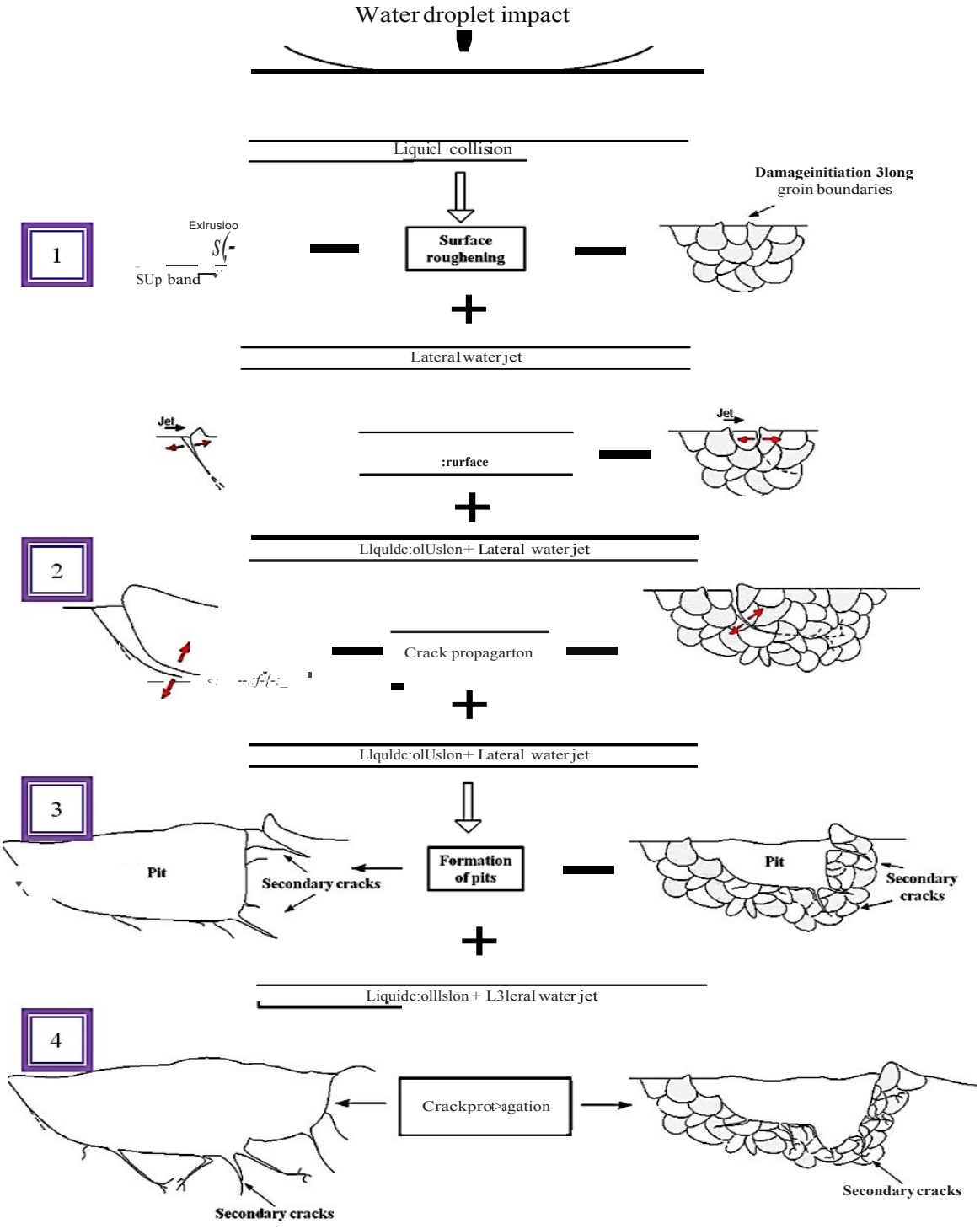

Figure 2-2 The mechanism of LIE material removal [12].

Surfaces are usually roughened due to the collision with water droplets, forming what are called slip bands. Adler [13] linked this behavior to the formation of surface depressions upon impact of the water droplets, extruding part of the surface around the impact zone; hence, increasing the surface roughness.

Jolliffe [14] also explained the formation of the slip bands with the aid of a schematic diagram shown in Figure 2-3. Water droplets impacting a previously formed depression induce a water hammer pressure inside the crater. As the compressed liquid moves, it pushes the edges of the depression causing their plastic deformation in the form of extruded (emerging) edges.

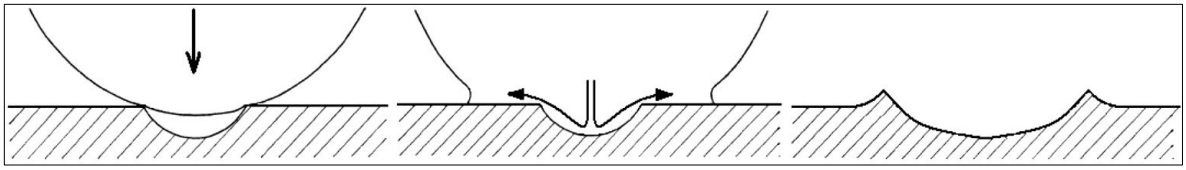

Figure 2-3 Formation of the slip band [14].

As the slip bands are formed, lateral jet pressure acts to initiate microcracks on the rough surface, as shown in stage 1 of Figure 2-2. As a result of stress wave propagation in the specimen, it forms micro- and macrocracks (Meng *et al.,* 1998) [15]. This can be attributed to the abundance of stress concentration locations on the surface which lead to the formation of more surface microcracks upon successive water droplets impingements. Cracks start to propagate along grain boundaries as described in stage 2 of Figure 2-2.

As the surface cracks merge, unsupported material particulates that detach from the specimen forming larger pits are created as illustrated in stage 3 in Figure 2-2. Further impingements acting on the fracture surface initiate more microcracks known as secondary microcracks. Due to the increased surface roughness, more stress concentration locations are present as sketched in stage 4 in Figure 2-2.

Experimental evidences [10, 14, 15] indicate that, under a wide range of LIE conditions, the weight loss of a material subjected to repeated impingements of liquid droplets varies with time (erosion rate) as shown in Figure 2-4 [8]. The evolution of LIE could be divided into 5 stages. In sequential order they are: "incubation period, acceleration period, maximum rate period, deceleration period and terminal period" [8]. The description of the stages is as follows:

① Incubation period: In this stage, there is negligible material loss. However, this period may not appear if the impact conditions are too severe.

② Acceleration period: It is characterized by rapid increase in erosion rate to a maximum value.

③ Maximum rate period: The erosion rate, in this period, remains relatively constant.

④ Deceleration period: During this stage, the erosion rate declines to (normally) 1/4 to 1/2 of the maximum rate.

⑤ Terminal period: This is the last stage of the evolution of LIE. The erosion rate is expected to remain constant, once again, indefinitely. However, in some cases, the erosion rate fluctuates in this stage.

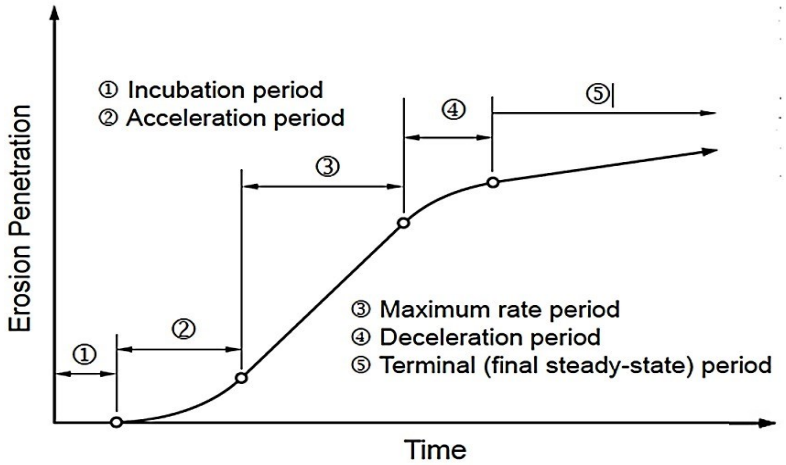

Figure 2-4 LIE damage stages [8].

2.1.3 Factors affecting Liquid impingement erosion (LIE)

LIE of the compressor blades of gas turbines is a very complex mechanical phenomenon and is significantly affected by many parameters such as: impact velocity, impact angle, droplet size, droplet shape, frequency of impacts, and impingement resistance of target material [16–23].

1) Impact velocity

The impact velocity is defined as the relative velocity between droplets and rotating blades, which is the vector sum of the absolute droplet velocity and the peripheral rotational velocity of the blades [13, 17].

Impact velocity is one of the most important parameters that significantly affect the erosion rate; their relation could be demonstrated by a Power Law equation of the form:

$$E \equiv V^n \tag{1}$$

where E is erosion rate, V is impact velocity, and n is a material dependent constant. For Ti64 alloy, n was reported about 7 [16, 21].

2) Impact angle

Impact angle is another important parameter affecting LIE. Ahmad [27] reported that maximum erosion occurs at an impact angle of 90°. When the impact angle deviates from the normal direction, the erosion rate will be affected due to the decrease of the normal impact velocity. However, the impact angle, to some extent, has been regarded as an unstable parameter in the literature, due to the continuous change of the surface roughness during the impingement process [6, 8].

3) Droplet size

Droplet size is another important parameter that significantly affects the LIE. Wang *et al.* [28] found that the cooling effectiveness tends to decrease when the droplet diameter is larger than 50 μm. Also, large droplets with high kinetic energy impact the leading edge of the compressor blade [20], causing increased erosion rate and more severe crater and pitting damage on the blades, especially on the blades tips [29]. The use of smaller primary droplets with a typical size of 5 to 10 μm is a common practice not only to improve the cooling effectiveness but also to reduce the water droplet erosion [28].

4) Droplet shape

The injection force, the gravity, and the reaction force, upon collision, could affect the actual shape of the water droplets, making them not to be perfect spheres. This might affect the LIE. A flattened droplet, with a larger equivalent diameter, has been proven to be more damaging, because it behaves effectively as a larger droplet [30]. This indicates the importance of studying the effect of the shape of the impacting droplets. However, in this work care is taken to assure as uniform droplets as possible.

2.1.4 Potential mechanical surface treatment solutions for LIE

Studies have not yet successfully correlated LIE resistance with any independent measurable material property [30]. Rather, it depends on a combination of properties whose relative importance may differ depending on the variables, such as the nature of the substrates and erosion conditions [28–30].

Surface treatments, such as shot peening (SP), could be a reference for a potential solution to LIE. SP is one of the most widely-used surface treatments, which introduces a

high magnitude of local residual stress with high percentage of cold work by bombarding the surface of the material with solid particles. It enhances the fatigue life of the materials, but it entails high cold work percentage and produces a rough surface finish, which might not be beneficial for LIE resistance [31, 32].

Laser shock peening (LSP) is another widely-used technique to enhance the properties of the material, such as fatigue life [36]. Since the process involves the usage of laser technology, the cost is relatively high and the processing time is long. Robinson *et al.* [37] applied LSP to Ti64 to study its LIE performance. For the tests, they [37] used an impulsive water jet that produced 100-micron droplets size at an impact speed of 500m/s, and the total test period was 25 hours. The results showed an improvement of 20-25% in mass loss, compared to the untreated samples under the same erosion condition. The improvement was attributed to the combined effects of the existence of 400μm depth homogeneous martensitic (α') microstructure on the surface of Ti64, and an up to 10% increase in micro-hardness.

Low Plasticity Burnishing (LPB) is another important surface enhancement technique. Improvement of both high cycle and low cycle fatigue life is the most popular application of LPB [33, 35–37]. However, its effectiveness in LIE is yet to be established. The details of LPB will be discussed in the following section.

2.2 Low plasticity burnishing (LPB)

The LPB parameters are reviewed here in order to design the best process for LIE tests. The LPB process develops a deep layer of high magnitude compressive residual stress, with improved surface finish but minimal cold work, which provides the thermal stability of the compressive residual stresses produced [38, 39]. LPB can be performed

with either CNC or conventional machines. The process involves a pass or multipass of a smooth free rolling spherical ball tool on the surface of a workpiece, under a normal force sufficient to plastically deform the surface of the workpiece, as shown schematically in Figure 2-5 [43]. The hard ceramic burnishing ball is supported in a fluid bearing and is lifted off the surface of the retaining spherical socket. The ball is in mechanical contact only with the surface to be burnished; hence, it is free to roll in any direction [44].

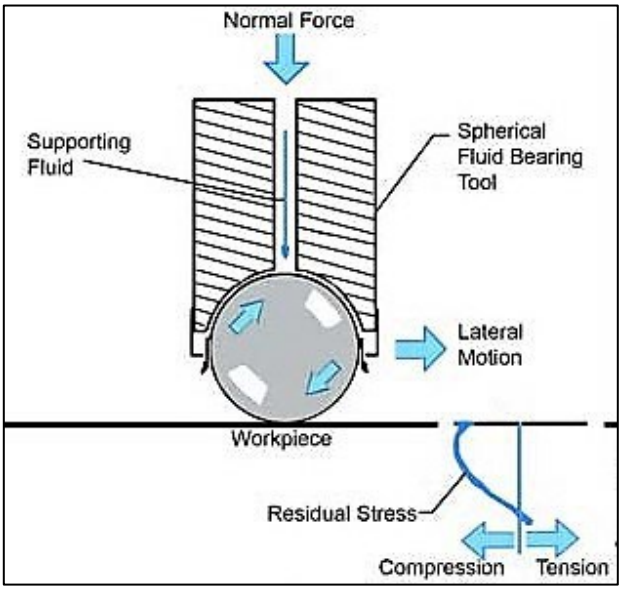

Figure 2-5 Schematic of LPB process [43].

LPB develops subsurface Hertzian contact stresses (residual stresses), which act parallel to the burnished plane. With sufficient normal pressure, the subsurface stress exceeds the yield strength of the workpiece, reaching a maximum beneath the surface, thereby producing deep subsurface compression [45].

2.2.1 Process parameters of LPB

The significant processing parameters of LPB are: feed rate, normal force provided by the hydraulic pump, LPB ball material, LPB ball diameter and number of passes [43–46]. With a poor choice of processing parameters, the workpiece surface could be left

nearly stress-free or even in tension [50, 51]. Hence, process optimization has to be used to select parameters that leave the treated surface in compression.

2.2.2 Characterization of LPB process

LPB produces a good surface finish and induces a relatively a high compressive residual stress at the substrate surface. The change in surface characteristics, due to LPB, can cause improvement in surface hardness, wear resistance, fatigue resistance, yield and tensile strength [38, 48, 49]. Thus, studying the influence of different LPB conditions on different properties is essential.

As a cost-effective surface enhancement technology with processing speed comparable to those of conventional machining operations, LPB is widely used for many applications. Deep compression produced by LPB could improve the fatigue strength of engine parts made of IN718, Ti64, and Al 7075-T6 alloys [46, 50–53]. These advantages of LPB have attracted attention of US Air Force and US Navy, and the process has been investigated for potential use in aircraft industry [58]. Application of LPB to the manufacturing of compressor blade is shown in Figure 2-6 [59].

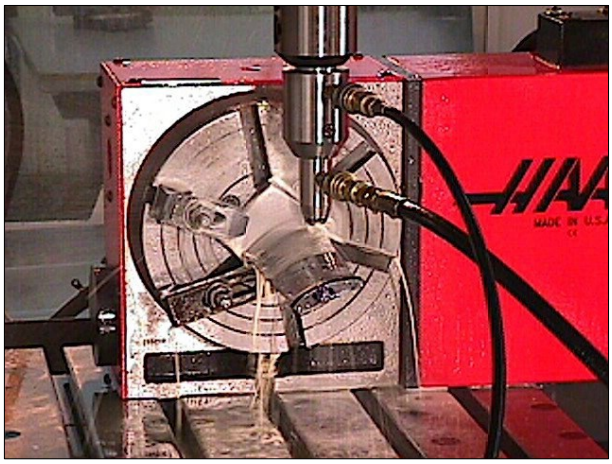

Figure 2-6 LPB application to an engine compressor blade using four-axis CNC milling machine [59].

1) The compressive residual stress induced by LPB

An LPB treated workpiece has a maximum magnitude of compressive residual stress just below the surface with a small equilibrating tensile stress inside the workpiece, as shown in Figure 2-7 [36]. When considering the compressive residual stress, the depth of the compression and its magnitude are very important. The reviews of different LPB processing parameters on the residual stress distribution are as follows:

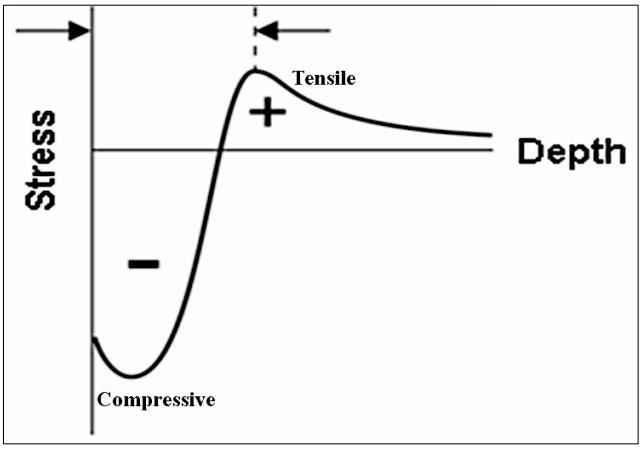

Figure 2-7 Residual stress distribution of a LPB treated workpiece [36].

a) The effect of LPB load on residual stress distribution

Finite element analysis and experimental study (Figure 2-8) have been used to investigate the effect of LPB load on residual stress distribution [50]. The results showed that both the magnitude and the depth of compressive residual stress increase with increasing the LPB load. This effect is synonymous with increasing the laser intensity in the LSP process [42, 50]. However, the depth where the maximum compressive residual stress occurs stays almost the same [59].

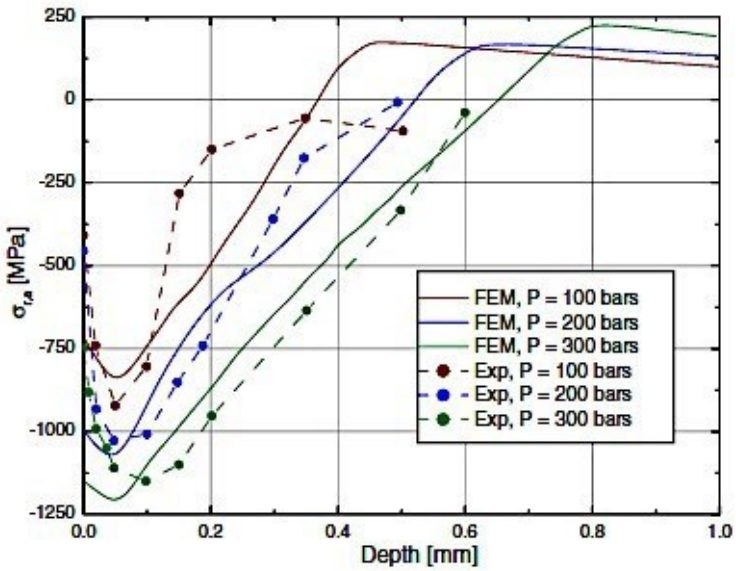

Figure 2-8 FEM and experimental results of the effect of different pressure on residual stress distribution [50]

b) The effect of LPB ball material on residual stress distribution

Several studies [33, 38, 57, 58] were conducted to verify the effect of LPB ball material on residual stress distribution. There was no noticeable difference in the residual stress distribution obtained with the use of chromium steel, beta-silicon nitride, and tungsten carbide burnishing balls. Hence, the effect of burnishing ball material on residual stress is negligible.

c) The effect of LPB ball diameter on residual stress distribution

Sartkulvanich *et al.* [60] studied the effects of LPB ball diameter on residual stress. Using a larger burnishing ball led to a slight increase in maximum compressive residual stress and much deeper compression layer, this is due to the fact that a larger ball presses down the near-surface material more repeatedly and uniformly when compared to LPB with a smaller ball as shown in Figure 2-9 [50]. Although using different sizes of LPB balls

did not affect the depth where the maximum compressive residual stress resides.

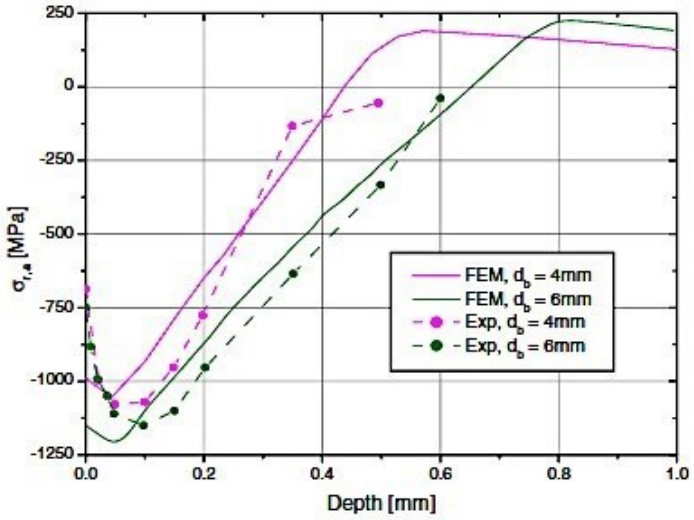

Figure 2-9 FEM and experimental results of the effect of ball diameter on residual stress distribution [50].

d) The effect of overlapping ratio on residual stress distribution

Multipass LPB has been used to study the effect of different overlapping ratios on residual stress distribution [59, 60]. According to the finite element modeling results of Zhuang and Wicks [64], as shown in Figure 2-10 [64], the magnitude and the depth of the compressive residual stress induced by the 2-pass LPB are greater than those of a single pass LPB. However, the experimental work of Salahshoor and Guo [42] showed that overlapping ratio has no significant influence on the residual stress distribution, as shown in Figure 2-11 [42].

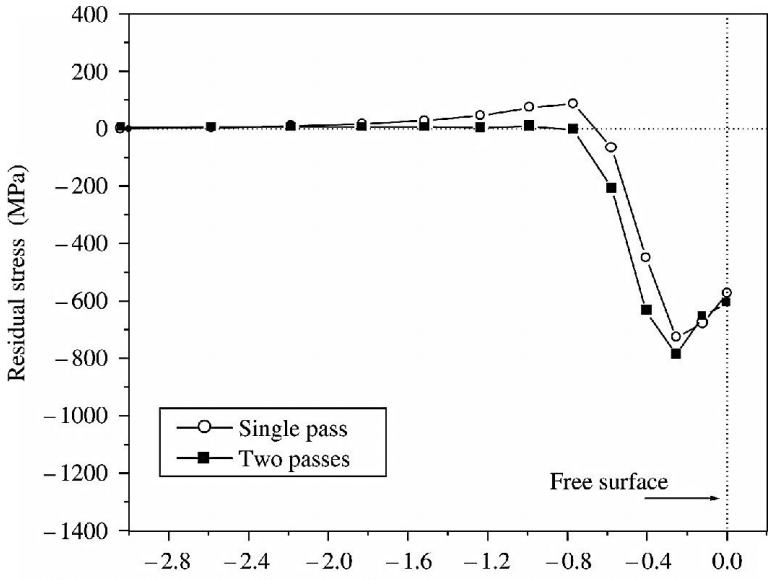

Figure 2-10 FEM result of multipass LPB on residual stress distribution [64]

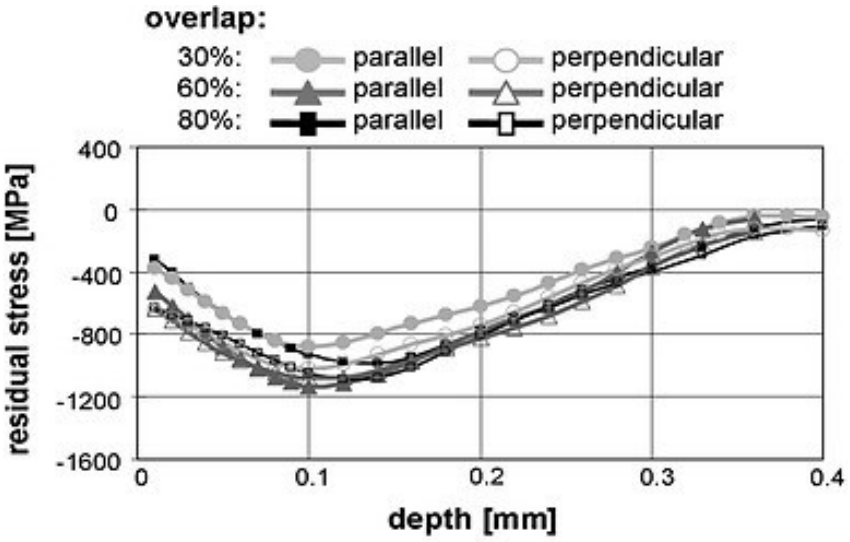

Figure 2-11 Experimental result of the effect of different overlapping ratios on residual stress distribution [42].

2) The effect of LPB on microhardness

The near-surface microhardness depth profiles of an LPB treated Ti64 samples showed a 10% increase in hardness compared to virgin Ti64, as shown in Figure 2-12 [65]. This could be due to the existence of a work-hardened layer after surface treatment [65]. However, the trend line was not convincing since it was not well matched with the scattered readings of the microhardness. The claimed 10% increase of the microhardness

induced by LPB at the near-surface region could be within the difference of microhardness between α and β phases.

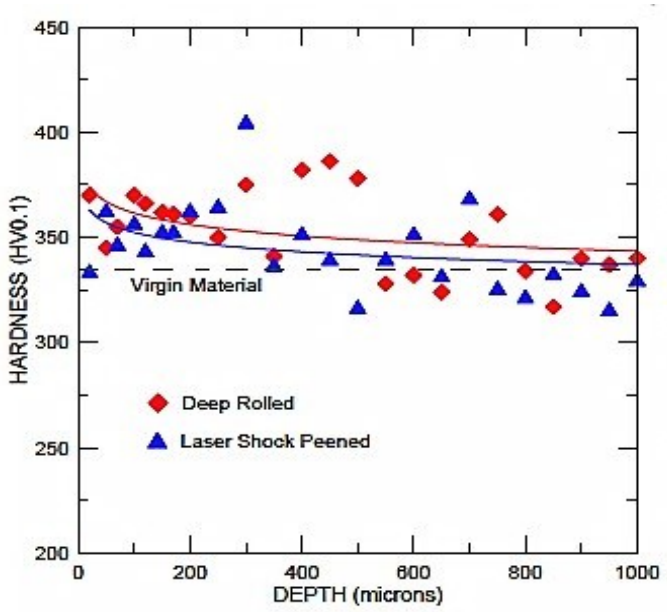

Figure 2-12 In-depth microhardness profile of LPB (Deep Rolling) and LSP treated Ti64 alloy [65].

Luo *et al*. [48] performed a parametric study of the effect of LPB parameters on the surface microhardness. The parameters that had an influence on hardness, in decreasing order of importance, were burnishing feed, pressure, ball diameter and number of passes [66]. Figure 2-13 [67] shows the relationship between the burnishing feed *f*, and the surface microhardness of two different materials. The results showed that the surface microhardness of both materials increased with an increase in the feed rate of the LPB process.

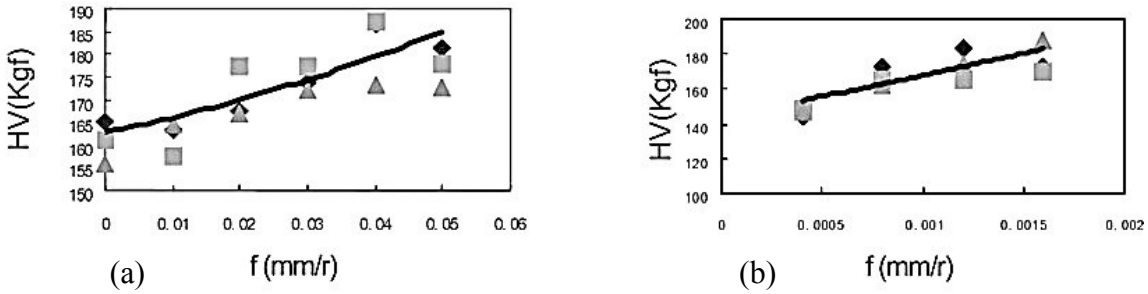

Figure 2-13 Correlation of the burnishing feed with surface microhardness: (a) Specimen material: H62LY12, n=4000r/min, burnishing depth d=3.5μm; (b) Specimen material: LY12, n=3000r/min, burnishing depth d=2μm [67].

While in terms of the correlation of the burnishing pressure and surface microhardness, results in Table 2-1 [68] show that for both heat-treated steel and Inconel 718, the surface microhardness improved by increasing the burnishing pressure.

Table 2-1 Vickers hardness of heated-treated steel and Inconel 718 near to the LPB treated surface [68]

Burnishing pressure (normal force)	Surface hardness of heat-treated steel	Burnishing pressure (normal force)	Surface hardness of Inconel 718
0 MPa	32 HRC	0 MPa	41 HRC
10 MPa (250N)	36 HRC	10 MPa (250N)	43.8 HRC
15 MPa (375N)	37 HRC	15 MPa (375N)	44.6 HRC
20 MPa (500N)	38 HRC	20 MPa (500N)	46.5 HRC

3) The effect of LPB on surface roughness

LPB has also been proven to improve surface roughness [57, 63]. The SEM images in Figure 2-14 [69] show the initial turned surface of Ti64 and the surface after LPB treatment. The LPB treated surface became much smoother and uniform, compared to the untreated surface. The direction of LPB operation is depicted by the arrow marks on the images. Mark 'G' in Figure 2-14 shows that sharp machining marks deformed due to the LPB process. According to Low and Wong [69], when the surfaces are under continuous compressive load during LPB operation, the sharp asperities deform, resulting in a smoother and more uniform surface. SEM image of the LPB treated Ti64 also shows some of the undeformed asperities ('F' in Figure 2-14).

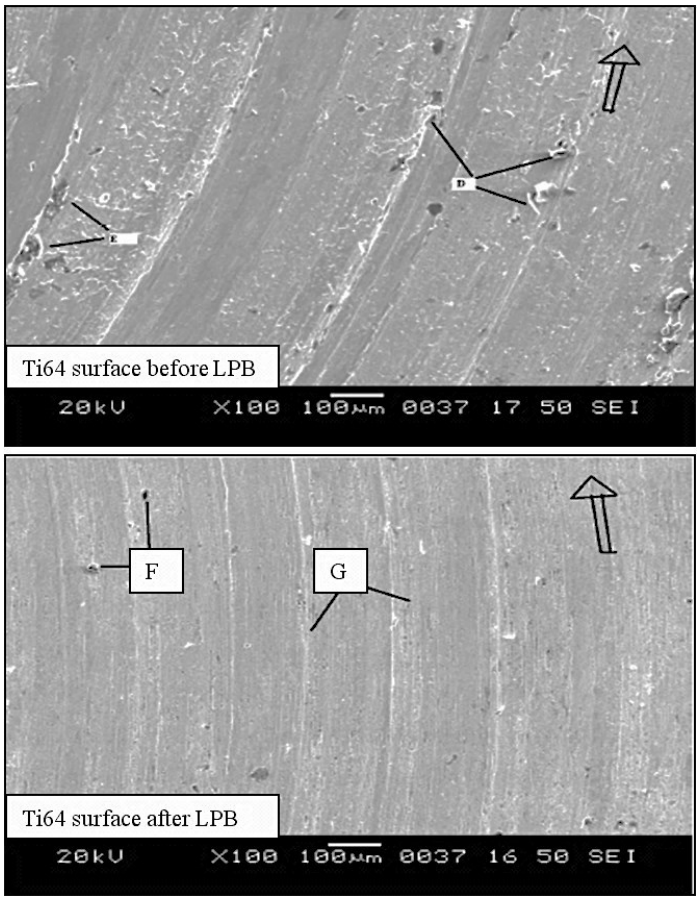

Figure 2-14 SEM image of Ti-6Al-4V surface before and after ball burnishing [69].

Studies [51, 67] show that, no single LPB process parameter has the dominant effect on the surface roughness. All the parameters are interacting. In the case of LPB treated AISI 1045 [71], a strong interaction between burnishing speed and ball diameter was noticed. In order to minimize the surface roughness value, it was recommended to set the burnishing speed, pressure, number of passes at high level and ball diameter at low level. For the LPB process of Ti64 [67], burnishing pressure and number of burnishing passes showed strong interaction. Higher number of passes was recommended to improve the surface roughness of Ti64. Hence, it is important to study the effects of the operating parameters of LPB on surface roughness in order to better characterize the LPB process.

4) The effect of LPB on microstructure

There is relatively less information about the near-surface work-hardened microstructure induced by LPB and its influence on fatigue behavior. Figure 2-15 [73] shows TEM images of Ti64 near-surface nanocrystalline grain structure after LPB surface treatment at different temperatures. Nalla *et al.* [65] studied the correlation between the thermal stability of this nanoscale microstructure and fatigue resistance of Ti64. The near-surface nanocrystalline structure stayed perfectly stable up to 500-550^{o}C as shown in Figure 2-15, where complete release of the applied compressive residual stresses has occurred, as shown in Figure 2-16 [65]. In conclusion, the improvement of fatigue resistance after LPB treatment at elevated temperatures could be attributed to the existence of the thermally stable, near-surface, nanocrystalline grain structure [65, 73, 74].

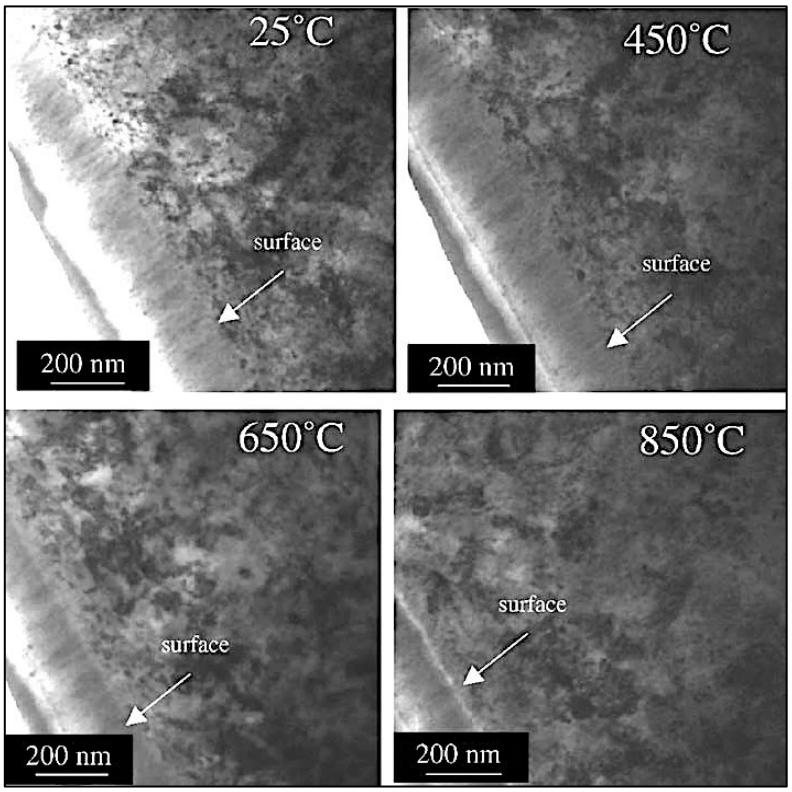

Figure 2-15 Near-surface microstructure of LPB treated Ti–6Al–4V after thermal exposure at temperatures between ambient and 850^{o}C [65].

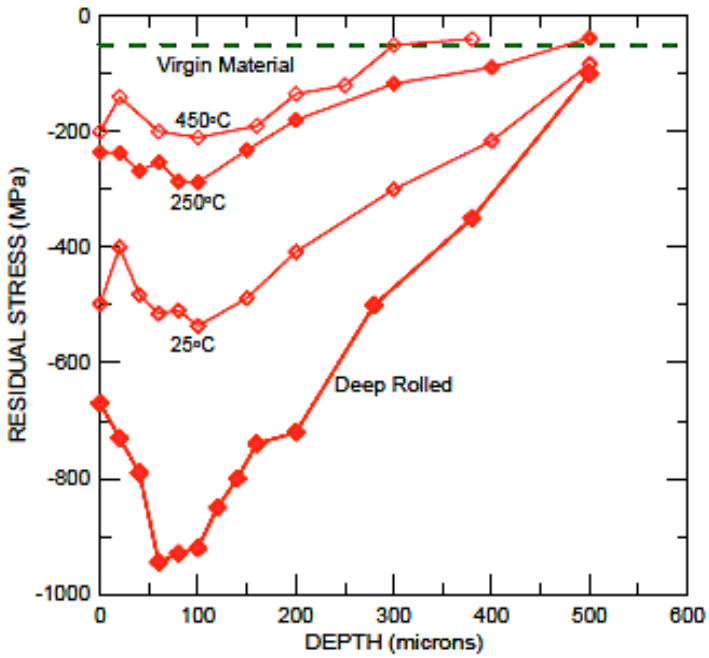

Figure 2-16 Release of residual stresses of LPB treated (Deep Rolled) Ti64 at elevated temperatures [65].

2.3 Evaluation and comparison of LPB with LSP and SP

All these surface enhancement techniques are aimed at developing a layer of compressive residual stress using mechanical deformation. However, the techniques differ in terms of how the surface is deformed, the form and magnitude of the residual stress and plastic deformation distributions developed in the surface layers [55]. General evaluations and comparisons were made among these three surface enhancement techniques, as shown in Table 2-2.

Table 2-2 Evaluation and Comparison of LPB with LSP and SP

Surface Enhancement Techniques	Cold work Percentage	Depth of Compressive Residual Stress	Surface finish	Processing time	Cost
LPB	Low	Deep >1mm	Mirror like	Moderate	Moderate
SP	High	Shallow 0.2-0.5mm	Poor	Fast	Low
LSP	Low	Deep >1mm	Worsen	Slow	High

2.3.1 Residual stress profiles

Figures 2-17 [68] and 2-18 [75] show comparisons of residual stress profiles among various surface treatments. In general, SP generates relatively shallow depths of high magnitude compressive residual stresses. With LSP, the depth of induced compressive residual stresses is significantly greater than that produced by SP. On the other hand, LPB generates high magnitude of compressive residual stresses through a deeper thickness of the substrate.

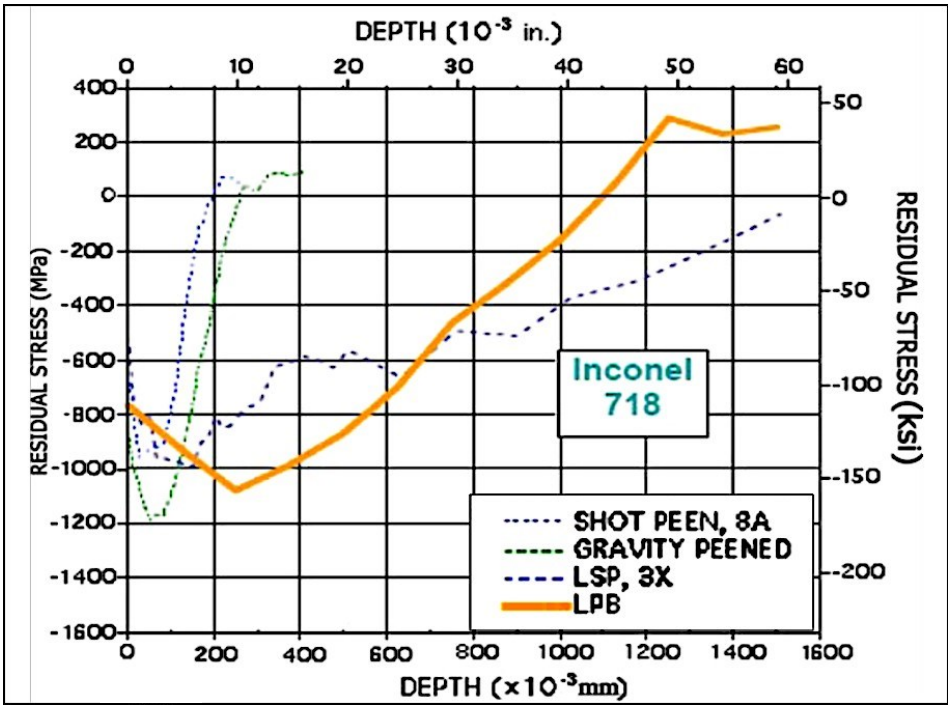

Figure 2-17 Comparison of residual stress profiles induced by SP, LSP and LPB for IN718 [68].

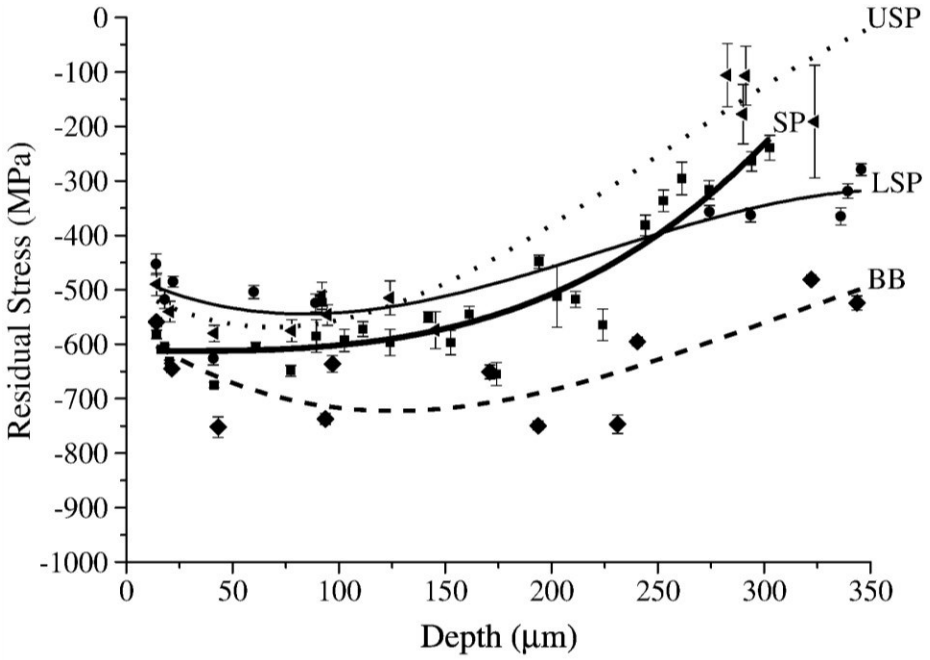

Figure 2-18 Residual stress–depth distribution in Ti–2.5Cu (SHT) after various surface treatments (SP=shot peening, BB=ball-burnishing, LSP=laser shock peening, USP=ultrasonic shot peening, SHT=solid solution heat treatment) [75].

2.3.2 Cold work percentage

Comparison in terms of the degree of cold work among three surface treatment techniques was made as shown in Figure 2-19 [68]. A high amount of cold work (up to 30-40%) is achieved by repeated application of SP. For the LSP process, the degree of cold work (9%) is beneficially less for the same peak compressive residual stress produced by SP. LPB generates the least amount of cold work (4%) for the same peak compressive residual stress at the surface [36, 68]. The minimized plasticity could be attributed to the configuration of the LPB tool constituted by a free rotating ball, which reduces the friction with the workpiece surface [38, 64].

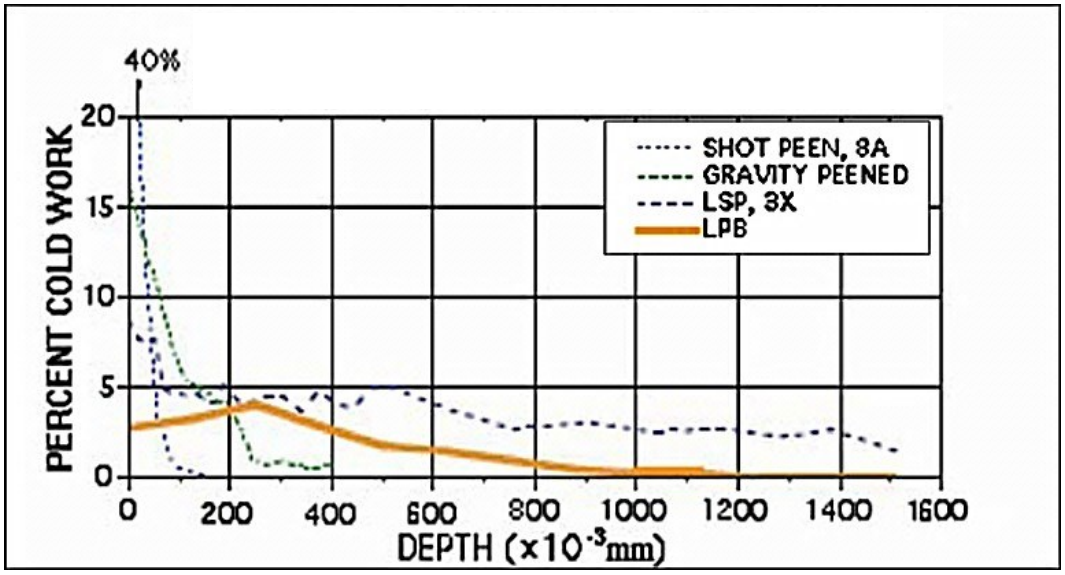

Figure 2-19 Degree of cold work of SP. For LSP process [68].

2.3.3 Residual stress relaxation

Although the mechanism of residual stress relaxation still needs to be investigated, it has been found that the degree of cold work induced during residual stress generation will influence the rate of thermal relaxation of the residual stresses [65]. A comparison study of thermal relaxation for a variety of surface treatment technologies has been conducted, the results indicated that compressive residual stresses at heavily cold worked SP surfaces relaxed very rapidly, compared with that of a low cold worked surface produced by LSP and LPB [65, 68, 74, 76].

2.3.4 Surface finish

SP produces a poor surface finish by bombarding the workpiece with hard shots, resulting in localized plastic deformation (Figure 2-20 b). However, LPB improves the surface close to a mirror-like finish after the process (Figure 2-20 a). While in the case of LSP, the surface finish could be worsened after the treatment (Figure 2-20 c) [75].

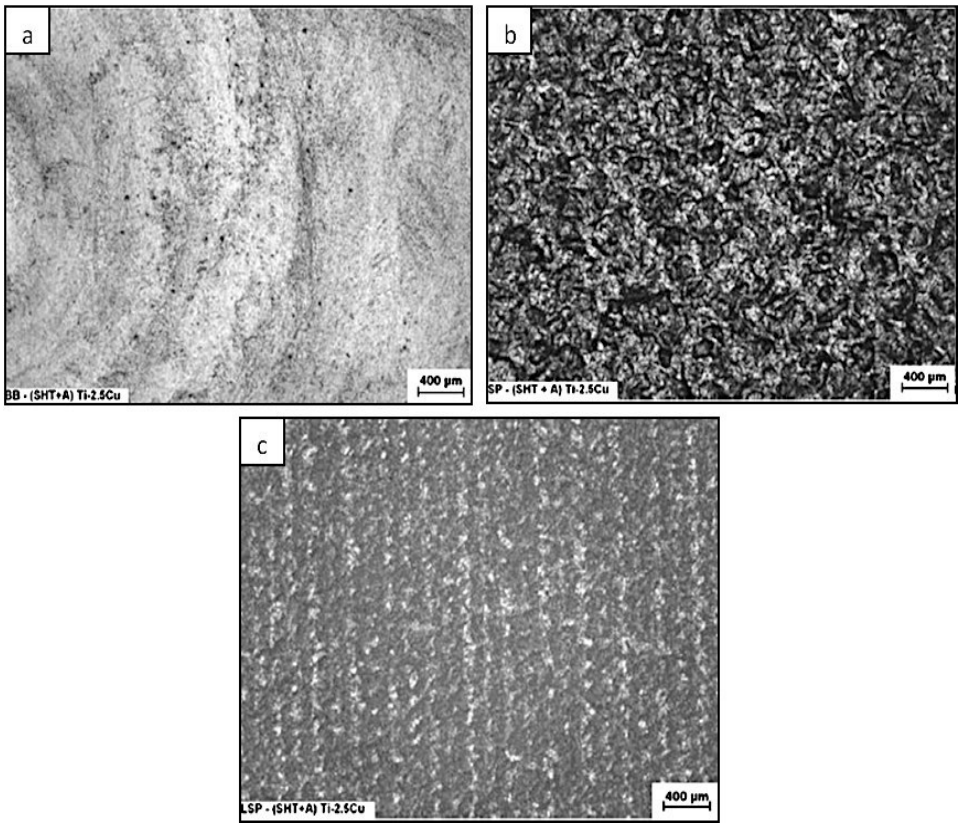

Figure 2-20 Images of the mechanically treated surface (a) LPB, (b) SP and (c) LSP [75].

2.3.5 Cost and processing time

LSP is the most expensive and the slowest, compared to SP and LPB, and it is the most difficult to incorporate into an existing machine shop environment, while LPB can be carried out on existing CNC or conventional machines, at speeds comparable to conventional machining processes such as surface milling [38, 58, 75].

2.4 General properties of Ti6Al4V

Titanium alloys are used as base material for the compressor of the gas turbine blades. They are also used as erosion shield material for the last stage rotor blades in large steam turbines, because of their high strength to weight ratio and better erosion/corrosion resistance [18]. Ti64 is the most widely used titanium alloy. Ti64 contains 6% aluminum (Al) and 4% vanadium (V), making it an alpha-beta alloy. Table 2-3 shows a typical

chemical composition of Ti64. It has a density of roughly 4.4 g/cm^3, compressive yield strength of 970 MPa, and tensile yield strength of 880 MPa. Although Ti64 has good mechanical properties, LIE remains a problem.

Table 2-3 Chemical composition of Ti64 (wt. %) [77]

	Al	V	C	N	O	H	Fe	Y	Others	Ti
Min.	5.5	3.5	-	-	-	-	-	-	-	-
Max.	6.75	4.5	0.08	0.5	0.2	0.0125	0.3	0.005	0.1	Balance

2.5 Objectives of the present work

Previous studies have introduced LSP and SP as potential solutions for LIE of Ti64. However, no study has been performed to study the effects of LPB on the water erosion resistance of Ti64. Therefore, the present work aims at filling this research gap.

The objective is to undertake a series of tests to measure the water erosion performance of Ti64 that has been treated by a LPB process. In order to find suitable process parameters for this LPB process, an investigation of the principal LPB parameters (the feed rate, spindle velocity, number of passes and pressure) on Ti64 were undertaken.

The optimized process will then be used for the liquid impingement coupon. Residual stress distribution, microhardness and surface roughness measurements were conducted to characterize the LPB process.

Since LIE resistance depends on a combination of different properties of the material, the present work is expected to establish the correlation between the LIE performance and the properties of Ti64 improved by LPB.

The present study aims at:

- Optimizing the LPB process parameters in order to obtain much deeper and larger compressive residual stress.

- Investigating the effect of hardness on the LIE performance of Ti64.
- Investigating the effect of compressive residual stress on the LIE performance of Ti64.
- Studying the LIE mechanisms of LPB-treated and non-treated Ti64.

Chapter 3

Experimental Methodology

This chapter introduces the material processing, as well as the parameters used for the LPB treatment. Furthermore, the methods used for evaluating surface roughness, microhardness, residual stress, microstructure and water droplet impingement test are described. Figure 3-1 shows a brief description of the research methodology used during this work. The Ti64 alloy was received from Performance Titanium Group (San Diego, US) in the form of a square plate. The as-received Ti64 plates were then cut and LPB treated. The burnished alloys were then subjected to several characterization processes such as: microhardness, microstructural, surface roughness, residual stress and LIE measurements.

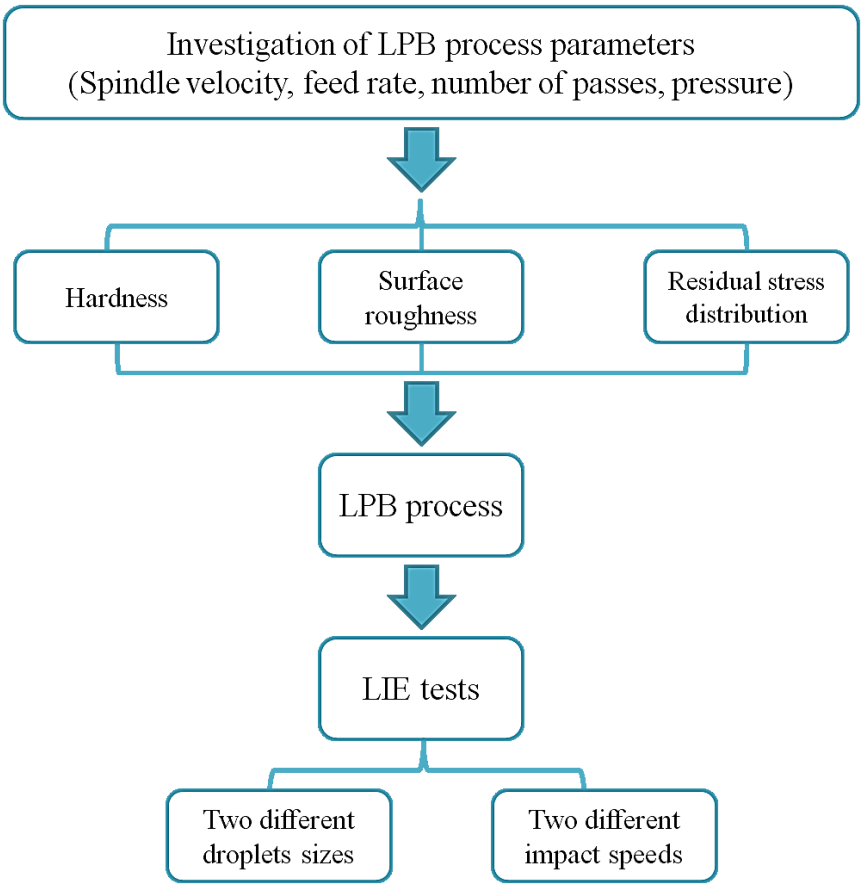

Figure 3-1 Research methodology used in the present work.

The detailed description of the experimental methodology is as follows:

3.1 Ti6Al4V sample preparation

The Ti64 (AMS 4911) was received as an annealed plate with dimensions of 12 inch × 12 inch × 0.6250 inch. It was cut into 16 small squares, with sides of 3 inches. The small squares were machined into small disks with 3 inch diameter. These disks were processed using different LPB parameters on a conventional lathe at Concordia University. Two T-shape LPB samples, as shown in Figure 3-2, were cut from each disk using a waterjet cutting machine. This particular design was made for the LIE-tested parts of both T-shape coupons to have the same strain rate after LPB treatment. The T-shape samples and cutting steps are shown in Figure 3-3.

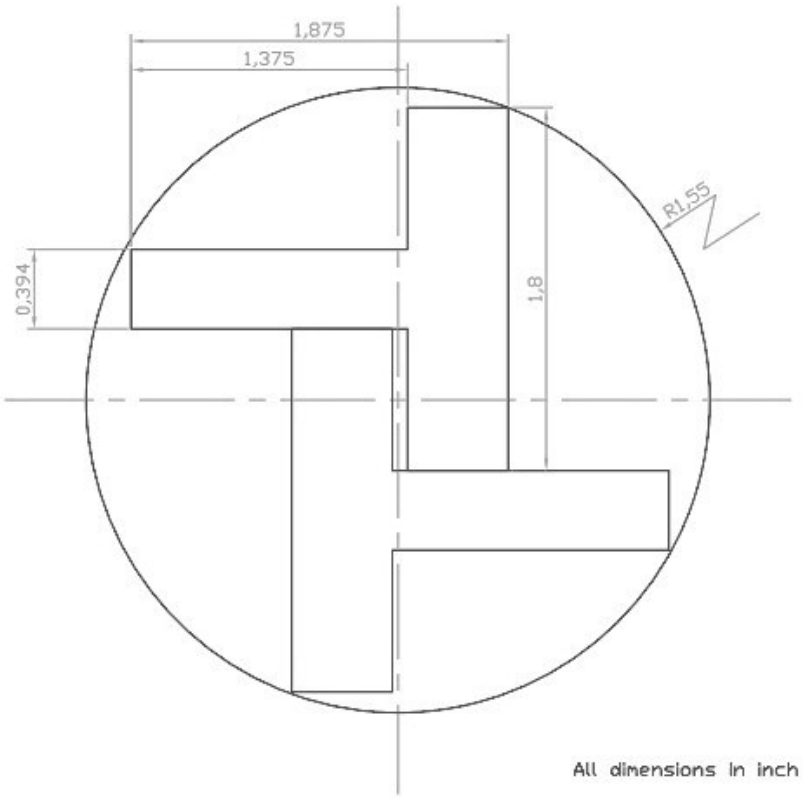

Figure 3-2 Schematic of the two T-shape samples cut from small disks.

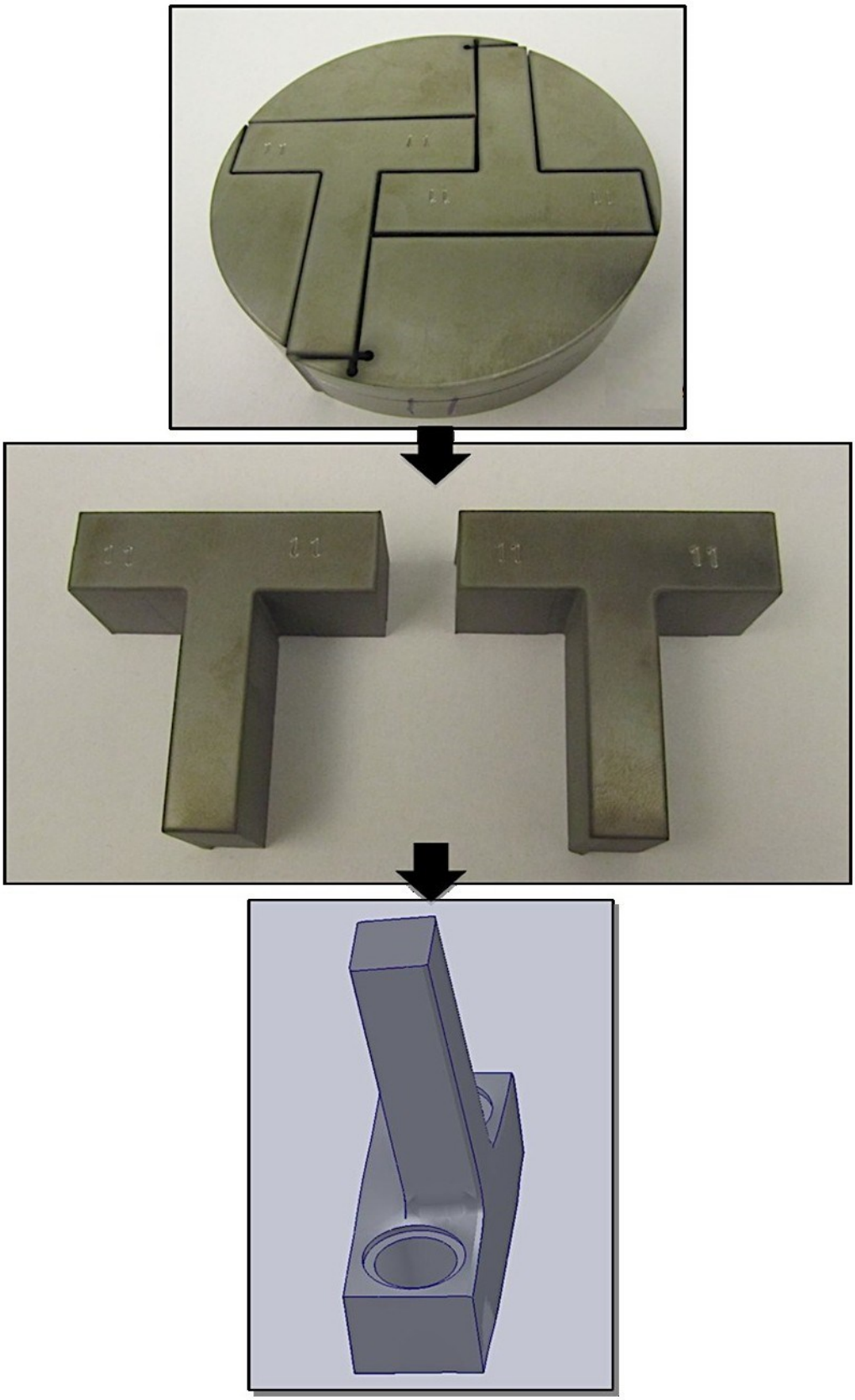

Figure 3-3 Cutting steps for the T-shape samples.

3.2 Low plasticity burnishing

The LPB equipment is from ECOROLL Company (Ohio, US). The equipment, shown in Figure 3-4, consists of a 6.6 mm hard ceramic ball able to process material up to 65 HRC hardness equipped with a hydraulic pump that is able to provide pressures up to 200 bars. Graphical representation of the LPB process is shown in Figure 3-5. It is carried out by mounting the burnishing tool on a manual lathe and then pressing the tool against the rotating Ti64 disk surface with the normal force provided by the hydraulic pump.

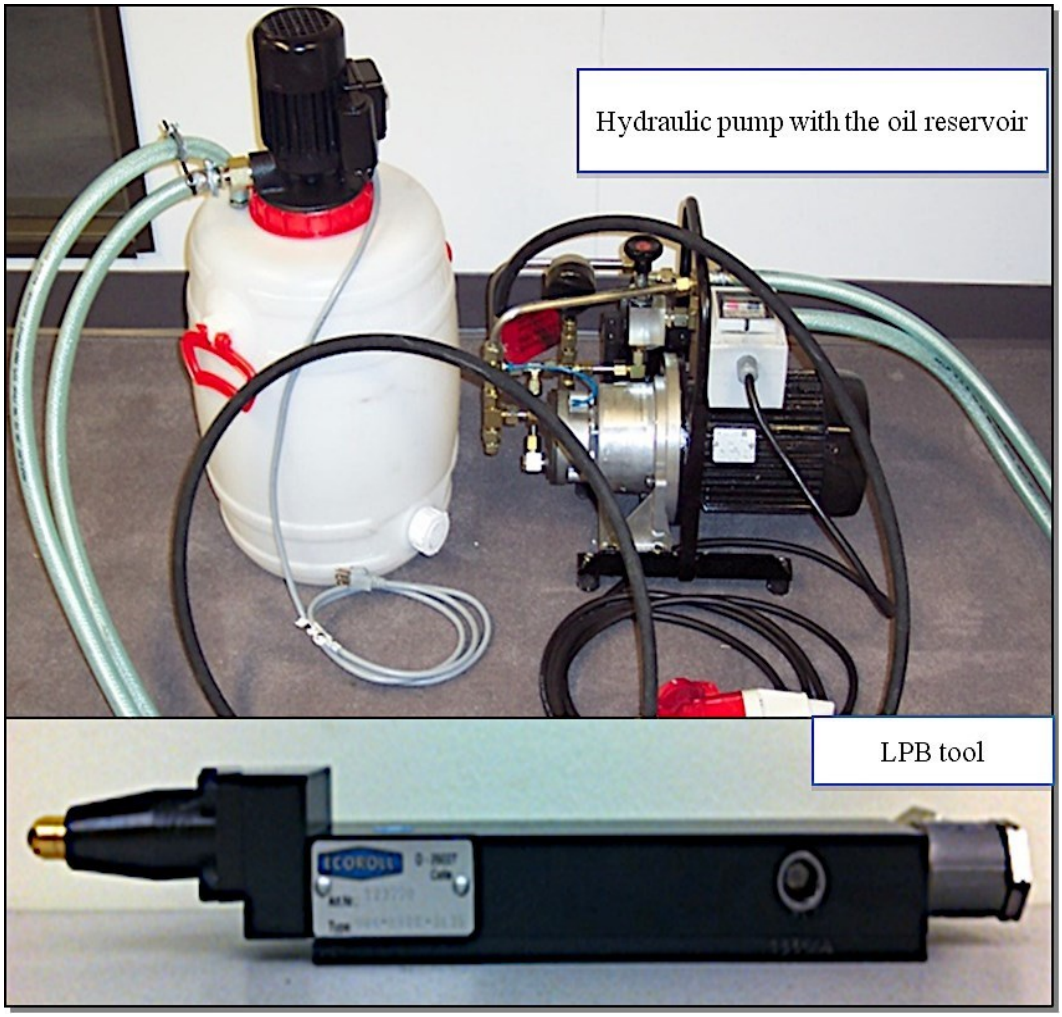

Figure 3-4 LPB tool and hydraulic pump.

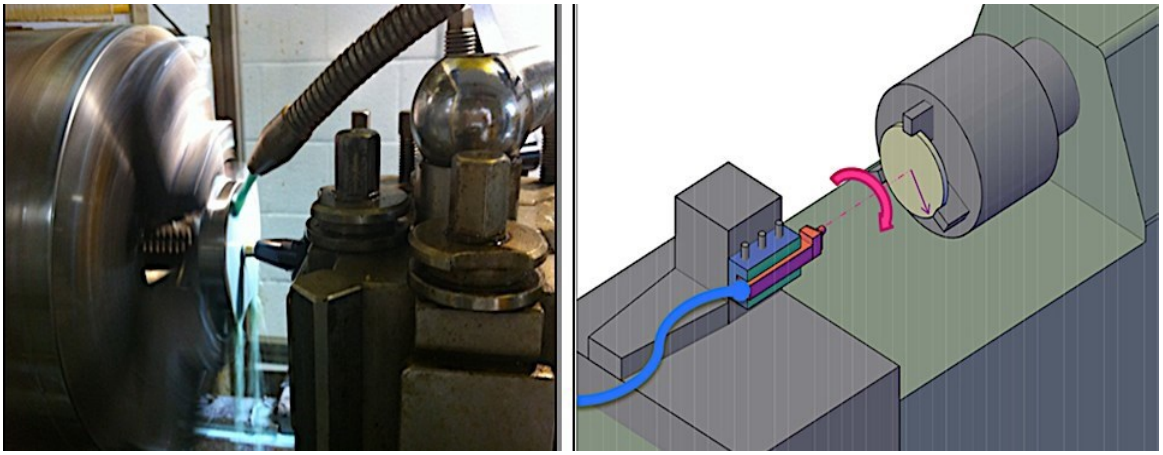

Figure 3-5 LPB process on a conventional lathe.

3.3 Surface roughness

The surface roughness of the various burnished samples was determined by means of an electronic contact profilometer instrument (Mitutoyo Surftest SJ-210). The arithmetic mean roughness (**R**a) was used to represent the surface roughness. The average of five roughness measurements was taken for each LPB sample.

3.4 Microhardness

3.4.1 Surface microhardness

The surface microhardness was determined using a square-base pyramid-shaped indenter (Mitutoyo Surftest SJ-210) for testing in a Vickers tester. A nominal force of 100 gram-force (gf) and a loading time of 15 s were used for the tests. The average of five measurements was taken at the surface of each sample to evaluate the surface microhardness improvement after LPB treatment.

3.4.2 In-depth hardness profile

Nano indentation measurements were performed to construct the hardness-depth profiles, as shown in Figure 3-6. The measurements were repeated twice for each sample and the average of two measurements was taken at each depth. The cross-sectioned LPB

samples were polished down to 1-micron. The measurements were taken across the depth at an interval of 0.025 mm starting from the edge of the burnished surface and going toward the center. The total depth of measurements was around 0.8 mm.

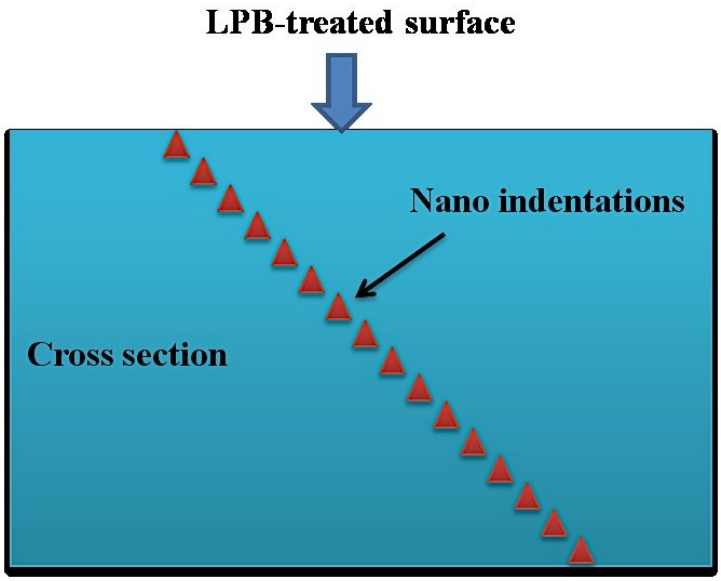

Figure 3-6 Schematic for in-depth hardness measurement.

3.5 Microstructural analysis

Hitachi S-3400N Scanning Electron Microscope (SEM) was used to observe the microstructure of the Ti64 sample before and after the LPB surface treatment. The surface preparation of the samples was done the same way as that of the cross-sectioned samples used in in-depth hardness measurements. SEM was also used to study the LIE mechanism of the tested samples.

3.6 Residual stress: incremental hole drilling method (IHD)

The Incremental Hole Drilling Method (IHD) was used in the present work to study the compressive residual stress distribution induced by various LPB conditions. The hole drilling method is a well-established and widely accepted technique for measuring residual stress. A strain gauge rosette is first bonded to the surface of the component under

investigation. A hole is then drilled using carbide tipped drill with 1.5 mm diameter driven by an air-turbine with a rotational speed of 200,000 rpm into the component through the center of the gauge to a depth approximately equal to half its diameter, as shown schematically in Figure 3-7. The original stress state in the component is then calculated from the relieved strain values according to ASTM E 837–01. Both the magnitude and directions of principal stresses are calculated [78, 79]. During the IHD measurement, the carbide tipped cutter is milling and drilling the workpiece at the same time as can be seen in Figure 3-7. As a result of that, a flat-bottom hole was made, as shown in Figure 3-8; this was aimed at avoiding stress concentrations for each increment of stress measurement.

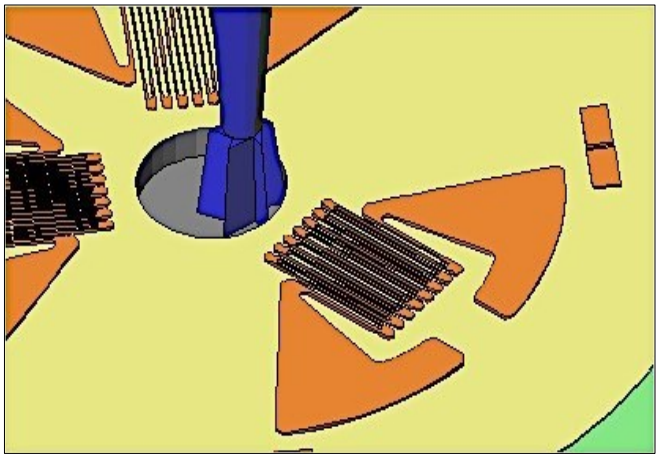

Figure 3-7 Process of carbide tipped cutter milling the hole [80].

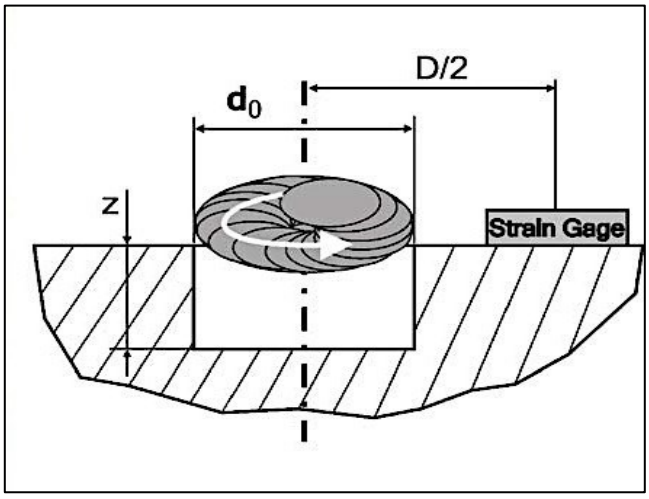

Figure 3-8 A flat-bottom hole was drilled after each increment of IHD measurement [78].

Target site surfaces were prepared for gauge installation by two very light passes of 400 grade abrasive paper followed by thorough degreasing. One rosette (CEA-06-062UL-120), as shown in Figure 3-9 was installed on the surface of each sample with elements 1 and 3 aligned as shown in Figure 3-10. These directions also refer to stresses σ1 and σ3 in the subsequent results sheets. For all the 16 samples, gauges were installed and drilled at the same position in relation to the curved surface as shown in Figure 3-10.

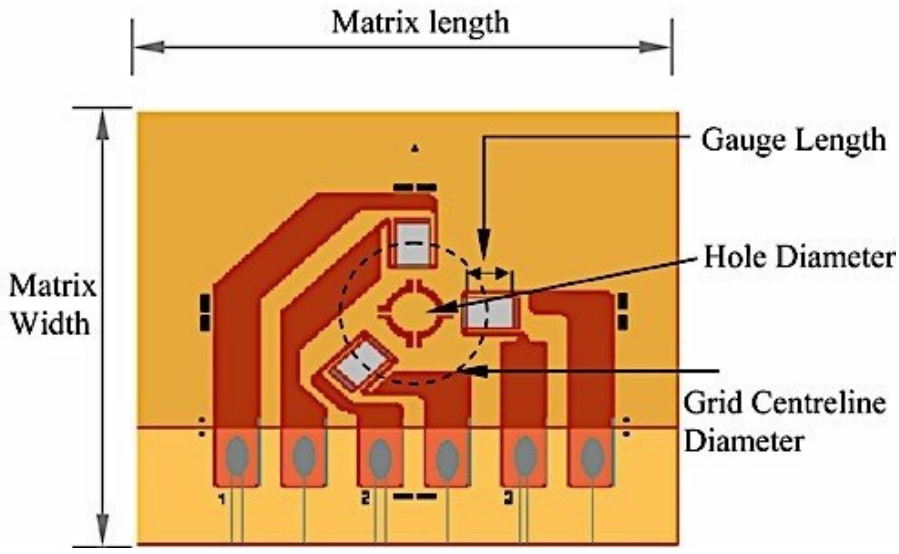

Figure 3-9 The schematic of CEA-06-062UL-120 strain gauge [81].

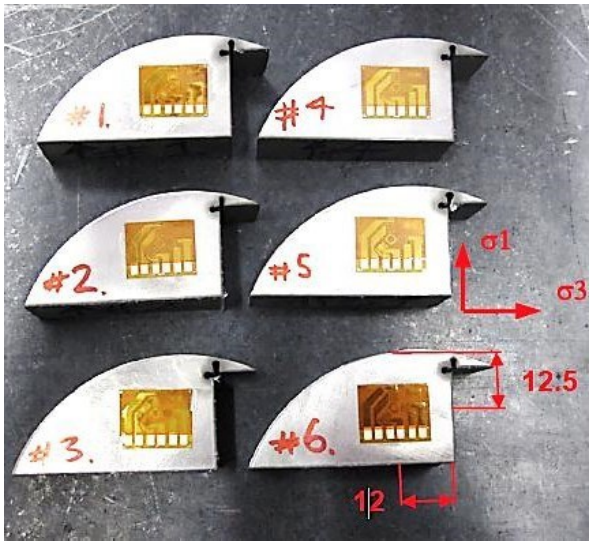

Figure 3-10 The positions of the stain gauge as installed.

Each sample in turn was cemented to an angle plate. Gauges were drilled using a miniature PC-controlled orbital driller; depth increments were set at 4 x 32 μm + 4 x 64 μm + 8 x 64 μm, giving a completed hole depth of 1,408 μm. Figures 3-11 and 3-12 show the arrangement for incremental drilling.

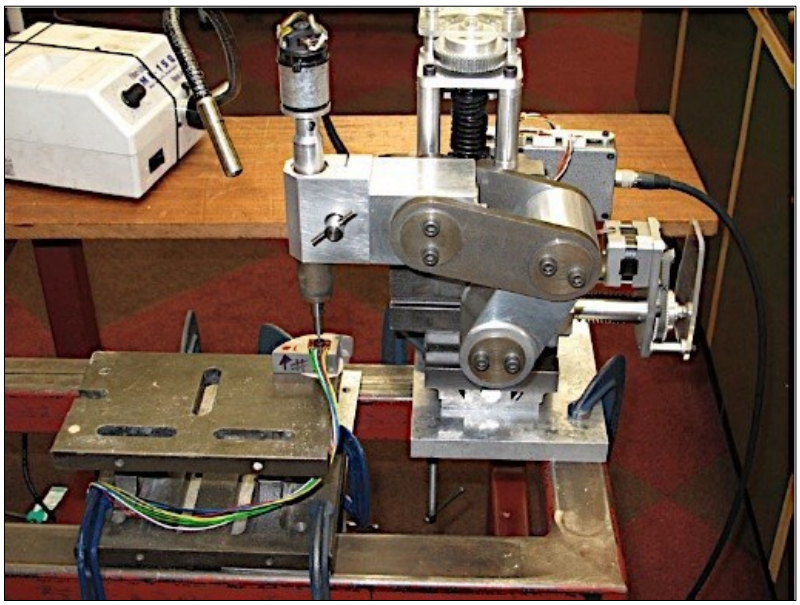

Figure 3-11 The arrangement for incremental drilling.

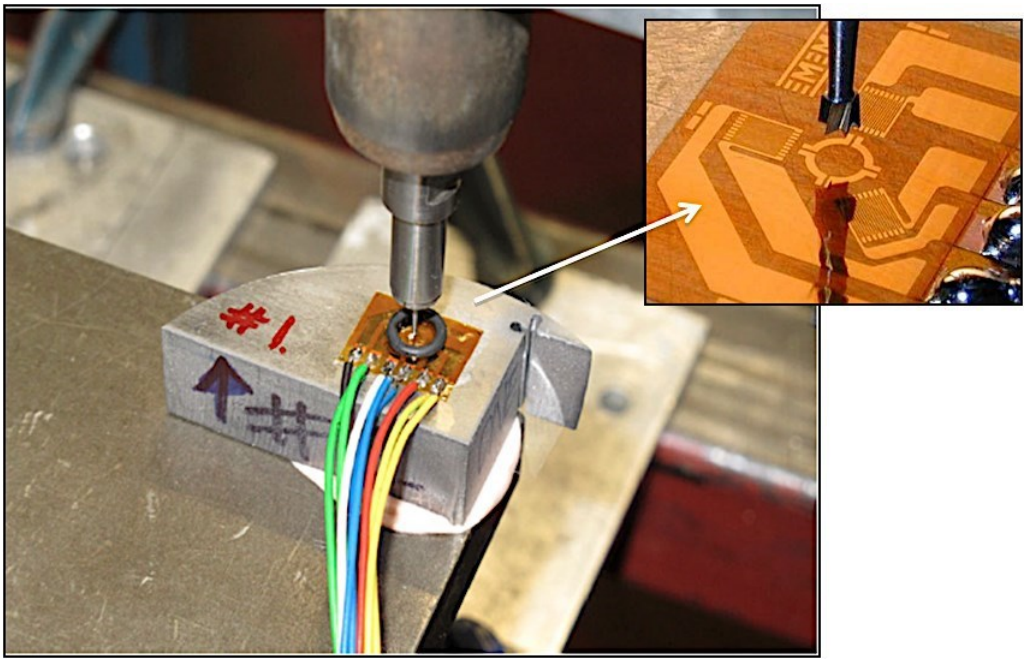

Figure 3-12 The arrangement for sample of incremental drilling.

3.7 Water droplet erosion test

3.7.1 Water droplet erosion rig

The water droplet erosion test was done using the rig as shown schematically in Figure 3-13. It simulates the working condition of the compressor blades and could reach the maximum testing speed of 20,000 rpm with the rotating disk. Three different designs of coupons are used for different testing speeds, as shown in Figure 3-14. The flat coupon as shown in Figure 3-14 (a), coupled with the L-shaped sample holder, was used in the LIE tests with impact speed lower than 350m/s; the T-shape coupon shown in Figure 3-14 (b) could be tested in the LIE tests with impact speed up to 500m/s; the L-shape coupon Figure 3-14 (c) is designed for the LIE tests with the impact speed up to 350m/s. The rig has two camera ports, top and side, to observe water impingement using a high-speed camera.

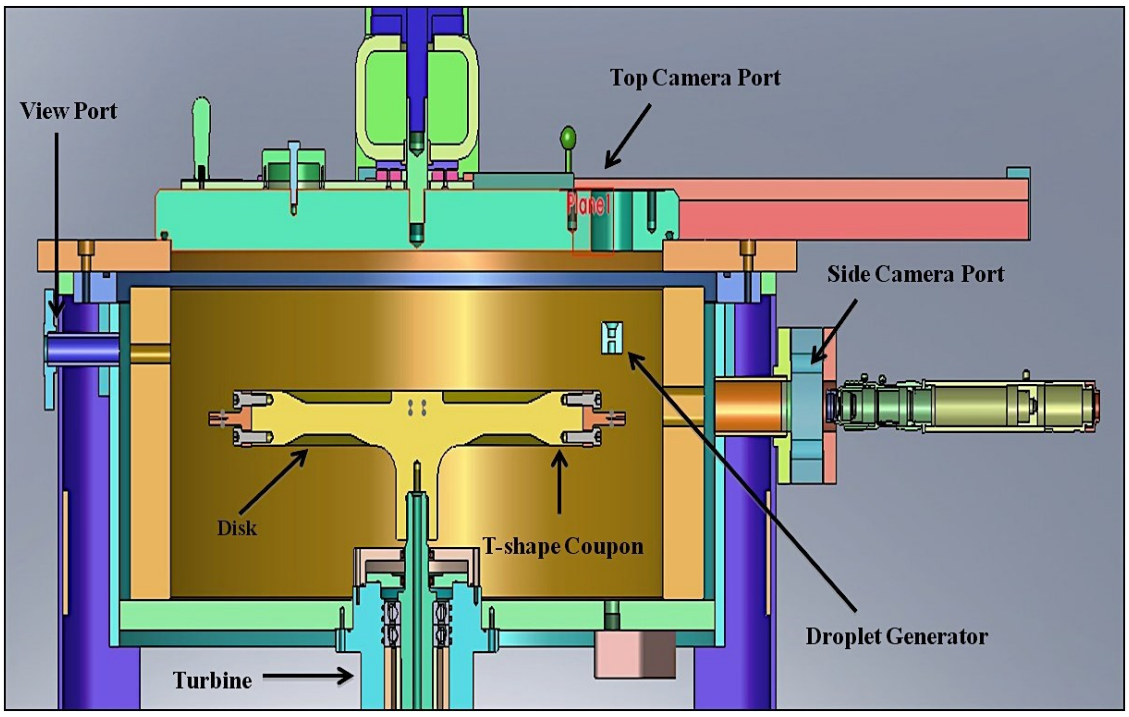

Figure 3-13 Schematic of the Water Erosion Rig.

The experiments were performed using pressurized deionized water, supplied by a vacuum pump and injected through orifice nozzles with diameters of about 400 μm and

600 μm. The experimental parameters of this rig were set up empirically using the DOE method. The initial water pressure was fixed at 30 psi. The stand-off distance between the nozzle and the specimen was set at 50 mm. The flow rates of the 460 μm and 630 μm droplets were set at 0.05L/min and 0.1L/min, respectively. Two water droplet impingement speeds; 250 m/s (10000 rpm) and 350 m/s (14000 rpm) were used for both sizes of droplets.

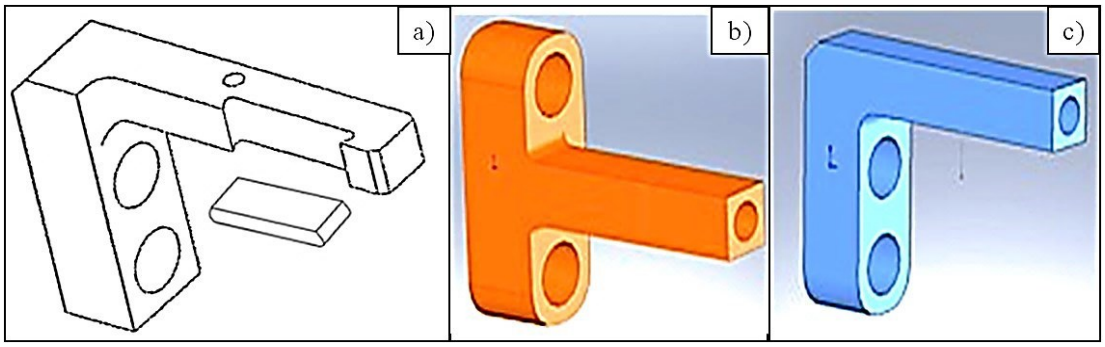

Figure 3-14 Coupons for LIE tests at different impact speeds: a) flat coupon coupled with the sample holder; b) T-shape coupon; c) L-shape coupon.

3.7.2 Water droplet size determination system

Since water droplets have a broad size distribution, normally, the mean diameter is used in the prediction of erosion for convenience. In this study, a high-speed camera was setup and aimed at a transparent glass water box which simulates the same conditions of the water droplet erosion testing rig as shown in Figure 3-15. Full resolution pictures (500 frames per second) were taken to measure the droplet size. 200 readings of the droplets size were recorded and the droplets size distributions were plotted.

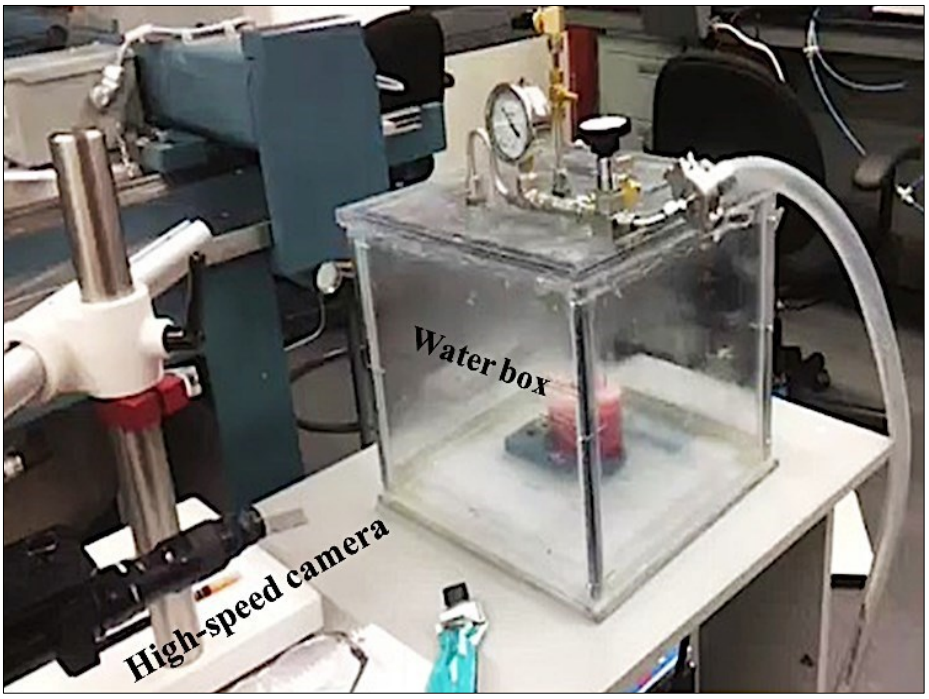

Figure 3-15 High-speed camera setup for water droplet size measurement.

Chapter 4

Results and Discussions

A systematic study of the parametric effects contributing to the surface roughness, surface microhardness and residual stress of LPB treated Ti64 was conducted. Furthermore, the LIE performance of LPB treated Ti64 was evaluated.

A design of experiments (DOE) approach was used for evaluating the parametric effects of LPB treatment. It was carried out using 2-level full factorial (2^k) design considering randomization and replication of experiments since one-factor-at-a-time approach cannot give a clear picture of the effect of parameter interaction. A 2-level full factorial design of experiment is an experiment whose design consists of two or more factors, each with discrete two possible values ("+" and "-") or levels ("high" and "low" level). It consists of every combination of the levels of factors in the experiment [82].

When analysing the full factorial design, several statistical terminologies were used in this study, which are explained as follows.

Main effects refer to the effect of a single factor on a specific experimental response. In contrast, factor interactions occur when the effect of a factor depends on the level setting of another factor.

A Pareto chart could be used to examine the significance of these estimated effects. The output of Pareto chart could be affected by the chosen confidence interval (α), which is used to indicate the reliability of an estimate of the effects [82, 83]. In the present work, a 5% of confidence interval (α) was used, which implies that 95% (1 - α) of the confidence intervals would contain the true response.

4.1 Low plasticity burnishing (LPB)

The parameters involved in the DOE for the present study are: spindle velocity (Factor A), burnishing feed (Factor B), number of passes (Factor C), burnishing pressure (Factor D) and the other parameters were held constant, such as burnishing ball material and diameter.

Each of the four selected parameters was utilized at two different levels with their respective coded values as indicated in: a low level (-1) and a high level (+1). The values of each level, as listed in Table 4-1, were determined from the available literature [39, 67] and recommendations gained from the manufacturer of the LPB equipment (ECOROLL).

Table 4-1 Process Parameters of LPB.

Level / Parameters	High (+1)	Low (-1)
Spindle Velocity (rpm)	150	75
Feed (mm/r)	0.20	0.06
Number of Passes	3	1
Hydraulic Pressure (bar)	200	100

The design table of LPB processing conditions was constructed with the parameters and corresponding coded values in Table 4-1. Sixteen Ti64 disks were treated using 16 different LPB conditions as shown in Table 4-2. Each LPB-treated disk was engraved with the corresponding number in the last column (Order of Runs) of the table, and this is recognized as the LPB sample number in the following text.

Table 4-2 Combinations of parameters for LPB process.

Observation Number	A	B	C	D	Order of Runs
	Spindle V (rpm)	Feed (mm/rev)	#Pass	Pressure (Bar)	
1	-1	-1	-1	-1	(1)
2	+1	-1	-1	-1	(2)
3	-1	+1	-1	-1	(15)
4	+1	+1	-1	-1	(16)
5	-1	-1	+1	-1	(4)
6	+1	-1	+1	-1	(3)
7	-1	+1	+1	-1	(14)
8	+1	+1	+1	-1	(13)
9	-1	-1	-1	+1	(5)
10	+1	-1	-1	+1	(6)
11	-1	+1	-1	+1	(10)
12	+1	+1	-1	+1	(11)
13	-1	-1	+1	+1	(8)
14	+1	-1	+1	+1	(7)
15	-1	+1	+1	+1	(9)
16	+1	+1	+1	+1	(12)

4.2 DOE analysis of surface roughness

Tables 4-3 and 4-4 present the average surface roughness (**R**a) values (average out of five readings) of the 16 different LPB-treated, and the untreated Ti64 substrate. Overall, the range in treatment parameters resulted in an **R**a from 0.05 to over 0.212 μm for LPB-treated samples, while the initial Ra of the Ti64 is 0.35 μm.

Table 4-3 Surface Roughness of LPB treated Ti64.

LPB Sample #	Surface Roughness (μm)					
	R1	R2	R3	R4	R5	Ave.
1	0.12	0.09	0.07	0.09	0.09	0.09
2	0.14	0.13	0.10	0.14	0.15	0.13
3	0.08	0.09	0.12	0.09	0.08	0.09
4	0.07	0.08	0.06	0.09	0.08	0.08
5	0.06	0.06	0.05	0.06	0.08	0.06
6	0.07	0.07	0.10	0.07	0.09	0.08
7	0.07	0.06	0.07	0.07	0.07	0.07
8	0.04	0.07	0.05	0.05	0.04	0.05
9	0.17	0.14	0.13	0.13	0.18	0.15
10	0.13	0.16	0.13	0.15	0.14	0.14
11	0.17	0.16	0.12	0.14	0.11	0.14
12	0.12	0.17	0.19	0.15	0.08	0.14
13	0.15	0.16	0.16	0.14	0.11	0.14
14	0.15	0.13	0.21	0.15	0.14	0.16
15	0.19	0.19	0.34	0.14	0.20	0.21
16	0.15	0.16	0.16	0.14	0.11	0.14

Table 4-4 Initial surface Roughness of Ti64.

Ti64	Surface Roughness (μm)					
	R1	R2	R3	R4	R5	Ave.
	0.22	0.30	0.41	0.50	0.31	0.35

Figure 4-1 shows the general effect of the 16 different LPB conditions on surface roughness of the treated disks as compared to the initial surface roughness of the Ti64

substrate. It is evident that all the LPB conditions left the Ti64 surface with an improved surface finish, an example is shown in Figure 4-2.

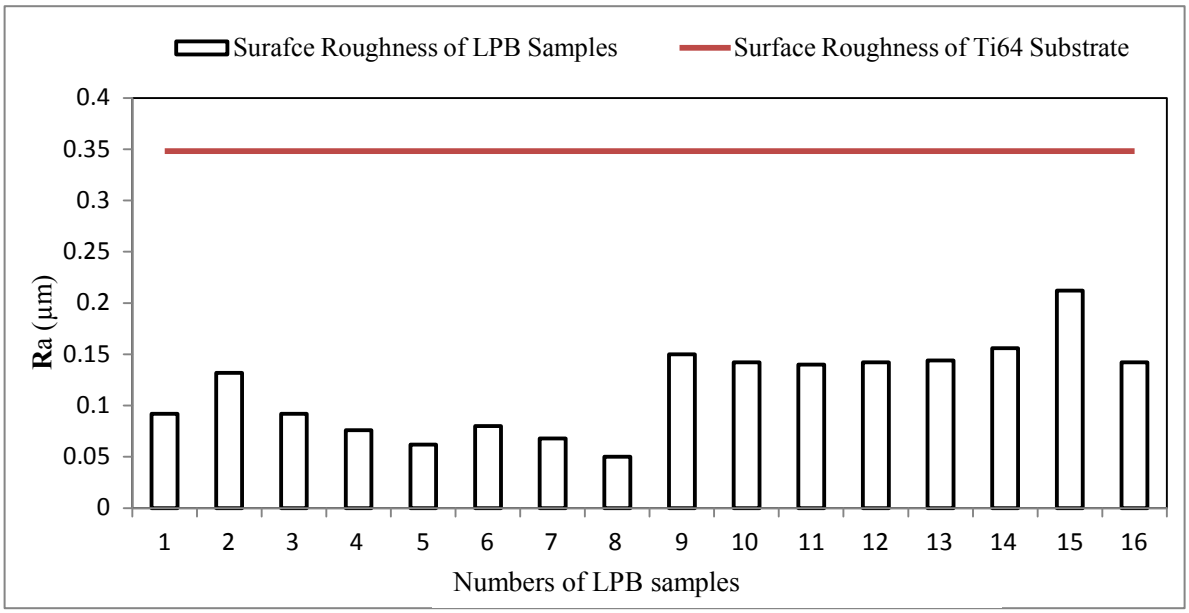

Figure 4-1 Surface roughness improvement on Ti64 after LPB treatment.

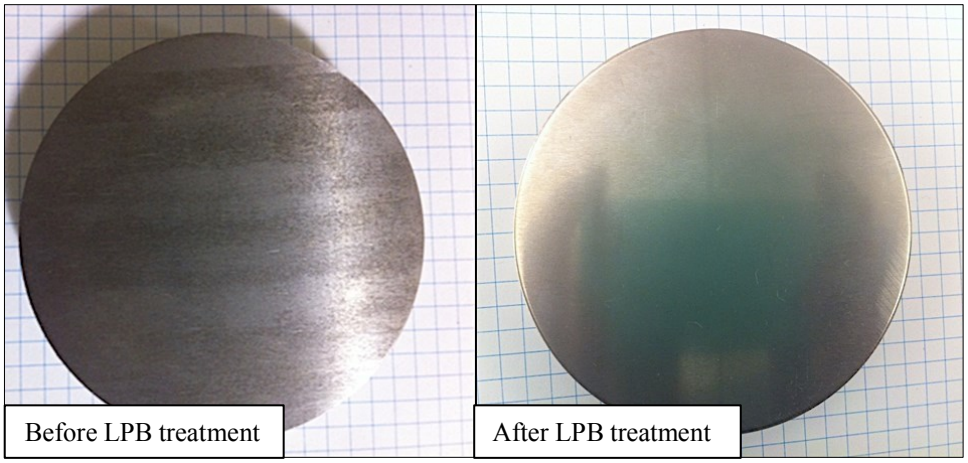

Figure 4-2 Surface finish of Ti64 disks before and after LPB treatment.

The Pareto chart, shown in Figure 4-3, indicates that the burnishing feed has the most dominant effect on the surface roughness of Ti64. An improvement of 0.07 μm in the surface finish of Ti64 could be induced by decreasing the burnishing feed (Factor B) from the high level (0. 20 mm/rev) to the low level (0.06 mm/rev). Moreover, the Factor B shows a positive value according to DOE analysis, suggesting that the feed rate of the LPB

process works directly proportional to the surface roughness value. Hence, in order to minimize the surface roughness value, it is advisable to set the burnishing feed at a low level.

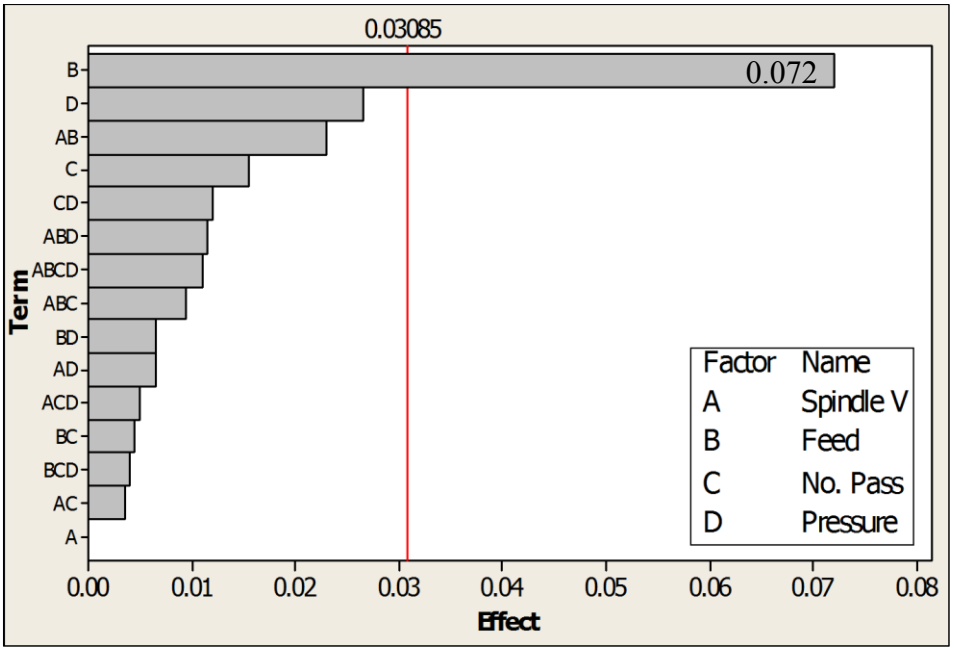

Figure 4-3 Pareto chart of Ra.

One of the full factorial methodology advantages over the one-factor-at-a-time experimental procedure is its ability to specify the interaction effect between any two factors. In general, treatments conducted with low level of feed rate resulted in lower **R**a, which means smoother surface finish. The response surface plots shown in Figure 4-4 highlight the interactions between the significant effect of the feed (Factor B) and the spindle velocity (Factor A), number of passes (Factor C) and the pressure (Factor D) on the **R**a.

It is worth noting that spindle velocity has little effect on **R**a when LPB was operated under high level of pressure (200 bar) for 3 passes. The response surface shown in Figure 4-4 (a) was dominated by the change of the feed rate. While under the LPB process parameters with low level of pressure (100 bar) for single pass, increasing the feed rate

showed no effect on the **R**a at high level of spindle velocity (Factor A), as shown in Figure 4-4 (d). The response surface in Figure 4-4 (d) showed an increasing trend of **R**a by increasing the spindle velocity at the low level of the feed rate, but a decreasing trend at the high level of the feed rate. Another interesting observation could be made in Figure 4-4 (c) and (f); the pressure showed a less pronounced effect on the **R**a at the LPB condition of high levels of the feed rate (0.20mm/rev), spindle velocity (150rpm) and number of passes (3 passes), as shown in Figure 4-4 (c). However, the response surface of Ra showed a decreasing trend by increasing the pressure at low levels of the feed rate (0.06mm/rev), spindle velocity (75rpm) and the number of passes (1 pass), as shown in Figure 4-4 (f).

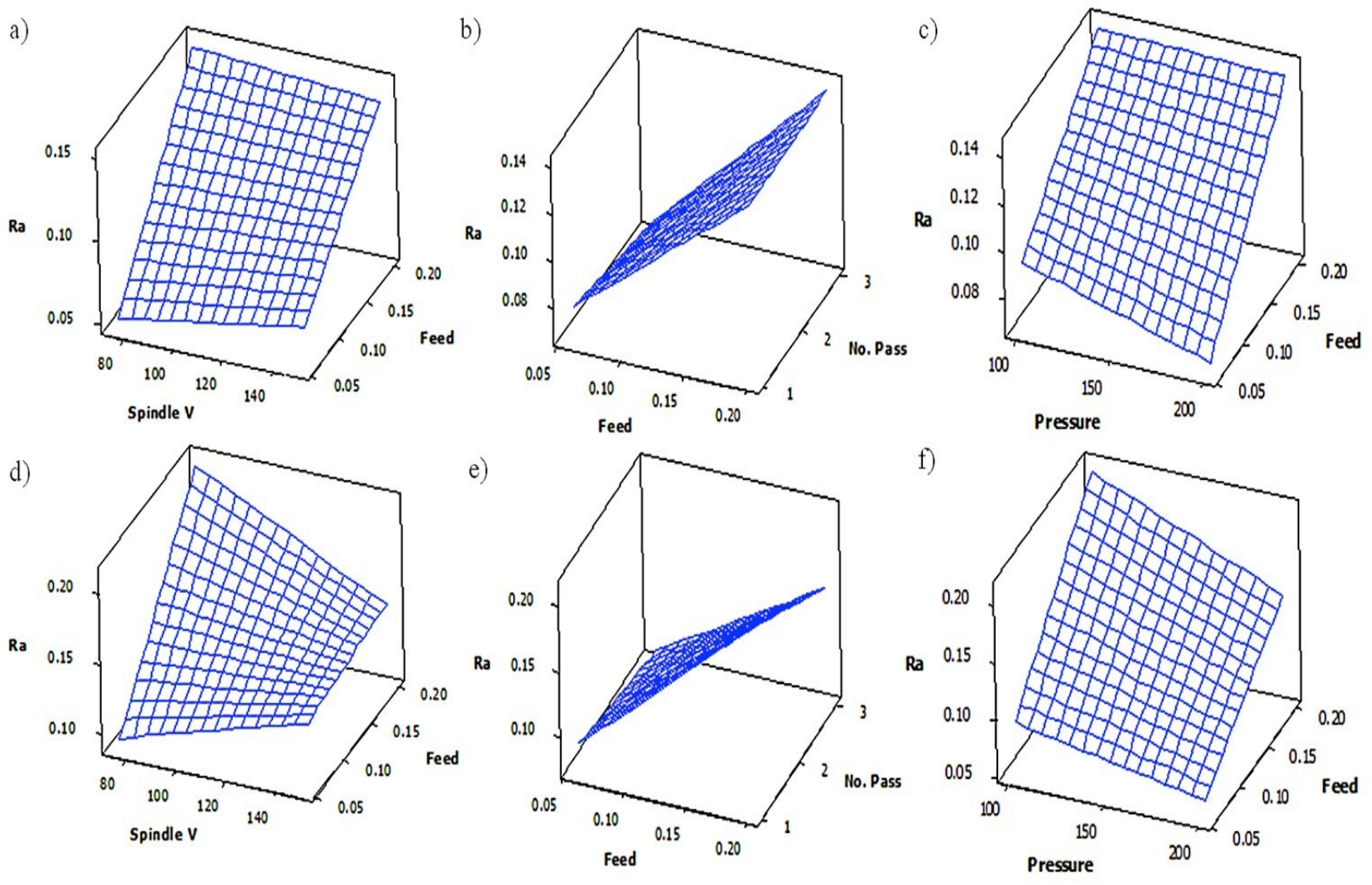

Figure 4-4 Response surface plots of Ra Vs: a) V, f at high level of No. Pass and P; b) f, No. Pass at high level of V and P; c) P, f at high level of V and No. Pass; d) V, f at low level of No. Pass and P; e) f, No. Pass at low level of V and P; f) P, f at low level of V and No. Pass.

4.3 Results of hardness measurements

4.3.1 DOE analysis for surface microhardness

As a surface enhancement technique, LPB is expected to improve the surface properties of the material. Results of surface microhardness measurements of the tested samples are listed in Tables 4-5 and 4-6, with the average of five readings for each sample.

Table 4-5 Results of surface microhardness of LPB samples.

LPB Sample #	Surface Microhardness (HV)					
	R1	R2	R3	R4	R5	Ave.
1	340.2	333.6	335	344.9	325.1	335.8
2	348.16	395.3	361.1	369.1	395.3	373.8
3	353.8	347.6	351.8	326.6	340.5	344.1
4	355.9	324.2	334.7	339.0	340.3	338.8
5	331.8	337.4	349.9	340.2	327.8	337.4
6	349.1	335.3	358.0	344.2	332.1	343.7
7	378.1	380.8	401.7	376.5	384.3	381.1
8	396.6	333.2	392.4	391.4	395.3	381.8
9	386.5	350.5	384.2	360.8	351.5	366.7
10	393.8	358.1	390.6	395.6	413.8	390.4
11	378.4	400.7	388.9	384.7	389.3	388.4
12	345.4	387.3	388	394.0	352.7	373.5
13	371	376.8	396.1	400.8	382.8	385.5
14	389.7	389.8	355.2	355.8	353.0	368.7
15	363.3	311.1	363.9	368.1	348.4	351.0
16	340.0	366.5	357.1	322.4	344.7	346.1

Table 4-6 Surface microhardness of Ti64 substrate

Ti64	Surface Microhardness (HV)					
	R1	R2	R3	R4	R5	Ave.
	310.8	297.3	308.0	302.1	291.9	302.0

A comparison between the surface microhardness of the LPB-treated and non-treated Ti64 is presented in Figure 4-5, indicating an increase of 10 - 30% in the surface microhardness of Ti64 after LPB treatment, the value varying with the different process conditions.

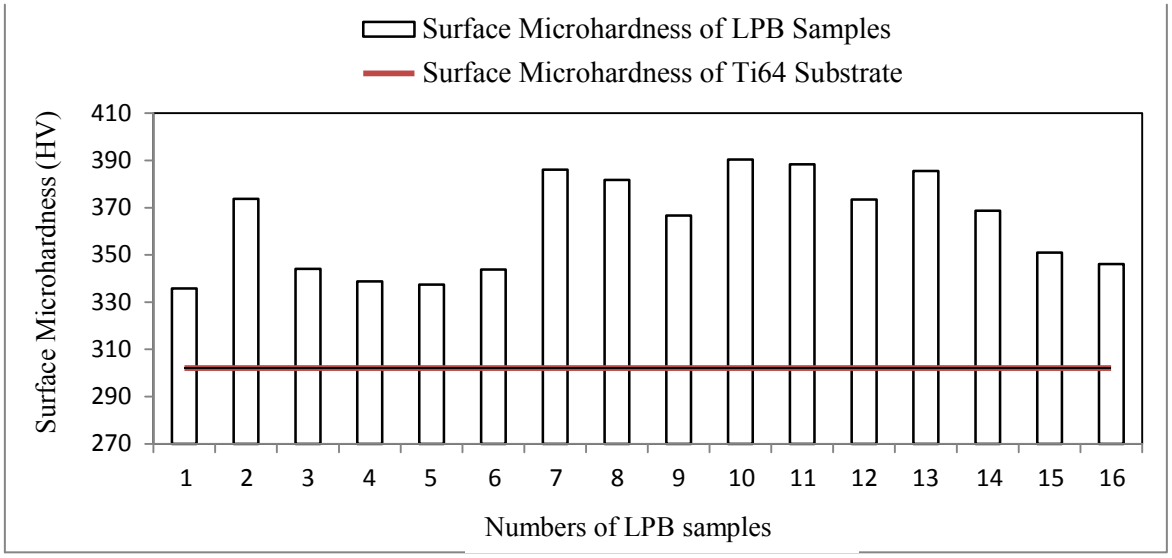

Figure 4-5 Comparison of the surface microhardness between the LPB treated and non-treated Ti64.

The Pareto chart shown in Figure 4-6 indicates that, the interaction effect (BCD) of the feed rate (Factor B), number of passes (Factor C) and pressure (Factor D) have the most significant effect on the surface microhardness of Ti64 at the 95% confidence level. In addition, the feed rate (Factor B) has a significant effect on the surface microhardness of Ti64. However, the level of its significance is less than that of the third order interaction effect, BCD. More details are provided by DOE analysis. The effect of the three-factor interaction (BCD) is inversely proportional (negative effect) to the magnitude of the surface microhardness of Ti64, while the feed rate has a directly proportional effect (positive effect) on the surface microhardness.

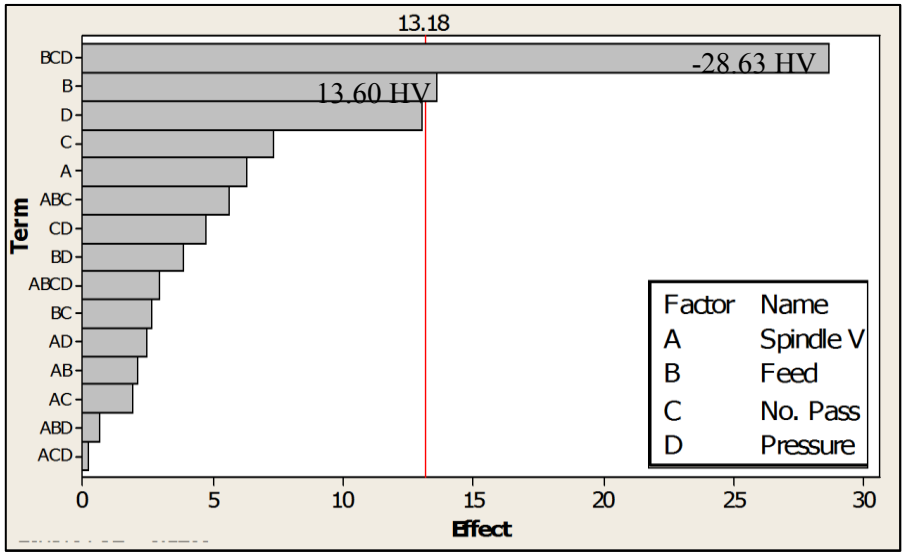

Figure 4-6 Pareto chart of the surface microhardness (HV).

Due to the presence of the significant three-factor interaction effect (BCD) on surface microhardness after LPB treatment, it is important to study the nature of interactions among the factors to obtain the optimized LPB condition for the sake of surface microhardness enhancement. As discussed above, in order to increase the surface microhardness of Ti64, the factors B, C and D should be combined in a way to build up a negative BCD effect, as presented in Table 4-7.

Table 4-7 Combinations of the parameters showing a negative BCD effect.

Third Order Interaction Effects BCD that are beneficial for surface microhardness	Surface Hardness (HV)	LPB Sample Number	Factors		
			B	C	D
			Feed	Number of passes	PRESSURE
1)	385.5 & 368.7	#13 & 14	+	+	-
2)	388.4 & 373.5	#10 & 11	+	-	+
3)	335.8 & 373.5	#1 & 2	-	-	-
4)	381.1 & 381.8	#7 & 8	-	+	+

Practical interpretations were examined with the help of the response surface plots to verify the obtained parametric effects of the LPB conditions listed in Table 4-7 on the surface microhardness of Ti64. The corresponding response surface plots are shown in Figure 4-7. A maximum microhardness value of about 390 HV on the response surface was

identified for all four LPB conditions listed in Table 4-7.

The results of the response surfaces indicate the dominance of the third order interaction effect (BCD) over the main effect (B), as shown in Figure 4-7 (b), (c) and (e). The surface plot in Figure 4-7 (b) reached the maximum values of surface microhardness at LPB conditions (2) and (4) listed in Table 4-7. The same observation could be made in Figure 4-7 (c) and (e); the surface plot reached the maximum values at the LPB condition (2) in Figure (c), and LPB condition (4) in Figure 4-7 (e). This is in accordance with the literature that, the main effects do not have much meaning when they are involved in significant interactions [82].

However, it is interesting to note that the pressure (Factor D) at low level of feed rate (Factor B) decreases the surface microhardness but increases it at high level of feed rate (Factor B) when the rest two factors (Factor A and Factor C) are set at their low level of values, as shown in Figure 4-7 (c). This explains the reason that a relatively smaller increment of surface microhardness value was observed in the LPB condition (3) listed in Table 4-7.

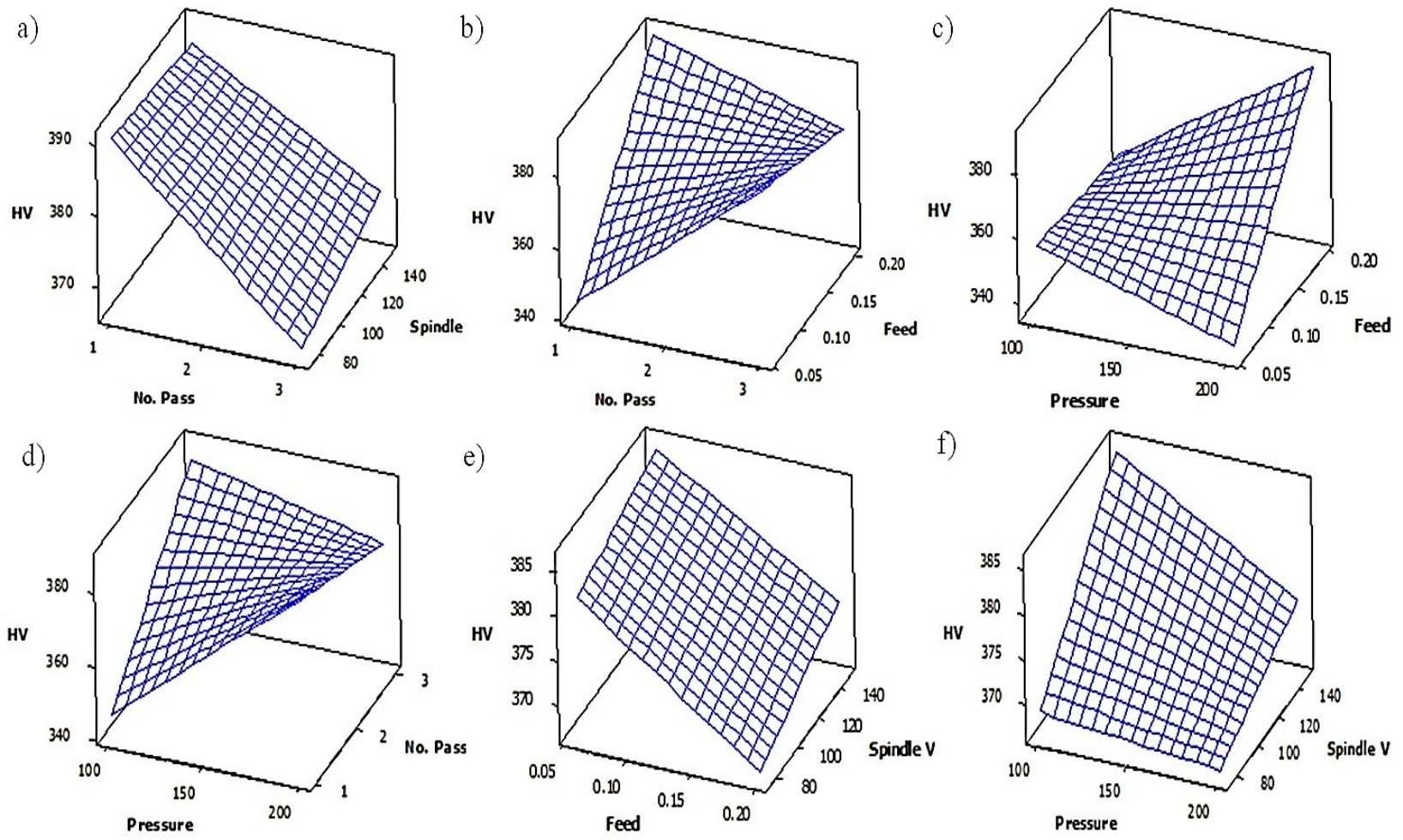

Figure 4-7 Response surface plots of surface microhardness Vs: a) V, No. Pass at high level of f and P; b) f, No. Pass at high level of V and P; c) P, f at low level of V and No. Pass; d) P, No. Pass at high level of f and V; e) f, Vat high level of V and P; f) P, V at high level of f and No. Pass.

4.3.2 In-depth hardness Profile

Two LPB treated samples (LPB #10 and LPB #15, shown in Table 4-8) were chosen for the in-depth hardness profile measurement with a nano-indentation tester. The only difference in the process parameters between these two LPB samples is the pressure. LPB #10 was treated with a high level of burnishing pressure (200 bar), while LPB #15 was treated with low burnishing pressure (100 bar). Two repeated tests were done for each sample to show the consistency of the results.

Based on the in-depth hardness profiles (Figures 4-8 to 4-10), comparisons were made between the LPB-treated samples and the virgin Ti64 samples. It showed that there was no certain trend for the changes in hardness for the LPB-treated Ti64 compared to that of the non-treated Ti64. Similar scattered readings of in-depth hardness were obtained in the measurements of both the present work and the literature [65]. The hardness values lie in the range of 4 GPa to 6 GPa in all measurements. The average values were given by the most matching trend line drawn in the profiles. It indicates that the in-depth hardness of LPB-treated and non-treated Ti64 have the same average value of 5 GPa. The fluctuation in microhardness could be due to the dual-phase (α and β) microstructure of Ti64, as the more brittle α phase is harder than the more ductile β phase. Moreover, the comparison of the in-depth hardness profiles between the LPB sample#10 and LPB sample #15 (Figures 4-8 and 4-9) indicates that the LPB pressure has little or no effect on the in-depth hardness.

Table 4-8 Process parameters of LPB sample #10 and #15.

LPB Sample #	A	B	C	D
	Spindle V (rpm)	Feed (mm/rev)	#Pass	Pressure (Bar)
10	75	0.20	1	200
15	75	0.20	1	100

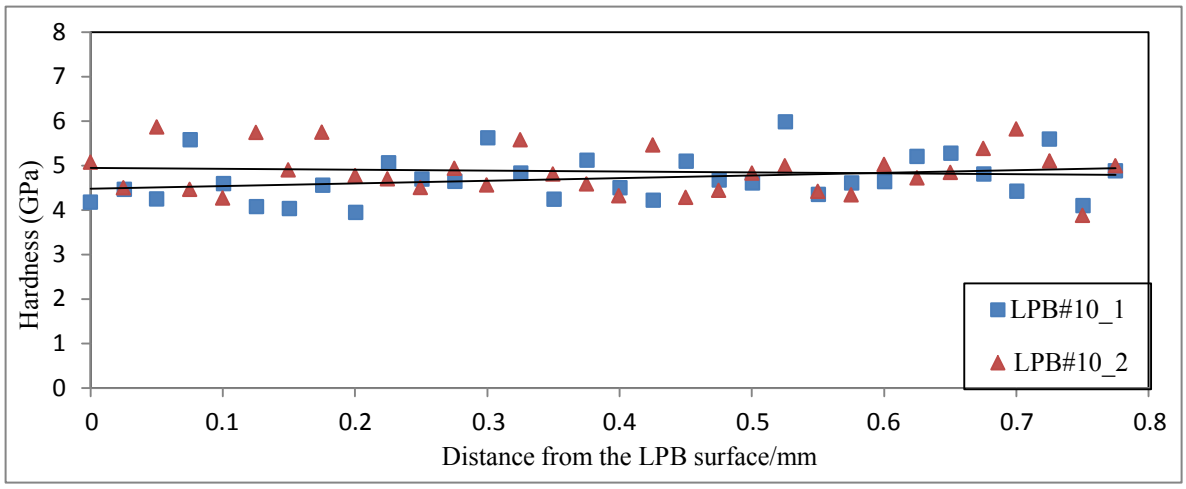

Figure 4-8 In-depth hardness profiles of LPB sample #10, replica #1 and #2.

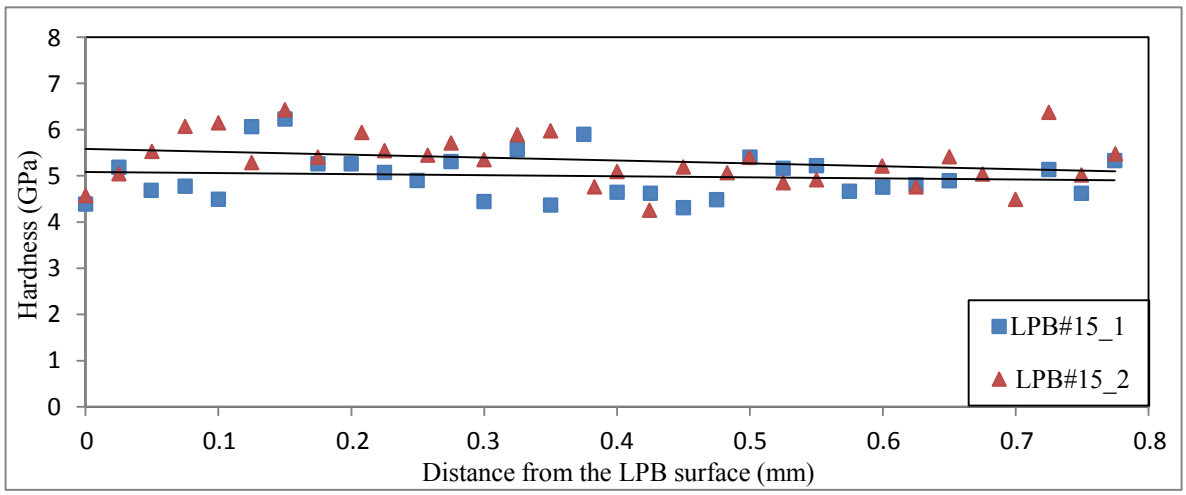

Figure 4-9 In-depth hardness profile of LPB sample #15, replica #1 and #2.

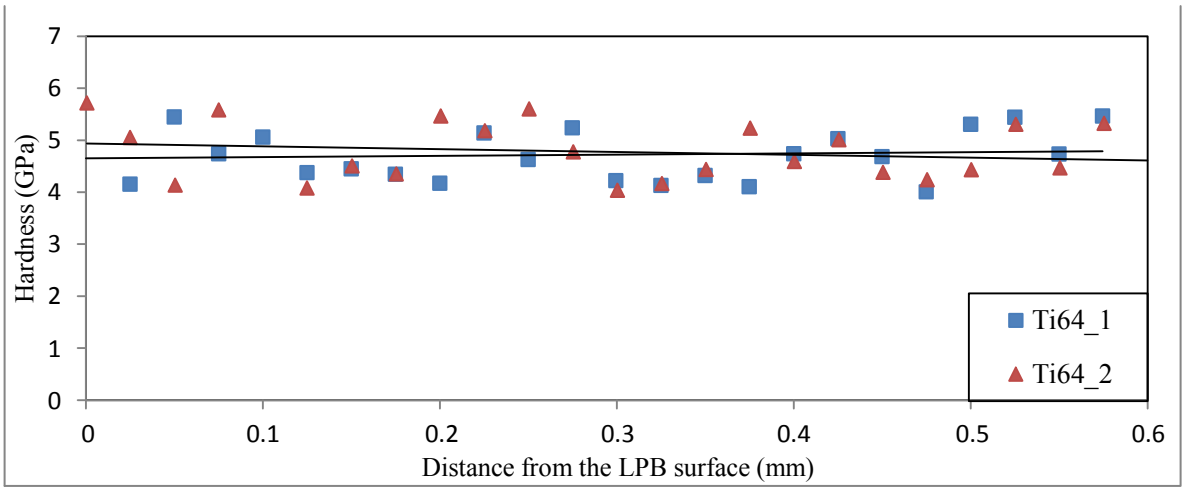

Figure 4-10 In-depth hardness profiles of non-treated Ti64, replica #1 and #2.

4.4 Residual stress distribution

The residual stress distributions of the 16 different LPB conditions were determined using the incremental hole-drilling method. Results from the individual target gauges are shown in Figures B-1 to B-3 (Appendix B). Each figure lists the relaxed strains recorded at 16 drilling depths. Within the data reduction program, the strain data was subjected to a moving average smoothing process and then reduced to normal stresses ($\sigma 1$ and $\sigma 3$) and shear stress ($\tau 13$). The distributions of both directions of residual stresses ($\sigma 1$ and $\sigma 3$) show little or no difference, thus, the discussion will be on $\sigma 1$ and it should be applied to $\sigma 3$ as well. The values of shear stress ($\tau 13$) are negligible, compared to $\sigma 1$ and $\sigma 3$.

The NPL Good Practice Guide [84] lists a number of contributors to stress uncertainty including factors arising from the component, the drilling process, the strain gauge and strain indicator. The strain gauge and indicator together are the greatest sources of uncertainty in the form of noise in the strain output. A random strain uncertainty in the range of ± 3 με applied to the strain data of gauges in this assessment produces uncertainties of ± 34 MPa in $\sigma 1$ and $\sigma 3$ stresses over a depth range of 16 μm to 112 μm.

This decreases to a minimum of ± 6 MPa at a depth of 512 μm and then increases again to ± 14 MPa at the final increment, because of reducing sensitivity. Uncertainties at other depths vary linearly between these values. Many of the other factors have been evaluated; the additional experimental error is estimated at ± 6%. Total uncertainty ranges over the depth range covered here may be calculated as:

- ± 70 MPa (= ± 34 MPa ± 6% of –600 MPa) at depth 16 μm,
- ± 88 MPa (= ± 34 MPa ± 6% of –900 MPa) at depth 112 μm,
- ± 8 MPa (= ± 6 MPa ± 6% of 30 MPa) at depth 512 μm,

• ± 16 MPa (= ± 14 MPa ± 6% of 30 MPa) at depth 1024 μm.

The DOE analysis was performed on the basis of the responses of maximum magnitude of residual stress (RS Max.) and the total depth of the residual stress (RS Depth).

4.4.1 DOE analysis for the maximum magnitude of the compressive residual stress

The Pareto chart in Figure 4-11 shows that the only LPB parameter significantly affecting the maximum magnitude of the compressive residual stress at 95% confidence level is the pressure (Factor D). The effect of the pressure (Factor D) is positive (227.63), indicating that the maximum magnitude of the compressive residual stress (RS Max.) works in direct proportion to the pressure. The Pareto chart (Figure 4-11) indicates that there would be an increment of about 230 MPa on the maximum magnitude of the compressive residual stress (RS Max.) by increasing the pressure from low level (100bar) to high level (200 bar).

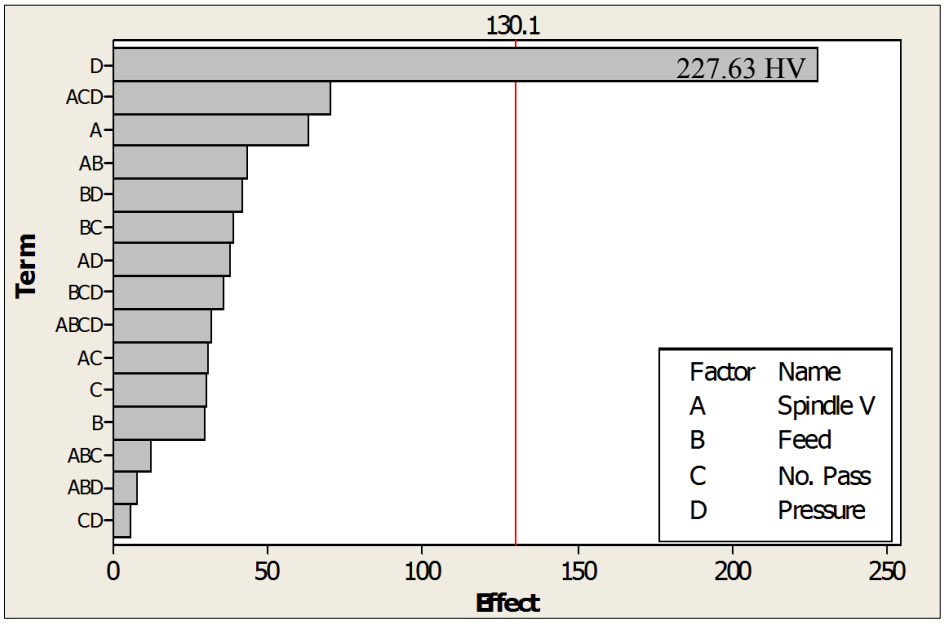

Figure 4-11 Pareto chart of the maximum magnitude (RS Max.) of the compressive residual stress.

The response surface plots, shown in Figure 4-12, are used to provide a practical interpretation of the effect of the LPB pressure, as well as its interactions with other main

effects on the response (RS Max.). Generally, it could be observed in these graphs that the response surfaces follow the trend of the LPB pressure, reaching a maximum compressive residual stress of about 1100 MPa at its high level (200 bar). The maximum increment of the response (RS. Max) shown in the plots lies in the range of 200 MPa to 300 MPa, which verifies the conclusion obtained from the Pareto chart.

It could be noted that the pressure (Factor D) leads the major trend of the respond surfaces of maximum magnitude of the compressive residual stresses; however, fluctuations in the response surfaces were observed due to the minor effects induced by other processing parameters of LPB. The spindle velocity (Factor A) showed more pronounced positive effect at high level of pressure at the LPB condition of low level of feed rate and number of passes, comparing to that of low level of pressure, high level of feed rate and number of passes, as shown in Figures 4-12 (a) and (d). The same observation could be made on the effect of the feed rate (Factor B) on the maximum magnitude of the compressive residual stresses, as shown in Figures 4-12 (b) and (e). The feed rate showed less effect at high level of pressure and number of passes, as shown in Figure 4-12 (b); while under low level of pressure and number of passes, the feed rate acts positively on the maximum magnitude of the compressive residual stresses at low pressure but negatively at high pressure, as shown in Figure 4-12 (e). Figures 4-12 (c) and (f) showed different effects of number of passes (Factor C) on the maximum magnitude of the compressive residual stresses under high and low levels of spindle velocity (Factor A) and feed rate (Factor B).

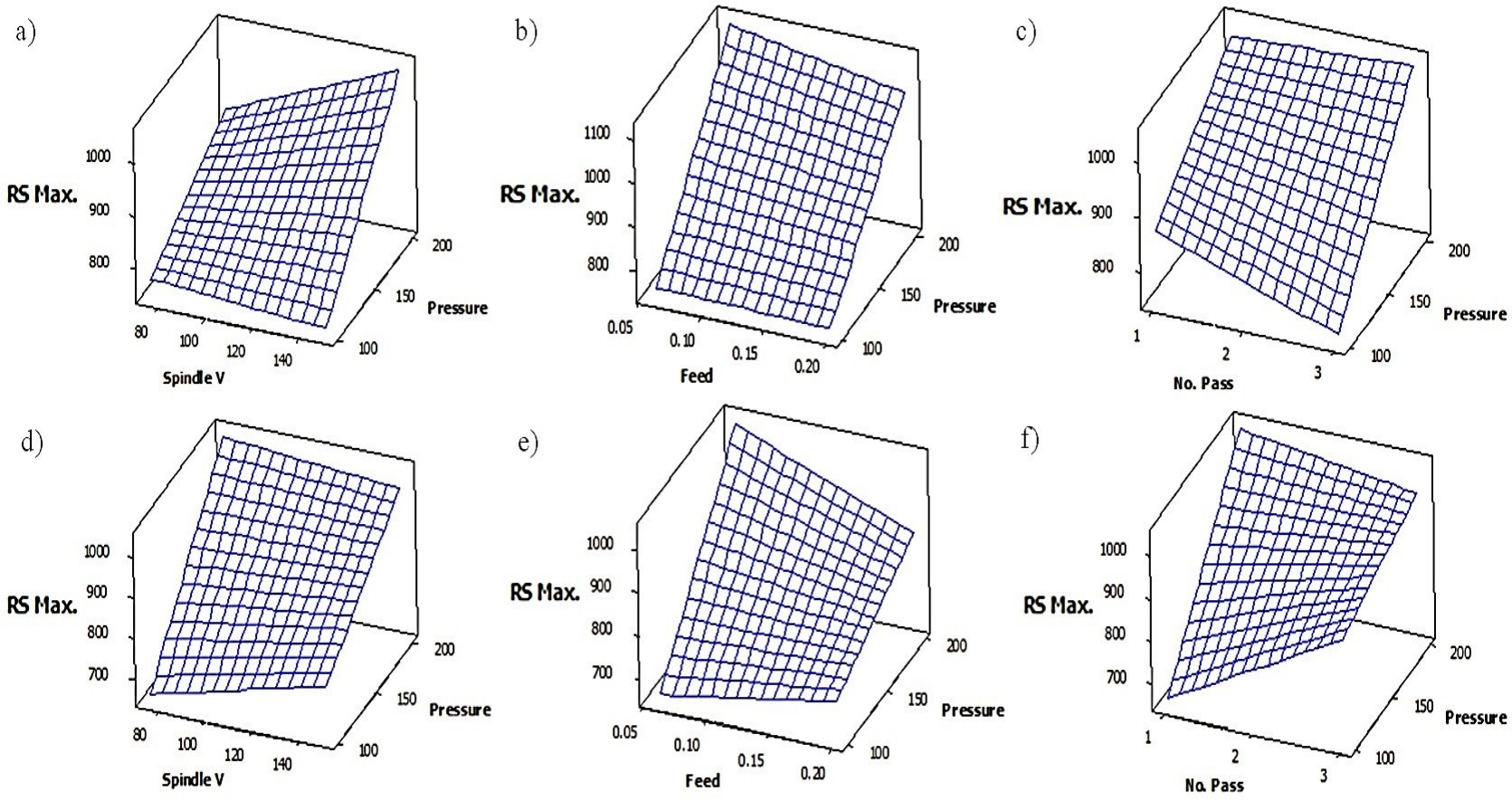

Figure 4-12 Response surface plots of RS Max. Vs: a) V, P at high level of f and No. Pass; b) f, P at high level of V and No. Pass; c) P, No. Pass at high level of V and f; d) V, P at low level of f and No. Pass; e) f, P at low level of V and No. Pass; f) P, No. Pass at low level of V and f.

4.4.2 DOE analysis for the total depth of residual stress

Two significant factors on the total depth of residual stress were identified in the Pareto chart in Figure 4-13, which are the main effects of pressure (Factor D) and feed rate (Factor B), in decreasing order of significance. The effect of the LPB feed rate (Factor B) on the total depth of the compressive residual stress layer is negative (-95.87 μm), while the effect of the pressure (Factor D) is positive (220.37 μm). This suggests that LPB treatment processed at low level of the feed rate (Factor B) with high level of the pressure (Factor D) is beneficial for increasing the total depth of the compressive residual stress layer. However, the extent of the influence of these two effects on the total depth of the residual stress layers varies as shown in the Pareto chart in Figure 4-13. The effect of the pressure (Factor D) on the total depth of the compressive residual stress is shown to be more than twice that of the feed rate (Factor B). This could be depicted in more details in the response surface plots, shown in Figure 4-14. When the feed rate (Factor B) was set at a fixed level, the response surface showed an increment of 300 μm in the total depth of the compressive residual stress layer by increasing the pressure (Factor D) from low level to high level, as shown in Figure 4-14 (d). While fixing the pressure (Factor D) at a certain level, the increment in the total depth of the compressive residual stress layer, induced by decreasing the feed rate (Factor B) from high level to low level is about 150 μm maximum, as shown in Figure 4-14 (a). It indicates that, the effect of the pressure (Factor D) is more dominant on the total depth of the compressive residual stress layer.

Furthermore, the interactions between the significant factors and the remaining factors are examined with the help of the response surfaces. For the interaction between the two significant factors (Factor B and D), the response surfaces reach the maximum value

of 660 µm at a feed rate (Factor B) of 0.06 mm/rev (low level) and a pressure (Factor D) of 200 bar (high level). Hence, it is preferable to apply larger pressure during LPB on the surface of Ti64 in order to obtain a deeper compressive residual stress layer. The usage of a low level of feed rate will achieve the same objective of gaining a deeper compressive residual stress layer, but the improvement will be relatively mild. According to the present work, a surface compression layer more than 660 µm deep could be obtained using a higher pressure (larger than 200 bar) and a lower feed rate (0.06 mm/rev) in the LPB process. However, it is worth noting that the feed rate does not decrease the depth of the compressive residual stress layer significantly at high level of pressure, spindle velocity and number of passes, as shown in Figures 4-14 (b) and (c).

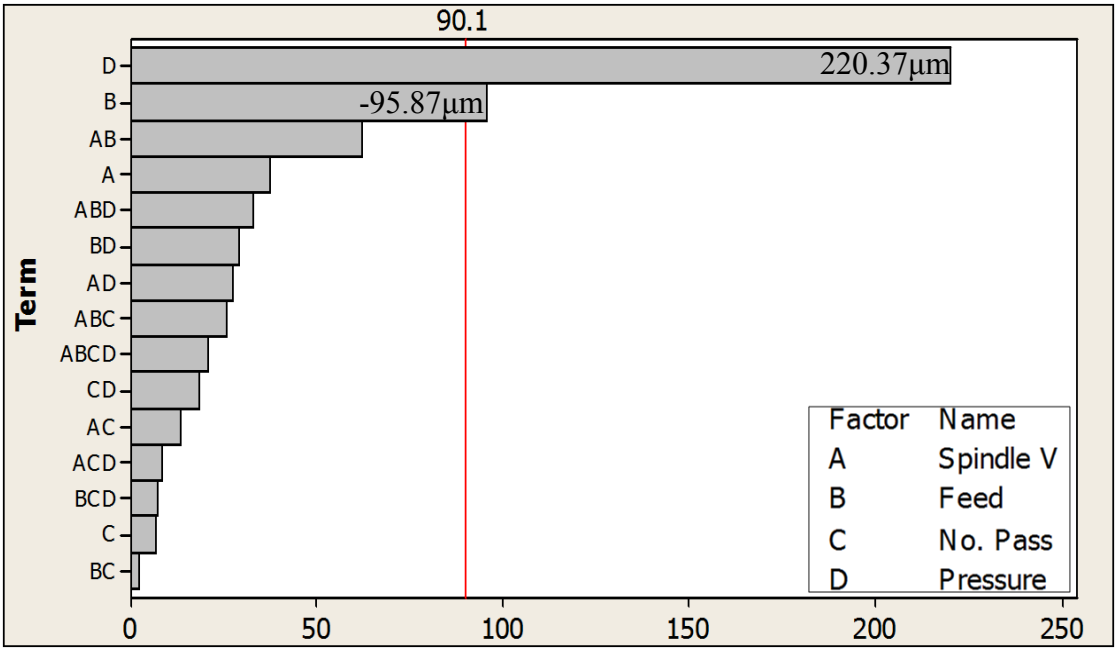

Figure 4-13 Pareto chart of the total depth (RS Depth) of the compressive residual stress layer.

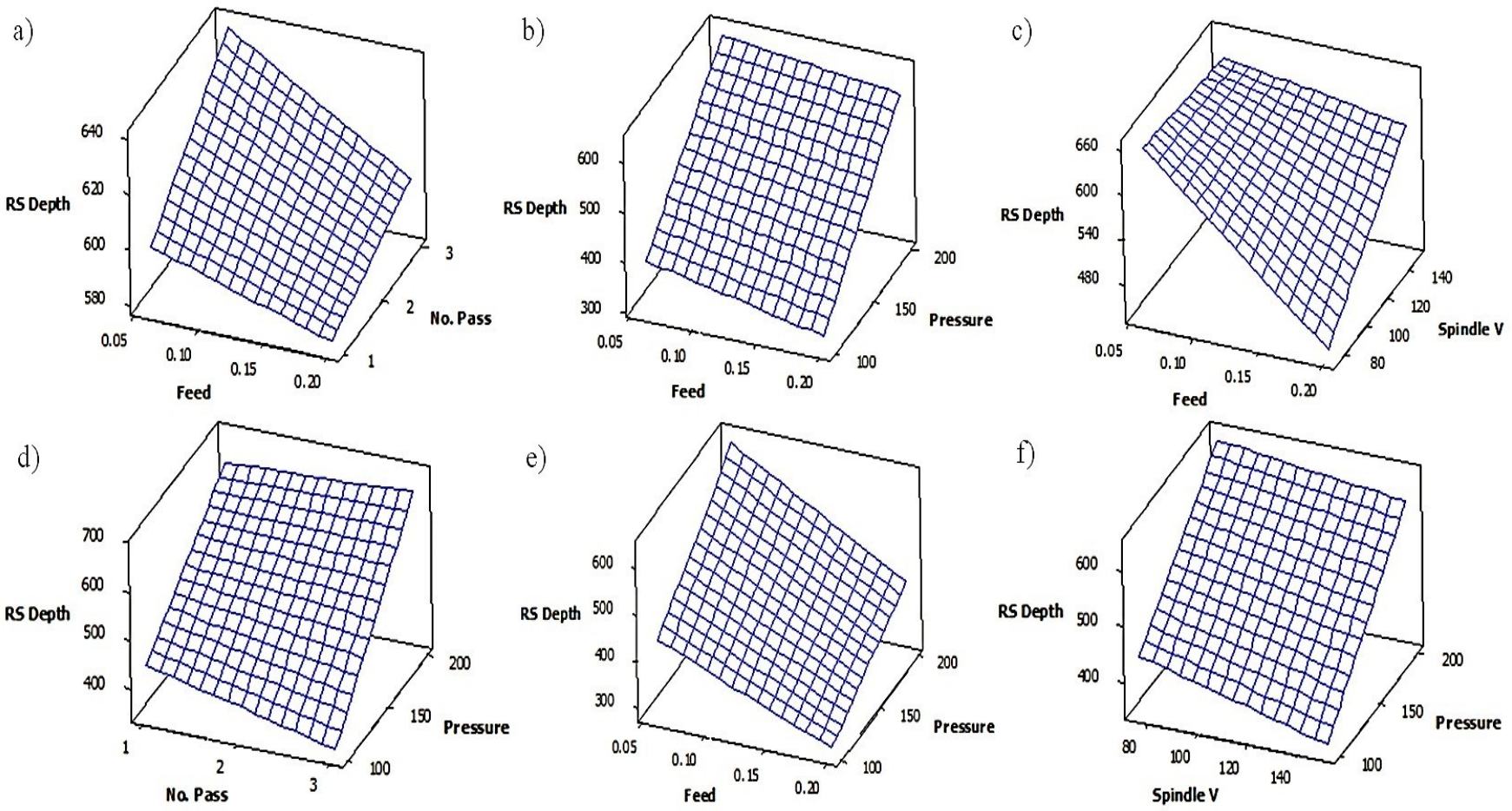

Figure 4-14 Response surface plots of RS Depth Vs: a) f, P at high level of V and No. Pass; b) f, P at high level of V and No. Pass; c) f, V at high level of P and No. Pass; d) No. Pass, P at low level of f and V; e) f, P at low level of V and No. Pass; f) P, V at low level of f and No. Pass.

The following conclusions can be drawn based on the DOE analyses shown above. The residual stress distributions of all the 16 LPB treated samples generally fall into two categories as shown in Figures 4-15 and 4-16. The LPB pressure (Factor D) played an important role in both the magnitude and the depth of the induced compressive residual stress. A Ti64 substrate surface treated by the LPB with a high level of pressure (200 bar) had a deeper compressive residual stress layer (about 660 μm) and larger magnitude (about 1100 MPa) compressive residual stress, as shown in Figure 4-15. While the samples burnished at low pressure (100 bar) resulted in a 350 μm depth of compressive residual stress layer with a maximum compressive residual stress of about 800 MPa, as shown in Figure 4-16.

The DOE analysis also took the depth, where the maximum compressive residual stress occurs, as a response. However, there was no significant effect shown in this response. Meaning that the maximum compressive residual stress always occurs at the subsurface (about 100 μm away from the LPB surface) of Ti64, and this is not affected by the LPB processing parameters. Distributions of stresses from the majority of the gauges show that the most intense levels of compression do not occur at the surface but at depths within the range of 80 μm to 160 μm. At depths beyond the compressive peak, stresses are seen to decay, returning to the tensile sub-surface coupon stresses at depths between 300 μm and 660 μm.

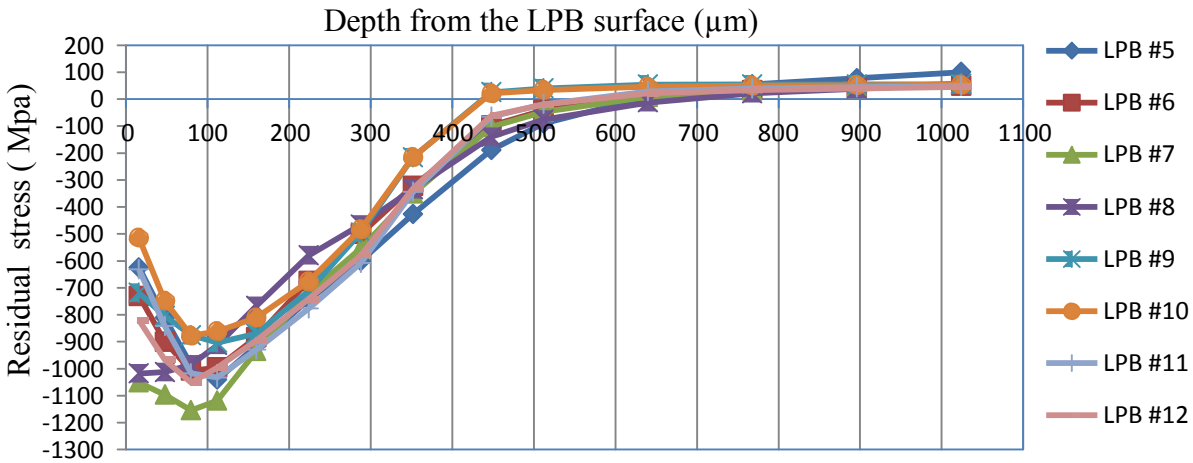

Figure 4-15 Residual stress distribution of Ti64 operated under high LPB pressure.

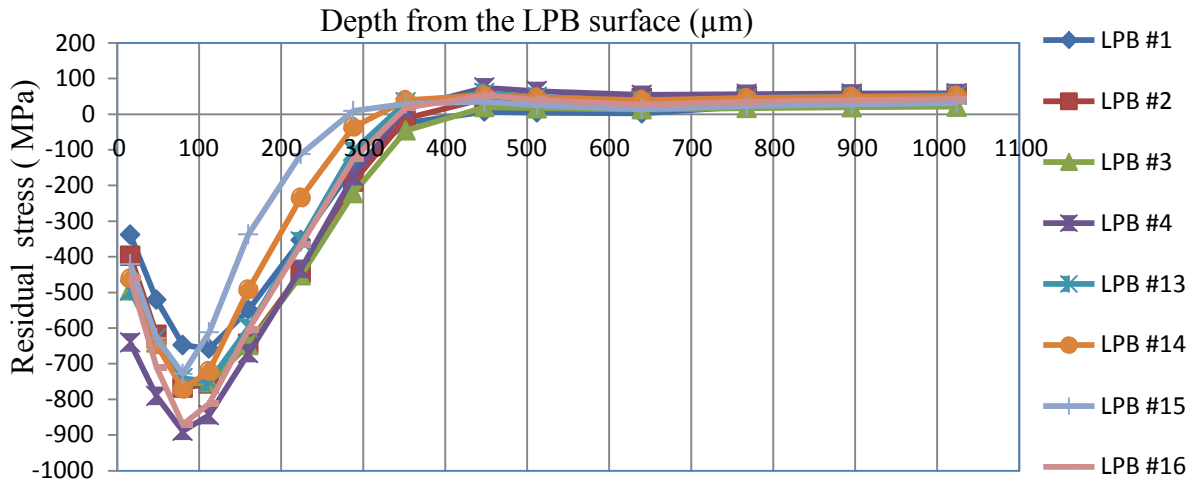

Figure 4-16 Residual stress distribution of Ti64 operated under low LPB pressure.

Residual stress measurements were conducted with similar incremental hole-drilling (IHD) method at Concordia University. Comparable results were obtained from the Concordia system and the StressCraft system discussed in the previous section on a different location of the same LPB-treated sample. The initial stress level of the virgin Ti64 was measured using the Concordia system, as shown in Figure 4-17. It indicates that the as received annealed Ti64 has an almost unstressed surface condition, as the residual stress values lie in the range of -100 MPa to +100 MPa, which are negligible compared to the residual stress induced by the LPB process.

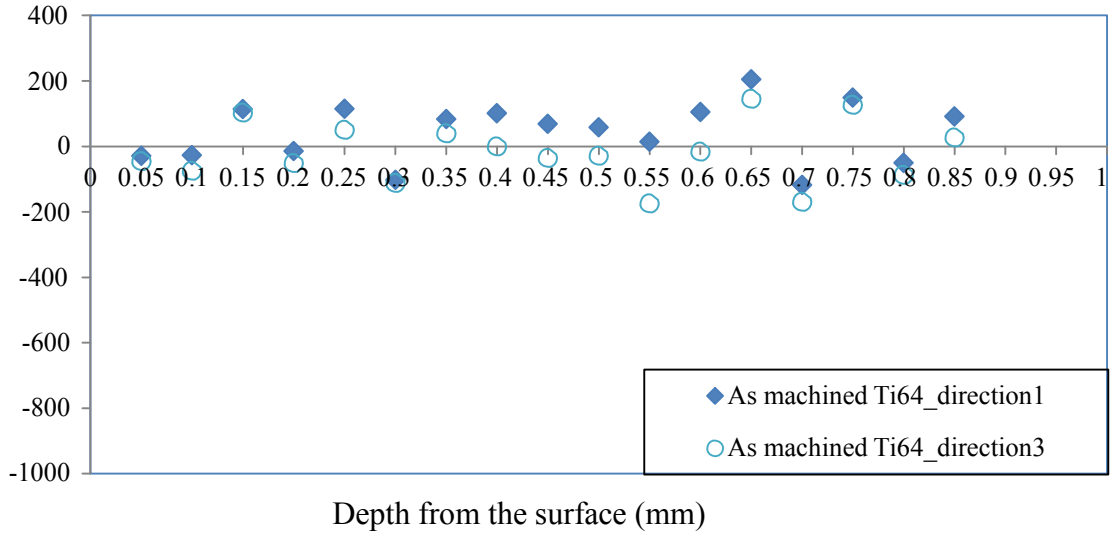

Figure 4-17 Residual stress distribution of non-treated Ti64.

Furthermore, the effects of LPB processing parameters on residual stress distribution are illustrated in Figure 4-18. The maximum magnitude of the compressive residual stress increases with increasing LPB pressure, while the depth where it occurs remains the same. To apply deeper compressive residual stress on the surface of Ti64, it is advisable to burnish the samples at lower feed rate with increasing pressure up to a limit while maintaining low plasticity condition.

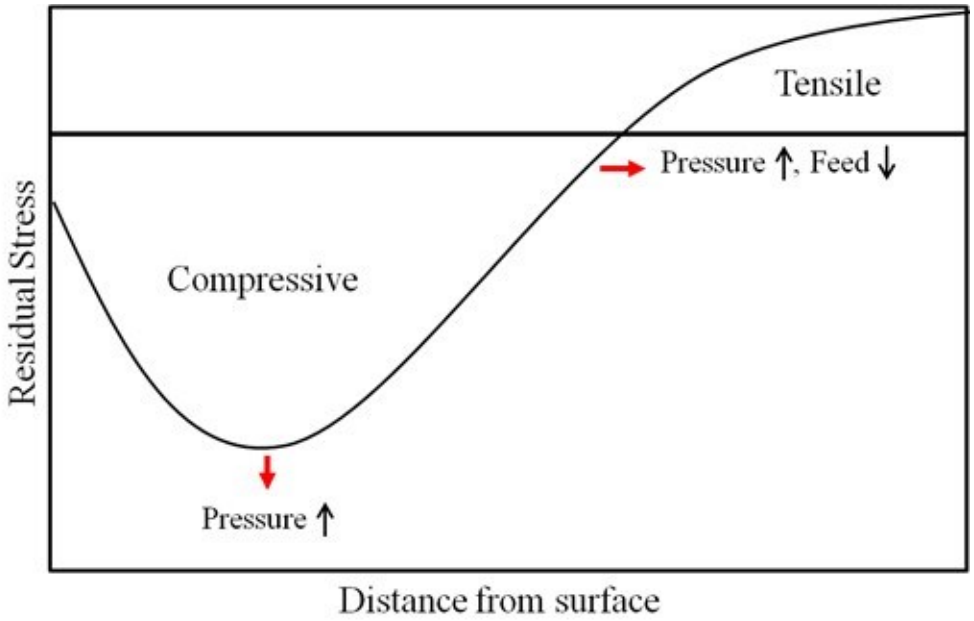

Figure 4-18 The effects of LPB processing parameters on residual stress distribution.

4.5 Liquid impingement erosion (LIE) tests

The above results have indicated the best LPB conditions to produce deep and high magnitude compressive residual stresses and high surface microhardness values. These are projected to be the most likely LPB conditions that could improve LIE resistance of Ti64 alloy. Thus, the sample types to be tested with LIE are LPB sample #6, #7 and #8 as discussed before.

The LIE curve is characterized with five major stages: incubation, acceleration, maximum erosion, deceleration and terminal erosion stage, as described in the literature review section. The erosion rate in the last two stages of the LIE curve usually decreases to a lower value, which may either remain relatively steady or may fluctuate unpredictably [9]. Hence, the discussions of the current LIE test results of LPB treated Ti64 samples are mainly focused on the initial three stages of the erosion curve: incubation stage, acceleration stage and maximum erosion rate stage.

LIE testing conditions with two different water droplet sizes (460 μm and 630 μm) at two impact speeds 250 m/s and 350 m/s) were used to test the LPB samples and the reference Ti64 sample. For each combination of LIE parameters, the tests were repeated twice to verify the consistency of the obtained results. The cumulative mass loss versus time and the number of impingements curves were plotted based on the LIE test results. The details are discussed in the following section.

In order to evaluate the effect of compressive residual stress on the LIE performance of Ti64, three LPB treated samples (Sample #6, #7 and #8) with significantly higher compressive residual stress (about 1000 MPa, as shown in Figure 4-19) were used

in the tests. The surface of the reference Ti64 sample is considered as stress free, as shown in Figure 4-19.

The LPB processing parameters of the tested samples are shown in Table 4-9, and their corresponding surface microhardness and surface roughness are shown in Table 4-10. Nevertheless, the three LPB samples are similar in terms of the residual stress distribution and the surface microhardness. The virgin Ti64 reference samples were polished down to an average surface roughness of 0.082 μm.

Table 4-9 The LPB processing parameters of LPB #6, #7 and #8.

LPB Sample #	Spindle V (rpm)	Feed (mm/rev)	#Pass	Pressure (Bar)
6	150	0.06	1	200
7	150	0.06	3	200
8	75	0.06	3	200

Table 4-10 The surface microhardness and surface roughness of LPB #6, #7 and #8.

LPB Sample #	Surface Microhardness/HV	Surface Roughness/ μm
6	343.74	0.08
7	381.06	0.068
8	381.78	0.05

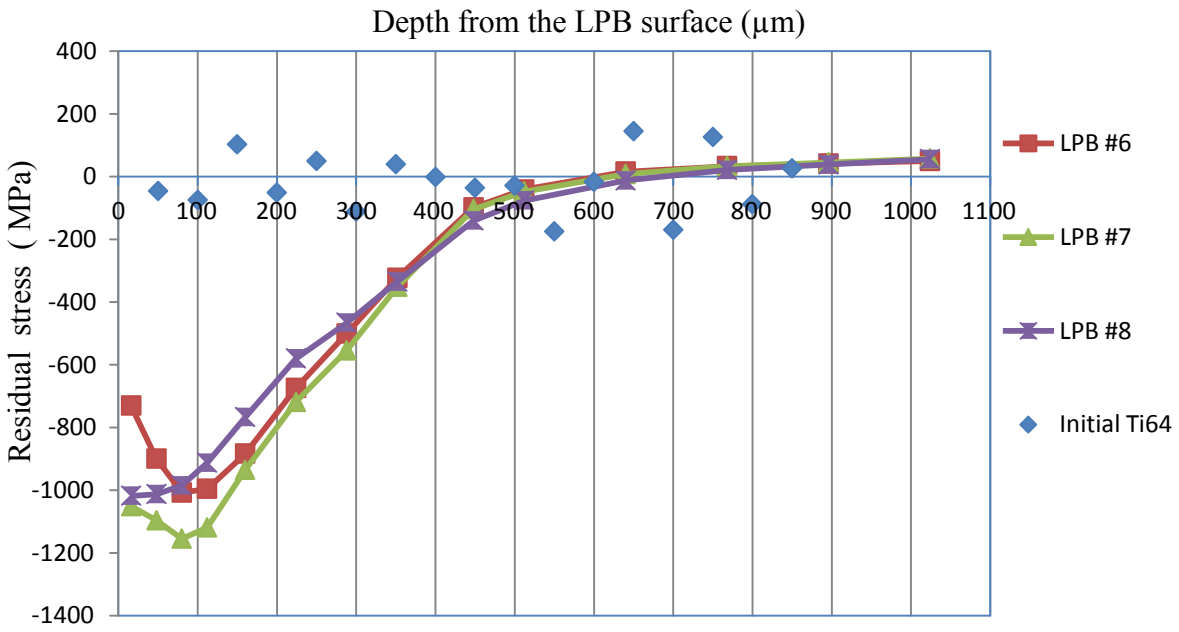

Figure 4-19 Residual stress distribution of the LPB samples #6, #7, #8 and the non-treated Ti64

Two different nozzle sizes were used in the LIE tests to generate two different sizes of water droplets. According to the ASTM standard G73-10 [85], "With drops, there will usually be a size distribution, and in most cases it will be necessary to determine that distribution by photography and analysis of the photographs". Hence, in the present study, droplet size distribution was studied using high-speed imaging system as mentioned in the experimental methodology section.

Figures 4-20 and 4-21 show the water droplet size distribution for the 400 µm and 600 µm nozzles, respectively. The diameters of 200 droplets were measured for each nozzle. Measurements were done in a vacuum glass box as mentioned in the experimental section, simulating the same test conditions for the LIE tests. The 400 µm nozzle generated droplet sizes with an average of 460 µm, while, for the 600 µm nozzle, the water droplet size has an average of 630 µm.

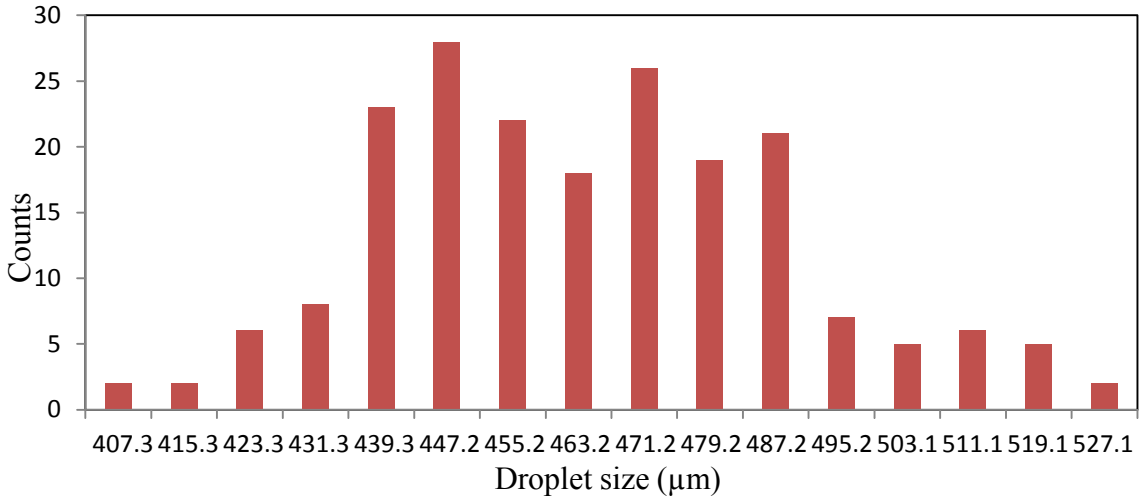

Figure 4-20 Droplet size distribution of 460 µm droplets

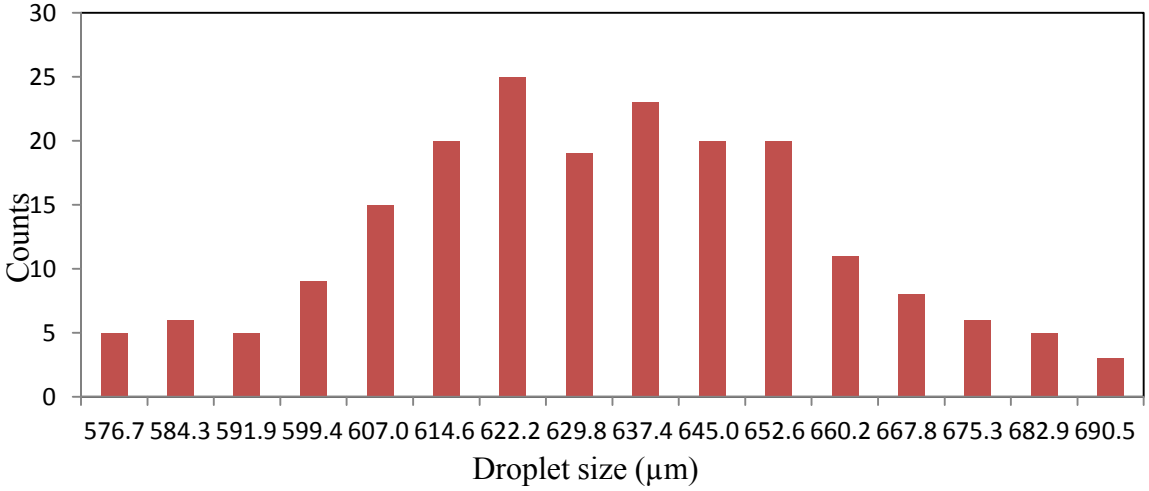

Figure 4-21 Droplet size distribution of 640 µm droplets

A high-speed camera (6000 frames per second) was used to capture images of the flow of the water droplets as shown in Figures 4-22 and 4-23, respectively. As a result, the number of impingements per revolution for each sample was counted. The 8 mm distance marked on Figures 4-22 and 4-23, respectively, this corresponds to the width of the test samples. Therefore, for the 460 µm droplets, the number of impingements is approximately 6 droplets/revolution, while that of 600-µm droplets is 4 droplets/revolution.

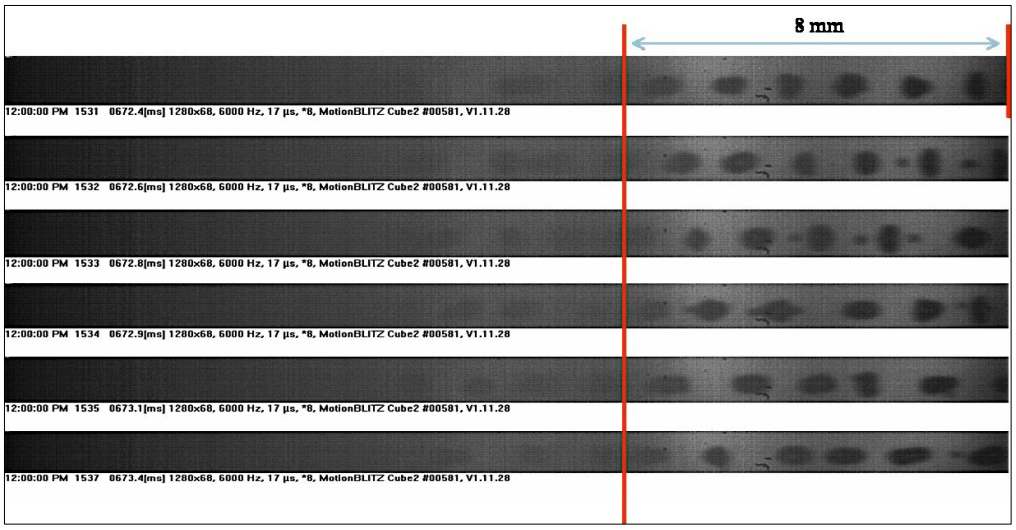

Figure 4-22 High-speed (6000 fps) images for 460 µm droplets

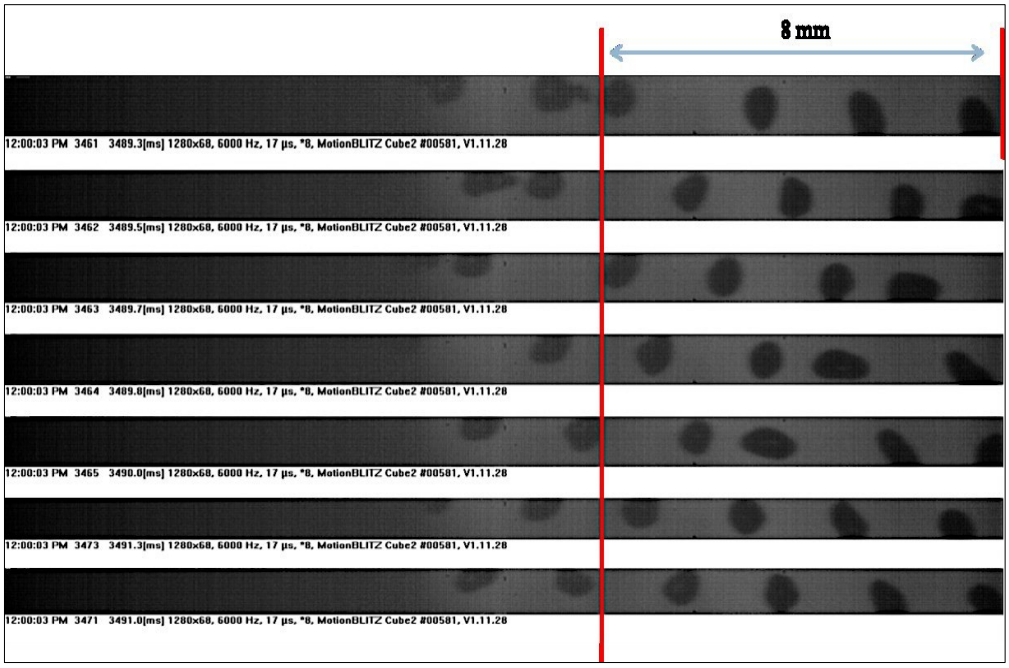

Figure 4-23 High-speed (6000 fps) images for 630-µm droplets

According to the measurements shown above, equation (2) can be used to compute the number of water droplet impingements (N_i) that are causing the erosion of the test specimens over time.

$$N_{impingement} = N_{spr} \times RPM \times t_e \quad (2)$$

where N_{spr} is the number of droplets hitting the sample each complete rotation (6 drop/revolution for the 460 µm droplets and 4 in the case of 640 µm), RPM is the number

of rotations per minute and t_e is the time of exposure in minutes.

4.5.1 LIE test results for 460μm droplets

1) 250 m/s impact speed (10,000 rpm)

The erosion curves representing the LIE test results of the LPB treated samples versus the reference Ti64 samples are shown in Figures 4-24 and 4-25. All four curves followed the typical LIE pattern. The first stage was the incubation period, followed by an acceleration of the erosion rate until it reached the peak and then the steady state erosion. The erosion rate then gradually decayed with time (or impingements).

Characterization of the nominal incubation period and maximum erosion rate are considered as the preferred evaluation method for presenting the LIE curves. According to the ASTM standard G73-10 [85], the maximum slope is determined by drawing a straight line that best represents the maximum rate stage of the test, while the incubation period (t_0) is obtained from the interception of the straight line with the x-axis (exposure time), as shown in Figure 4-26.

The incubation periods and the maximum erosion rates were determined for both tests following this standard and the results are listed in Table 4-11.

Table 4-11 Characterizations of the LIE curves

LIE tests with 460μm droplets at 250m/s impact speed	Samples for LIE tests	Incubation period t_0 (minute)	Maximum erosion rate (g/minute)	Ending Time for the third stage of LIE (minute)
Test #1	LPB #6	34	0.0002	80
	Ti64_1	32	0.0002	80
Test #2	LPB #7	30	0.0002	94
	Ti64_2	29	0.0002	96

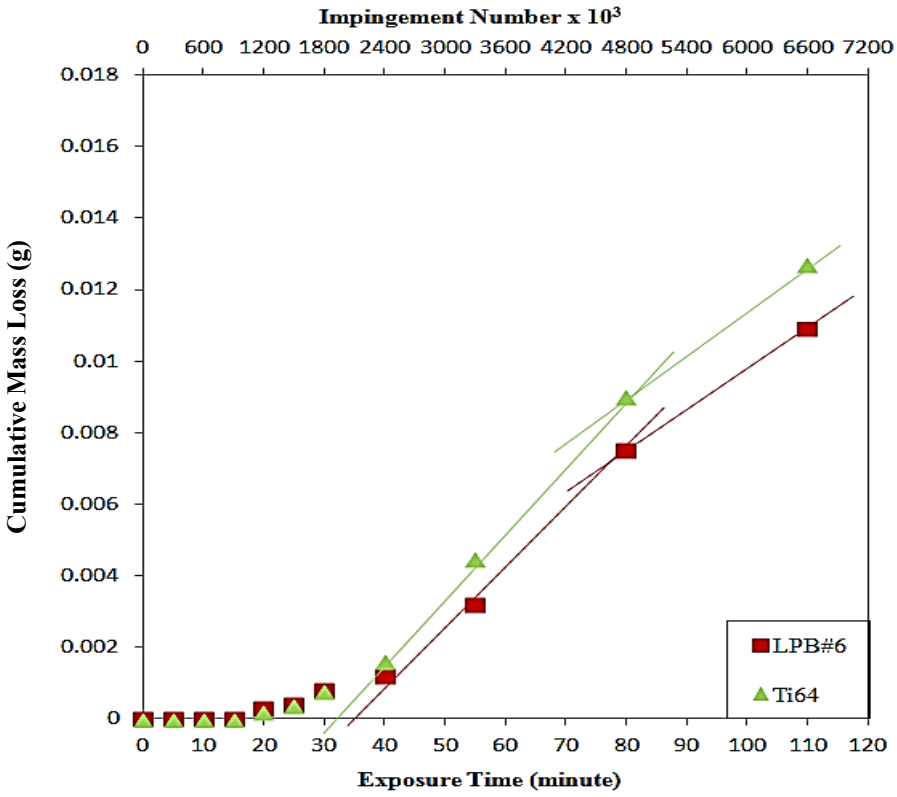

Figure 4-24 Erosion curves of LPB sample #6 in reference to virgin Ti64 at 250m/s with 400µ droplets

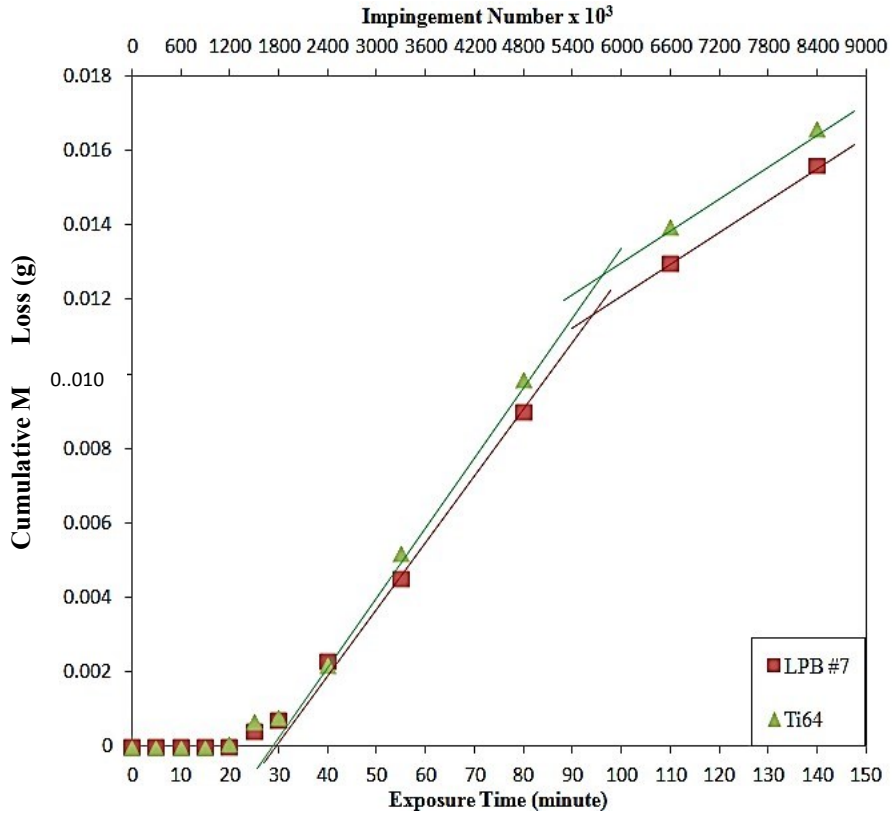

Figure 4-25 Erosion curves of LPB sample #7 in reference to virgin Ti64 at 250m/s with 400µ droplets

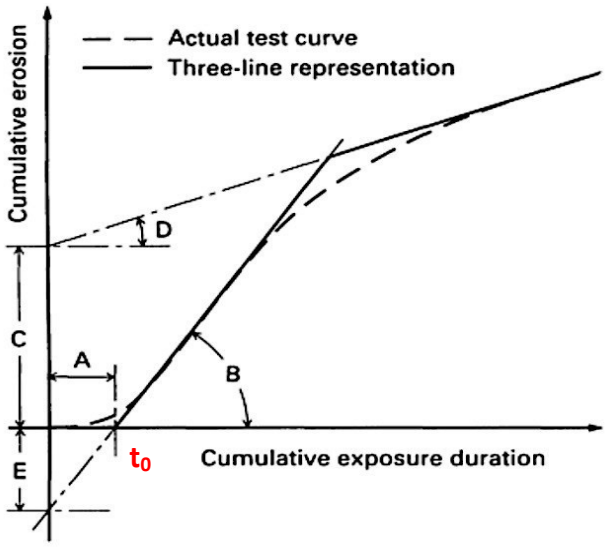

Figure 4-26 Maximum erosion rate determination method, where, A is nominal incubation period; B is representing the maximum erosion rate; D represents the terminal erosion rate [8].

The incubation period of LPB sample #6 and the reference Ti64 sample in test 1 (Figure 4-24) is 34 minutes and 32 minutes (as shown by the interceptions of the maximum-erosion-rate lines with the horizontal axis). The maximum erosion rate is 0.0002 gram/minute for both LPB sample #6 and the non-treated Ti64 sample. The third stage ends after 80 minutes in both LIE curves and the erosion rates continue to decrease with a similar erosion rate. A relatively consistent incubation periods were observed in the LIE curves of LPB sample #7 and the reference Ti64 sample used in test 2 (Figure 4-25), which are 30 minutes for LPB sample #7 and 29 minutes for the non-treated Ti64 sample. The maximum erosion rates are the same (0.0002 grams/min) for the two tests.

The slight variation in the LIE performance of the LPB samples and the virgin Ti64 samples in these two tests could be considered within the error limits.

The two LPB samples used in both tests have no significant difference in terms of the residual stress distribution, as shown in Table 10. It could be assumed that, the significantly different compressive residual stress levels between the LPB treated (1100

MPa) and the virgin Ti64 samples (considered as stress free 0 MPa) had little or no effect on the LIE performance.

Furthermore, the changes in the exposed surface of the tested samples at the same time interval during the LIE tests are shown in Figures 4-27 (test 1) and 4-28 (test 2). In both cases of the LPB treated and non-treated Ti64, the exposed surface showed no measurable material removal, but relatively shiny tracks due to the water droplet impingements during the incubation period. Once the small pitting formed, the erosion rate started to increase (acceleration stage), leading to the enlargement of the pits into a crater and more material removal from other parts of the exposed surface. Moreover, the craters coalesced as the erosion rate continuously increased in the third stage of LIE (maximum erosion rate stage) and eventually resulted in the formation of the erosion line across the width of the exposed surface. Both the depth and the width of the crater were enlarged during the repeated impingements.

It is interesting to note that the material removal at the initial stage for the non-treated Ti64 surface started with small but deep pitting. While for the LPB treated surface, it started with forming wide but shallow pitting, suggesting that the erosion or material removal might be limited only to the subsurface having compressive residual stress during the initial stages of LIE. However, the mass loss at the same period of the LIE tests has no significant difference in both LPB treated and non-treated Ti64 samples, as could also be observed in the macrographs (Figures 4-27 and 4-28).

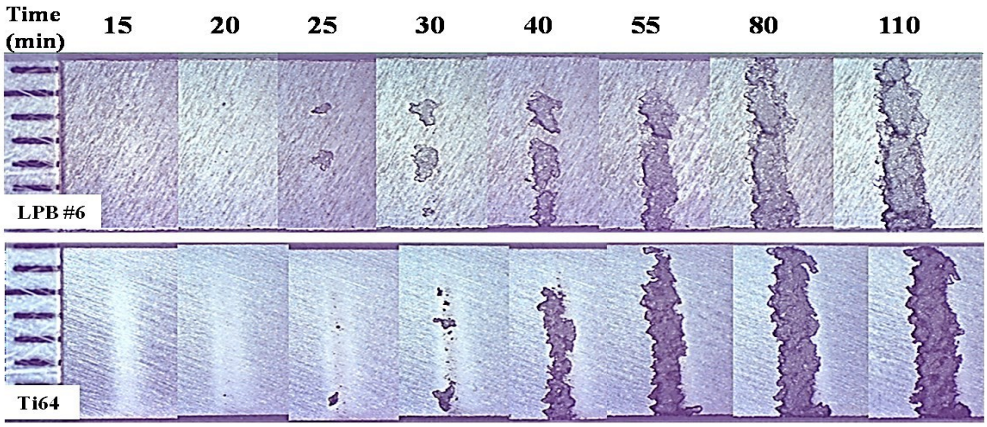

Figure 4-27 Changes in the exposed surface of LPB treated and non-treated Ti64 during the LIE test at 250m/s with 400µ droplets, test #1.

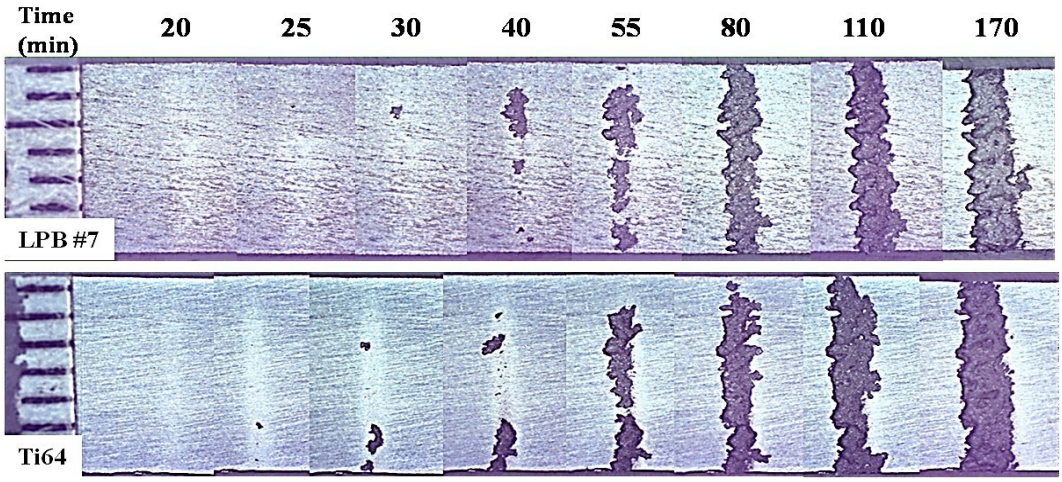

Figure 4-28 Changes in the exposed surface of LPB treated and non-treated Ti64 during the LIE test at 250m/s with 400µ droplets, test # 2.

2) 350 m/s impact speed (14,000 rpm)

Higher speed LIE tests (350 m/s) were performed with 460µm droplets size on two LPB samples (#7 and #8) versus two reference samples of Ti64. The results are shown in Figures 4-29 and 4-30. By following the ASTM standard G73-10 [85], the incubation periods and the maximum erosion rates of the LIE curves are summarized in Table 4-12.

Table 4-12 Characterizations of the LIE curves

LIE tests with 460μm droplets at 350m/s impact speed	Samples for LIE tests	Incubation period t_0 (minute)	Maximum erosion rate (g/minute)	End Time of the third stage of LIE (minute)
Test #1	LPB #7	3	0.0018	15
	TI64_1	3	0.0018	15
Test #2	LPB #8	3	0.0018	21
	TI64_2	3	0.0018	21

It is clearly shown in the erosion curves that there is no significant difference in the behavior of LPB treated and the virgin Ti64 samples in both cases. Both test 1 (LPB sample #7 and reference Ti64) and test 2 (LPB sample #8 and reference Ti64) showed an incubation period of 3 minutes. Moreover, the trends in both figures did not show any variation in performance as erosion evolves. The acceleration stage ended for all samples after 6 minutes. Erosion rates of all four samples increased to its maximum value of around 0.0018 grams/min in the third stage followed by the same gradual decrease trends in the erosion rate till the end of the tests.

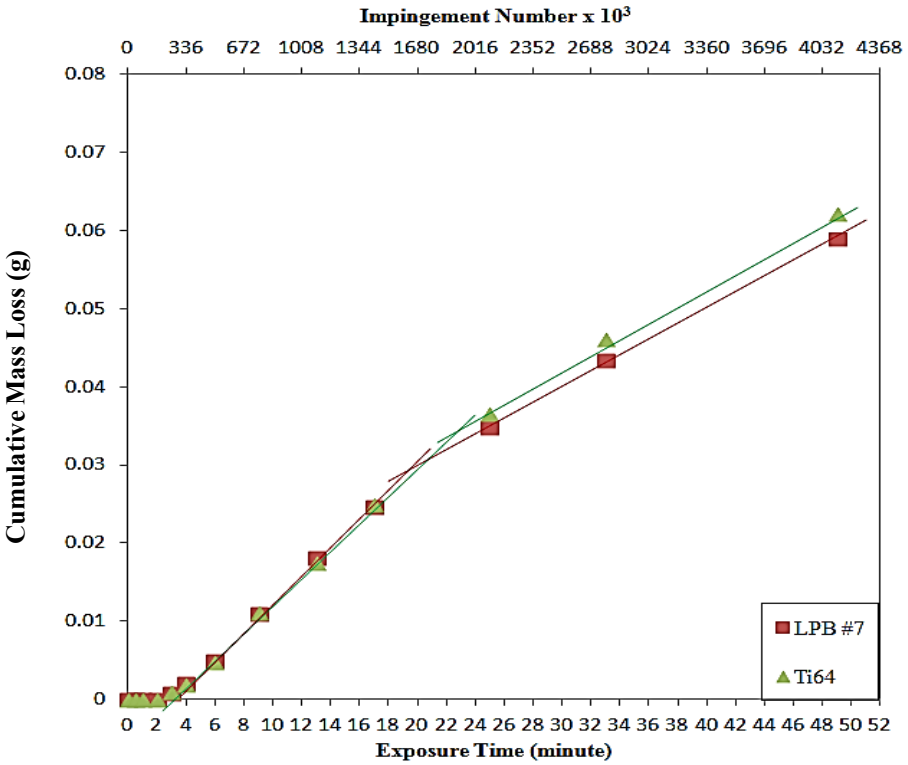

Figure 4-29 Erosion curves of LPB sample #7 with virgin Ti64 with LIE tests with 400µ droplets at 350m/s impact speed.

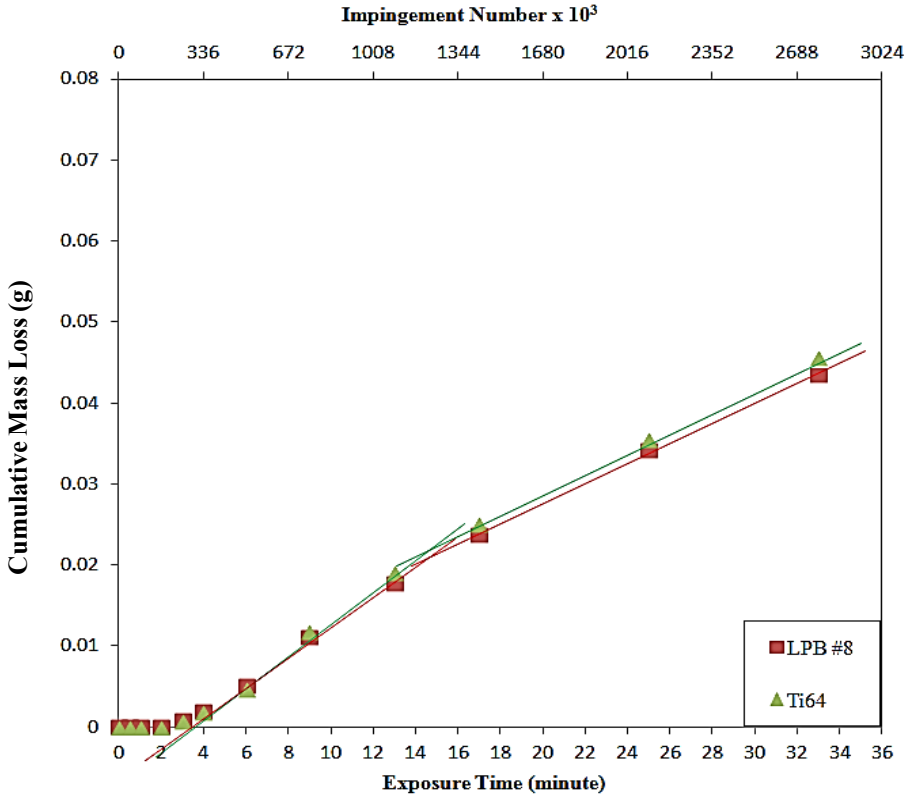

Figure 4-30 Erosion curves of LPB sample #8 with virgin Ti64 with 400µ droplets at 350m/s impact speed.

The changes of the exposed surface of the LPB treated and non-treated Ti64 samples at the same time interval during the LIE test were observed, as shown in Figure 4-31 (test 1) and Figure 4-32 (test 2). Compared to the macrographs of the exposed surface of the tests done with 400-µm droplets (Figure 4-27 and Figure 4-28), the small pitting initiation started earlier or after a shorter exposure time of the LIE tests as could be easily observed in Figure 4-31 and Figure 4-32. Moreover, the crater appeared to be much wider and larger at 350 m/s. It suggested that more severe erosion damage was induced by the higher impact speed (350 m/s) with the same droplet size (460 µm) impingements.

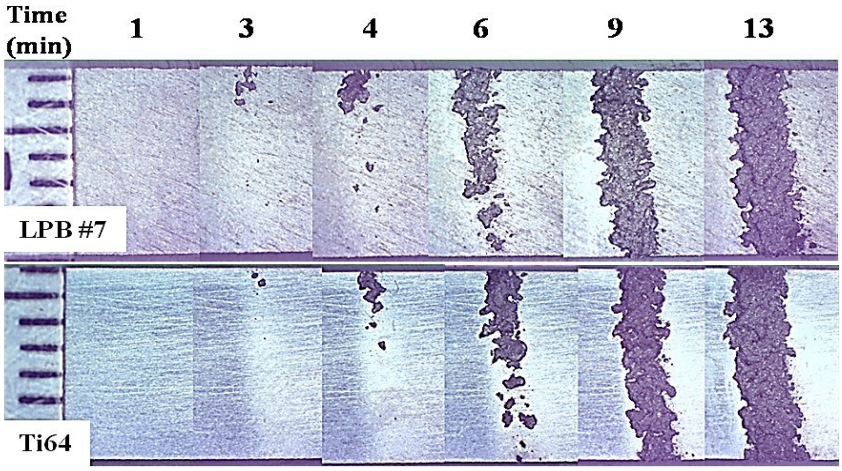

Figure 4-31 Changes in the exposed surface of LPB treated and non-treated Ti64 during the LIE with 460µ droplets at 350m/s impact speed, test 1.

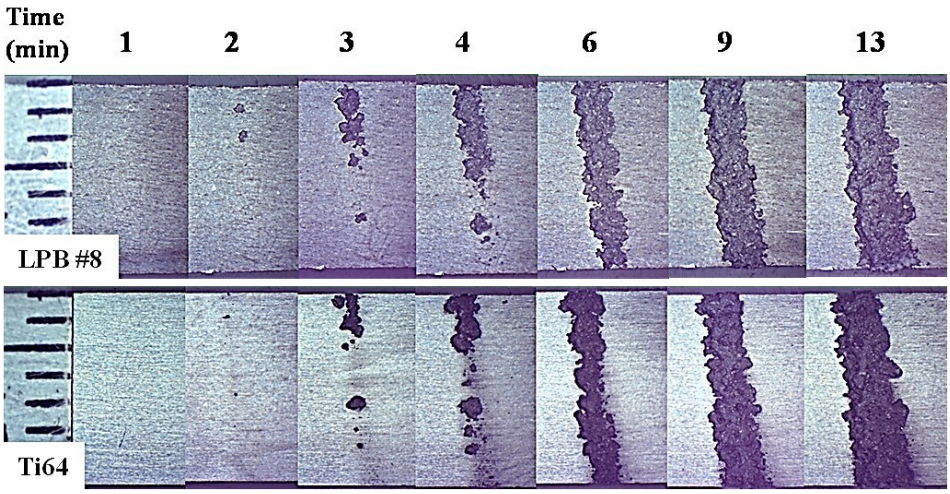

Figure 4-32 Changes in the exposed surface of LPB treated and non-treated Ti64 during the LIE with 460µ droplets at 350m/s impact speed, test 2.

4.5.2 LIE test results with 630 µm droplets

1) 250 m/s impact speed (10,000 rpm)

For the LIE test using 630 µm droplets at 250 m/s impact speed, two tests were done using LPB samples #7 and #8 versus the Ti64 reference samples. The obtained LIE curves are shown in Figures 4-33 and 4-34. It is obvious that for both tests, there is no significant difference in their LIE behavior between LPB treated and untreated Ti64 samples.

The incubation periods and the maximum erosion rates of all the LIE curves are determined and the results are listed in Table 4-13. The incubation period of LPB sample #7 and the reference Ti64 sample in test 1 (Figure 4-33) is 24 minutes and 28 minutes, respectively. The maximum erosion rates are calculated to be 0.0002 gram/minute for both LPB sample #7 and the non-treated Ti64 sample. The third stages end after 120 minutes in both LIE curves and the erosion rates continue to decrease with a similar erosion rate.

The maximum erosion rate was determined by the most matching lines of the maximum erosion rates of the LIE curves in Figure 4-33, which were 0.0002 gram/minute for both curves in test 1. And the incubation period of the two LIE curves in test 1 (Figure 4-33) are 24 minutes for LPB #7 and 28 minutes for Ti64 sample, as shown in Table 4-13.

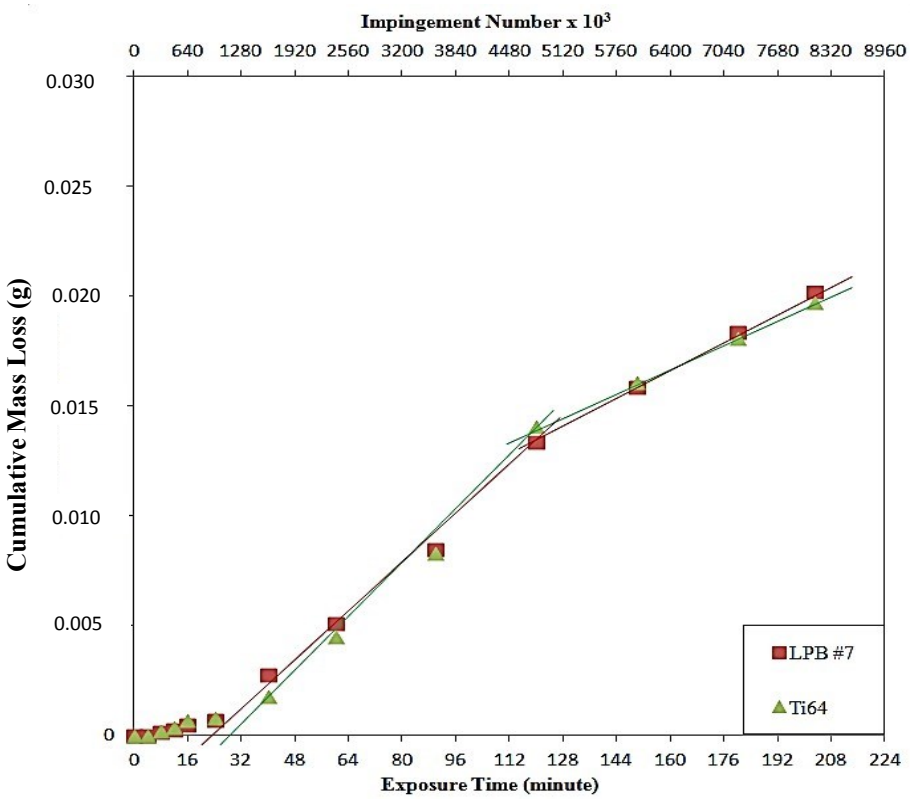

Figure 4-33 Erosion curves of LPB sample #7 with virgin Ti64 with 600µ droplets at 250m/s impact speed.

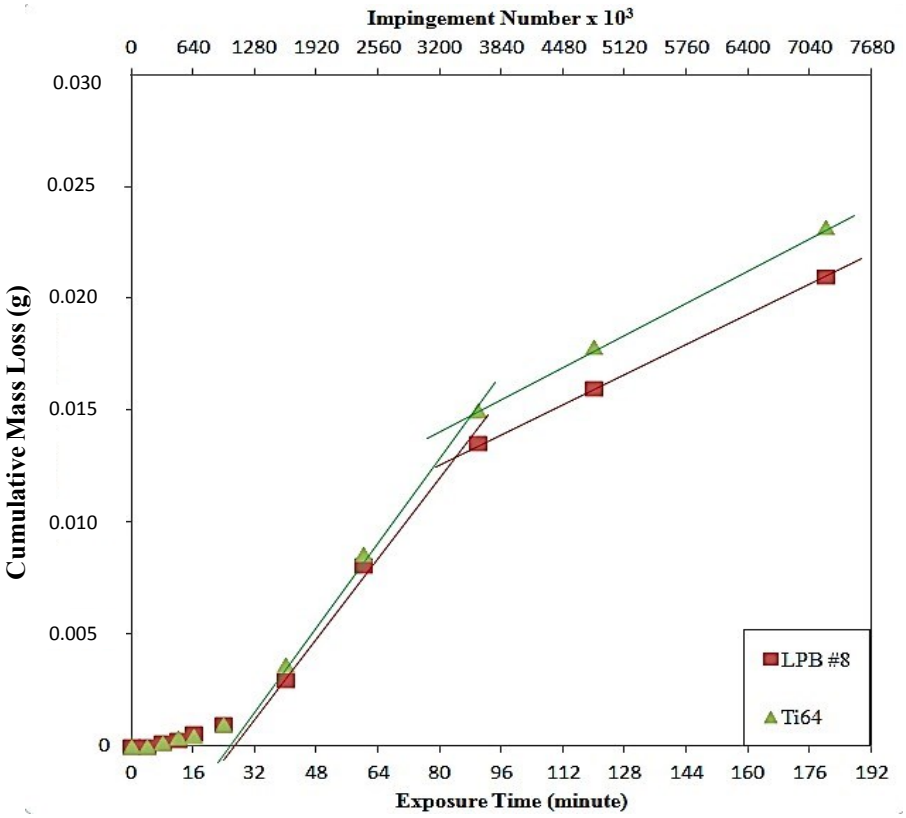

Figure 4-34 Erosion curves of LPB sample #8 with virgin Ti64 with 600µ droplets at 250m/s impact speed.

The incubation period of the LPB sample #8 and the reference Ti64 sample in test 2 (Figure 4-34) are 26 minutes and 25 minutes (as listed in Table 4-13), respectively. There is less variation in the determined incubation periods of the LPB sample #7 and non-treated Ti64 sample as the readings of the mass loss were relatively stable. The maximum erosion rates were calculated to be 0.0002 gram/minute for both curves in test 2 (Figure 4-34). The LIE curves show the same decrease in erosion rates after the end of the third stages as the both curves parallel to each other.

The significant difference between the surface compressive residual stress levels of LPB treated (1100 MPa) and virgin Ti64 (considered as stress free) samples showed no effect on the LIE resistance under the erosion condition of 630μ droplets at 250m/s impact speed.

Table 4-13 Characterizations of the LIE curves

LIE tests with 600μ droplets at 250m/s impact speed	Samples for LIE tests	Incubation period t_0 (minute)	Maximum erosion rate (g/minute)	End Time of the third stage of LIE (minute)
Test #1	LPB #7	24	0.0002	121
	TI64_1	28	0.0002	131
Test #2	LPB #8	26	0.0002	88
	TI64_2	25	0.0002	94

The same observation was performed to the exposed surface during the LIE tests, and the macrographs are shown in Figures 4-35 (test 1) and 4-36 (test 2). Compared to macrographs (Figures 4-24 and 4-25) of the LIE tests at the same impact speed but with smaller droplet size (460 μm), the formed craters in the initial erosion stages were relatively larger. As expected, more severe erosion damage was induced by the larger droplet (630 μm) at the same impact speed of 250 m/s.

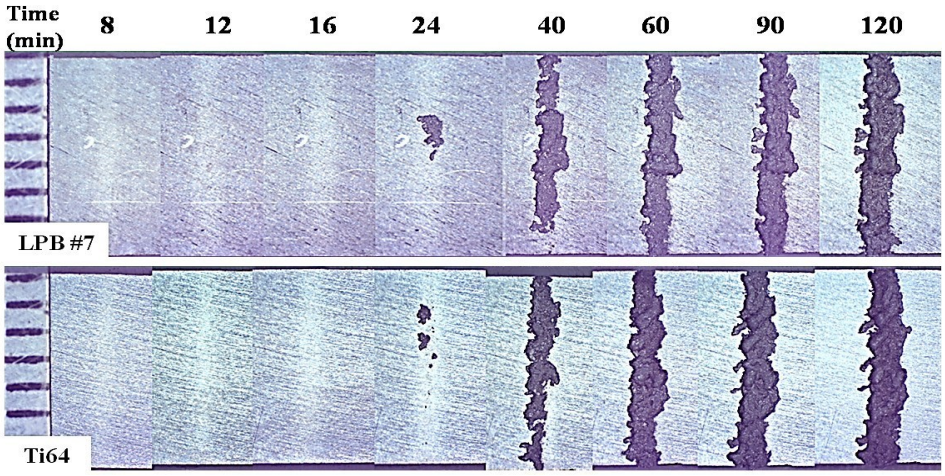

Figure 4-35 Changes in the exposure surface of LPB treated and non-treated Ti64 during the LIE with 630μ droplets at 250m/s impact speed, test 1.

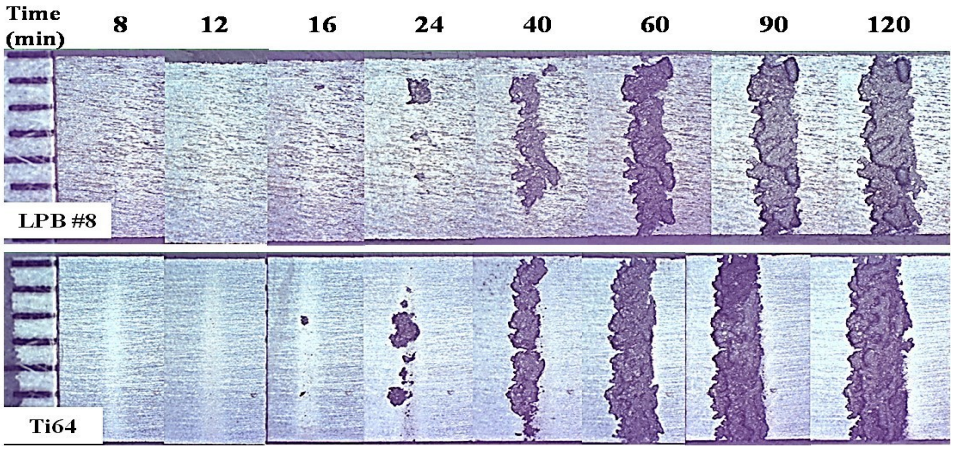

Figure 4-36 Changes in the exposure surface of LPB treated and non-treated Ti64 during the LIE with 600μ droplets at 250m/s impact speed, test 2.

2) 350 m/s impacting speed (14,000 rpm)

Testing condition with 630 μm droplets at the impact speed of 350 m/s is expected to be the worst LIE scenario in this study. The erosion curves plotted in Figures 4-37 and 4-38 indicate that there is no significant difference in the LIE behavior of LPB-treated and virgin Ti64 samples.

Both of the erosion curves of the LPB sample #7 and the reference Ti64 sample in test 1 (Figure 4-37) showed an incubation period of about 1.5 minutes. As the LIE evolves, the two curves reached a maximum erosion rate of 0.0026 grams/min in the third stage

after passing the acceleration stage from 1.5 minutes to 2 minutes, as listed in Table 4-14. The two LIE curves then ended with the same gradually decreased erosion rate till the end of the LIE tests.

A slight difference in the incubation periods were observed in the LIE curves of LPB sample #8 and the reference Ti64 sample used in test 2 (Figure 4-38), which are 1.5 minutes for LPB sample #8 and 1.7 minutes for the non-treated Ti64 sample. The maximum erosion rates are the same (0.0025 gram/min) for the two samples, as listed in Table 4-14. The third stages end after 7 minutes in both LIE curves in test 2 (Figure 4-38) and the erosion rates continue to decrease with a similar erosion rate.

As discussed above, the incubation periods and the maximum erosion rates of all the four curves in both tests are relatively consistent. As a conclusion, the large magnitude of the compressive residual stress induced by LPB on the surface of Ti64 shows little or no effect on the LIE behavior as compared to the virgin Ti64 under this erosion condition.

Table 4-14 Characterizations of the LIE curves

LIE tests with 630 μm droplets at 250m/s impact speed.	Samples for LIE tests	Incubation period t_0 (minute)	Maximum erosion rate (g/minute)	End Time of the third stage of LIE (minute)
Test #1	LPB #7	1.5	0.0026	9
	Ti64_1	1.5	0.0026	9
Test #2	LPB #8	1.5	0.0025	7
	Ti64_2	1.7	0.0025	7

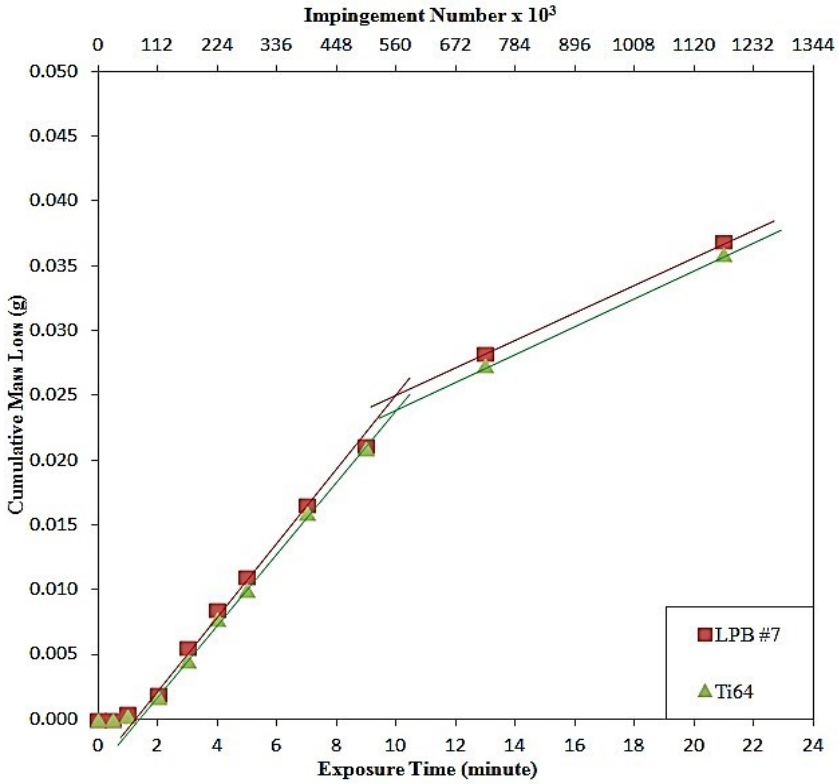

Figure 4-37 Erosion curves of LPB sample #7 with virgin Ti64 with 600µ droplets at 350m/s impact speed.

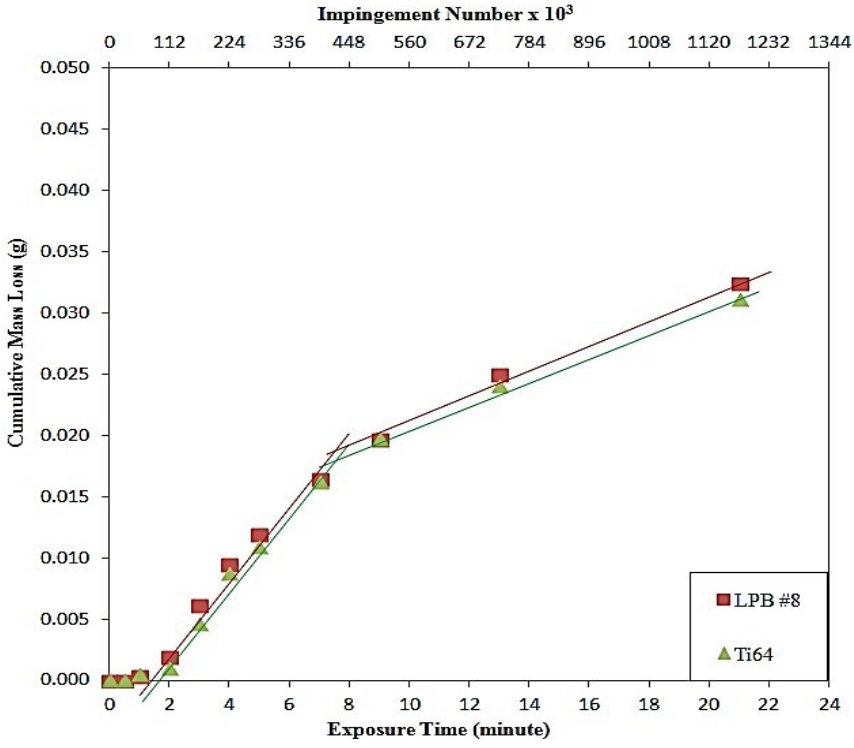

Figure 4-38 Erosion curves of LPB sample #8 with virgin Ti64 with 600µ droplets at 350m/s impact speed.

The changes of the exposed surface was observed at the same time intervals during the LIE tests were as shown in Figures 4-39 (test 1) and 4-40 (test 2). The observation supported that the most severe erosion damage was observed in the LIE condition with 630 μm droplets at the impact speed of 350 m/s at the same erosion period.

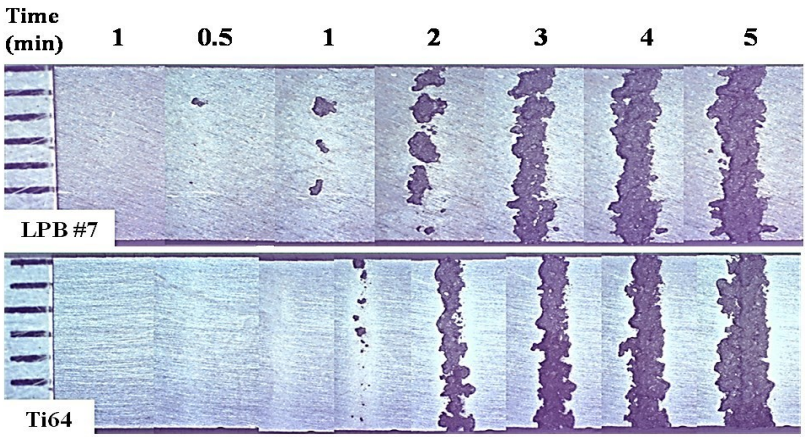

Figure 4-39 Changes in the exposure surface of LPB treated and non-treated Ti64 during the LIE with 630 μm droplets at 350m/s impact speed, test 1.

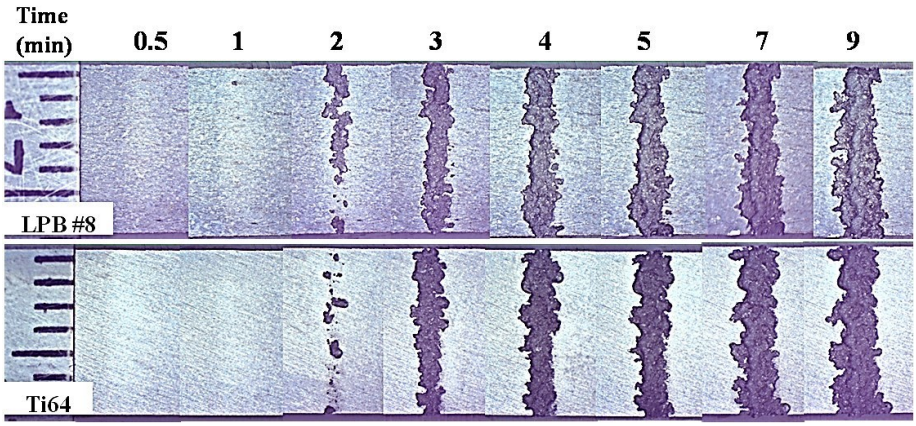

Figure 4-40 Changes in the exposure surface of LPB treated and non-treated Ti64 during the LIE with 630 μm droplets at 350m/s impact speed, test 2.

4.5.3 Discussion for LIE test results

1) The effect of water droplet size on the LIE behavior

Comparisons were made between the LIE results obtained at the same impact speed

for different droplet sizes in the previous sections. As a conclusion, the incubation period in the tests with smaller droplet size (460 μm) at the same impact speed is relatively longer than that of the tests with larger water droplet size (630 μm). And the maximum erosion rate increases with increasing droplet size.

Normalization of the number of the water droplet impingements was made on the LIE curves to investigate the effect of the different water droplet sizes at the same impact speed. Since there is no significant difference between the LIE performance of LPB-treated and non-treated Ti64, the normalization was made on the LIE curves of Ti64, as shown in Figures 4-41 and 4-42. It could be noted that the larger water droplets led to more severe erosion damage on the tested samples at the same number of impingements, this could be explained by the increased kinetic energy generated by the larger water droplets [86].

However, the extent of the effect of the droplet size on the LIE performance varies at the two different speeds. In the case of the tests conducted at 250 m/s impact speed with two different water droplet sizes, the larger droplets (630 μm) led to less severe erosion damage compared to that at higher impact speed (350 m/s), as shown in Figure 4-42. This implies that the effect of the water droplet size on LIE increases with the impact speed.

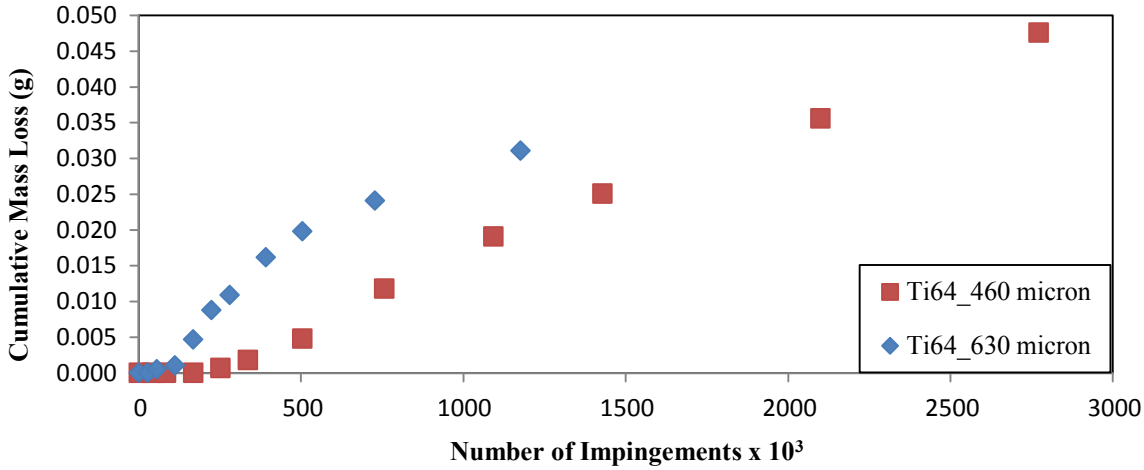

Figure 4-41 Comparison of the LIE tests with different droplet sizes at 350 m/s impact speed

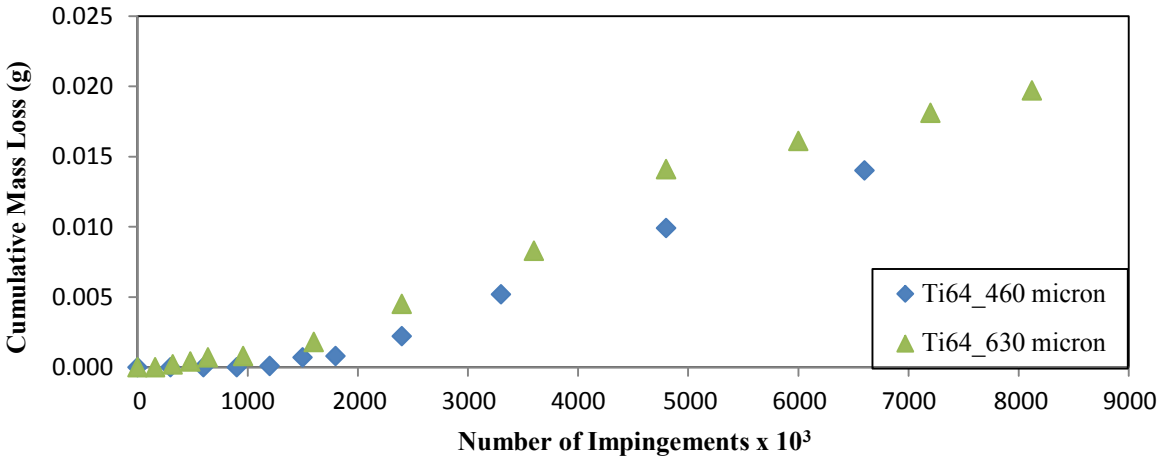

Figure 4-42 Comparison of the LIE tests with different droplet sizes at 250 m/s impact speed

2) The effect of impact speed on the LIE behavior of Ti64

Based on the results discussed in sections 4.5.1 and 4.5.2, LIE induces more severe damage by the same size of the droplets at higher impact speed (350 m/s) than at lower impact speed (250 m/s). Normalization per volume of water was made to investigate the effect of the impact speed. The volume of water impinged on the exposed surface during the LIE tests was calculated based on the impingement number of each droplet size per revolution for each tested sample obtained in Figures 4-22 and 4-23. Accordingly, cumulative mass loss due to the effective volume of water was plotted in Figures 4-43 and 4-44. Significant difference in LIE behavior between the two different impact speeds was observed. It was reported [30, 87] that the water droplet erosion rate is directly proportional to approximately the fifth power of the impact velocity if all other parameters remain constant. Furthermore, the shock pressure *Ps* generated by the impingement of a droplet is expressed as [87]:

$$P_s = \rho C v \qquad (3)$$

where v is the impingement velocity, ρ is the water density and C is the speed of sound in water. C and ρ are physical properties of water and they are constant. Hence, the shock

pressure increases proportionally with increasing impingement velocity, resulting in higher stresses that cause more severe erosion damage to materials.

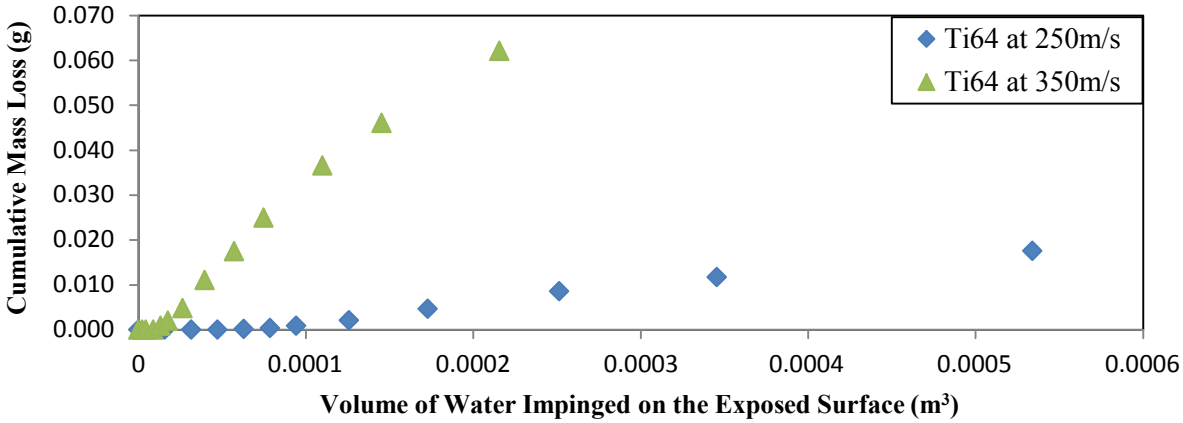

Figure 4-43 Comparison of the LIE tests with different impact speeds with 460 µm droplets

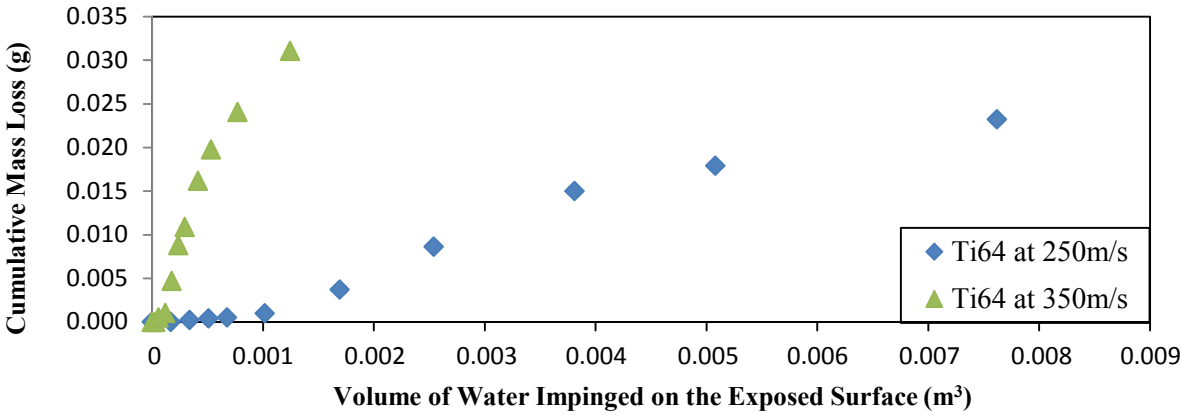

Figure 4-44 Comparison of the LIE tests with different impact speeds with 630 µm droplets

It is noted that the effect of the impact speeds is more pronounced than the effect of the droplet sizes on the LIE behavior of Ti64. And the tests performed at 350 m/s which was over the speed of sound (around 340 m/s) was expected to be more damaged compared to that at 250 m/s. This could be attributed to the increase in the impact energy of the dynamism increased.

3) Effect of LPB on the LIE performance of Ti64

No significant difference between the performance of LPB-treated samples and the non-treated Ti64 samples was observed during the LIE tests. This conclusion could be correlated to the previous studies reporting that the surface treatments such as shot peening, are generally not effective for improving the erosion resistance, since they practically duplicate the process of applying compression that occurs during the incubation period of LIE [23, 37]. In the present study, the "discontinuity" mechanism was used to explain the reason.

Compressive stress pulses induced by LIE are exerted onto the target surface (incident stress wave). This stress wave propagates into the solid substrate until it encounters a structured discontinuity, where part of the stress wave will transmit and part will reflect, as shown schematically in Figure 4-45 (a). As discussed previously that LPB induces high levels of compressive residual stress layer on the surface of Ti64 substrate. Moreover, literature has reported that a nano-crystalline structure of Ti64 was produced after LPB treatment [65, 75]. Both these features of the LPB-treated Ti64 could result in discontinuity #1 for the stress wave propagation during the LIE process. Thus, part of the stress waves transmit through discontinuity #1 and continue propagation until they encounter the discontinuity #2 and reflect again, as shown in Figures 4-45 (b) and (c). Discontinuity #2 could be the other side of the substrate as a geometry discontinuity or another stress wave discontinuity such as boundary between two different phase regions of Ti64. As the LIE process evolves, this phenomenon of transmission and reflection occurs several times, leading to significant tensile stress waves at the location of the discontinuities shown in Figure 4-45 (d), which will lead to the initiation of subsurface

microcracks.

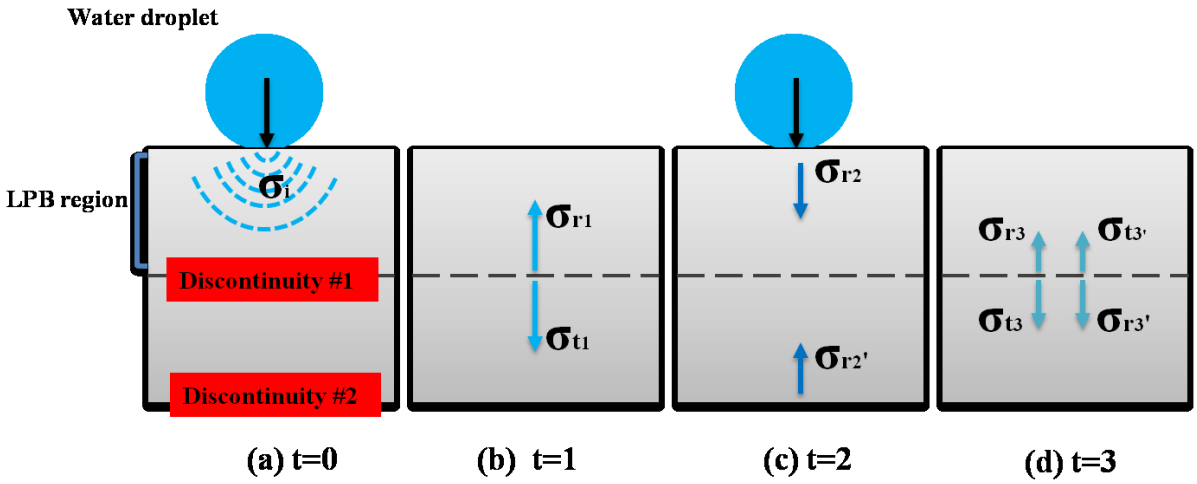

Figure 4-45 Stress wave propagation during LIE (t stands for time).

4.5.4 Material removal mechanism of LIE

The material removal mechanism of LIE is studied in this section with respect to the evolution of the erosion damage. The observed initial and advanced erosion damages of LPB-treated and non-treated Ti64 samples can be related to the stages of the LIE curves discussed in the previous section.

At droplet impact, a shock front is formed in the liquid and a stress wave that propagates in the solid. As a result, the responds of the solid substrate is governed by its dynamic properties. The LIE mechanism described in Figure 2-2 was used to analyze the SEM micrographs for the eroded samples as discussed in the following section.

1) Initial erosion stages of Ti64

The optical macrograph shown in Figure 4-46 illustrates the exposed surface of non-treated Ti64 coupon in the initial stages of LIE; the marked area was shown in details with SEM micrographs as follows in Figures 4-46 to 4-47. The SEM micrographs of the tested Ti64 samples showed similarity with the "surface roughening" erosion mechanisms

mentioned in the stage 1 in Figure 2-2 [12]. Figure 4-46, the untreated Ti64 showed the formation of surface slip bands due to applied water impacts and the slip bands are perpendicular to the shock wave propagation. The folded area, as shown in the enlarged marked area in Figure 4-47, indicates that the surface of virgin Ti64 was experiencing a plastic deformation under the liquid impingements before failing by ductile fracture.

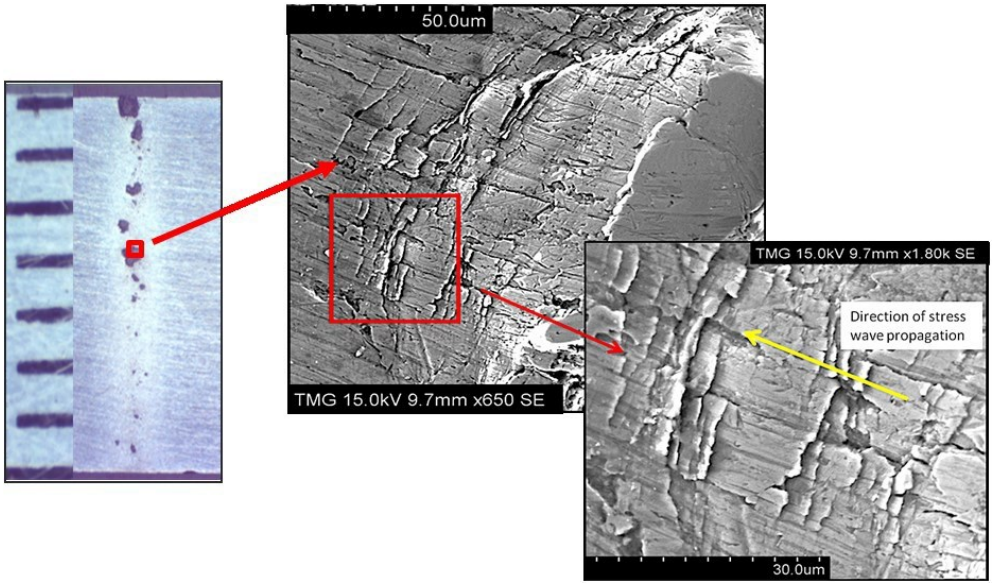

Figure 4-46 Slip bands on non-treated Ti64 surface at the initial LIE stages (marked area)

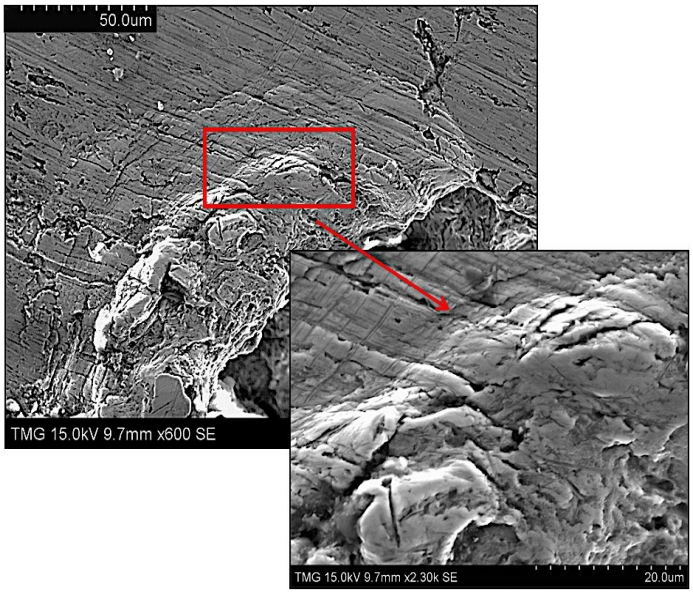

Figure 4-47 Plastic deformation of the non-treated Ti64 surface in initial LIE stages (marked area)

2) Initial erosion stages of LPB treated Ti64

In the case of LPB-treated Ti64, the surface behaved differently relative to the non-treated samples. During the initial stages of LIE, the surface of the LPB treated samples showed a more brittle behavior than the non-treated Ti64 samples. Figure 4-48 shows the slip bands formed on the exposed surface of LPB-treated sample, and their orientation relative to the stress wave propagation direction. Unlike the case of the non-treated Ti64, the eroded surface shows the reduction of ductility due to strain hardening induced by the LPB process. The slips bands formed on the eroded surface of the LPB-treated Ti64 show a more brittle feature as they turn into cracks, as shown in Figure 4-49. This can be attributed to the reduction of the impact damping capacity of the LPB-treated surface.

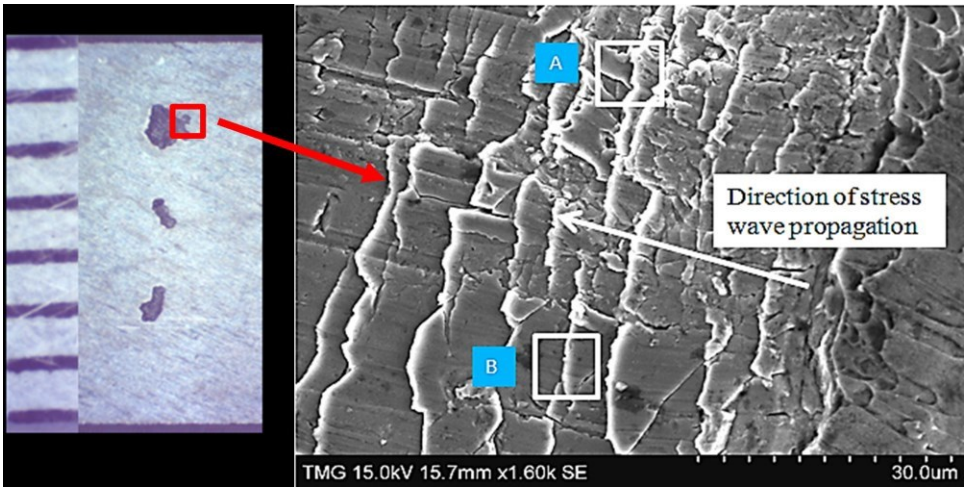

Figure 4-48 Slip bands on the exposed surface of LPB sample in the initial stages of LIE

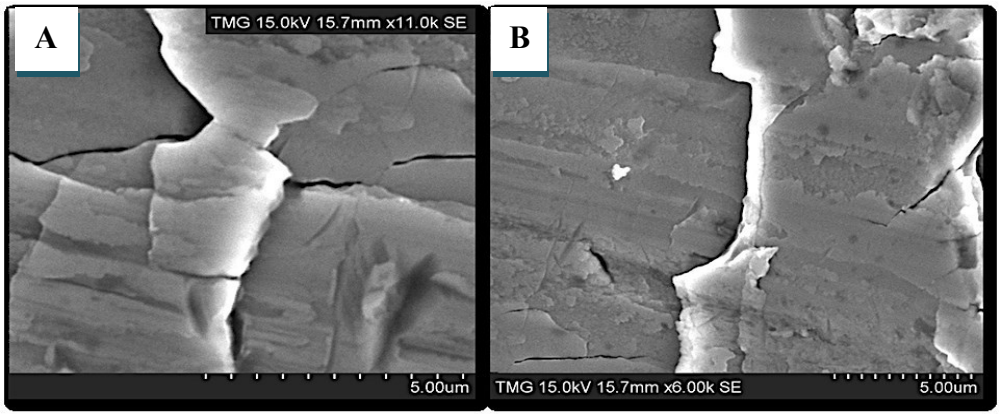

Figure 4-49 Slip bands on the surface of LPB samples

In Figures 4-50 and 4-51, positions marked as A, B and C represent the damage feature sequence as LIE damage proceeds. The extensive crack propagation, observed in area A in Figure 4-50 and Figure 4-51, was not observed in the untreated Ti64 samples and thus shows the reduction in fracture toughness of the treated surface. Moreover, water droplets apply more compression on the specimen's surface as the exposure time increases. As the micro-crack lines merge, they form isolated islands as shown at location B, Figure 4-50. Further erosion causes the detachment of these islands, forming larger pits as shown at location C, Figure 4-50.

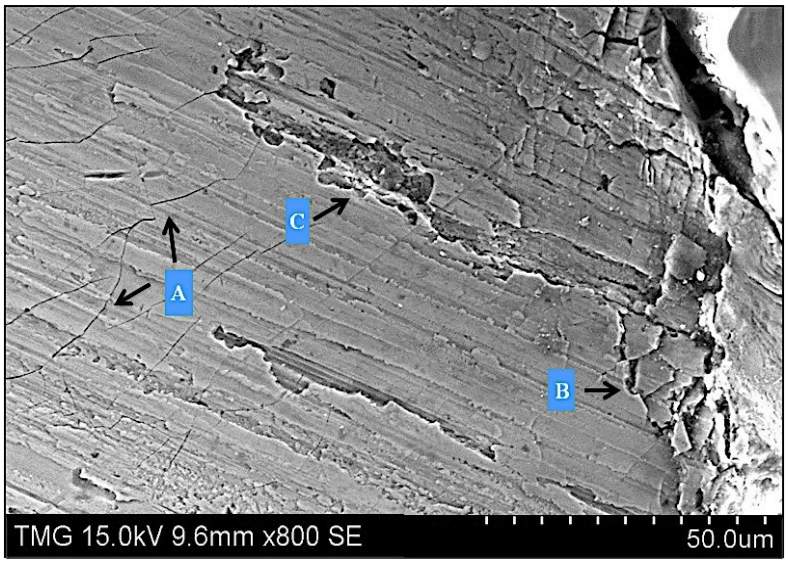

Figure 4-50 Feature of LIE damage on LPB-treated samples

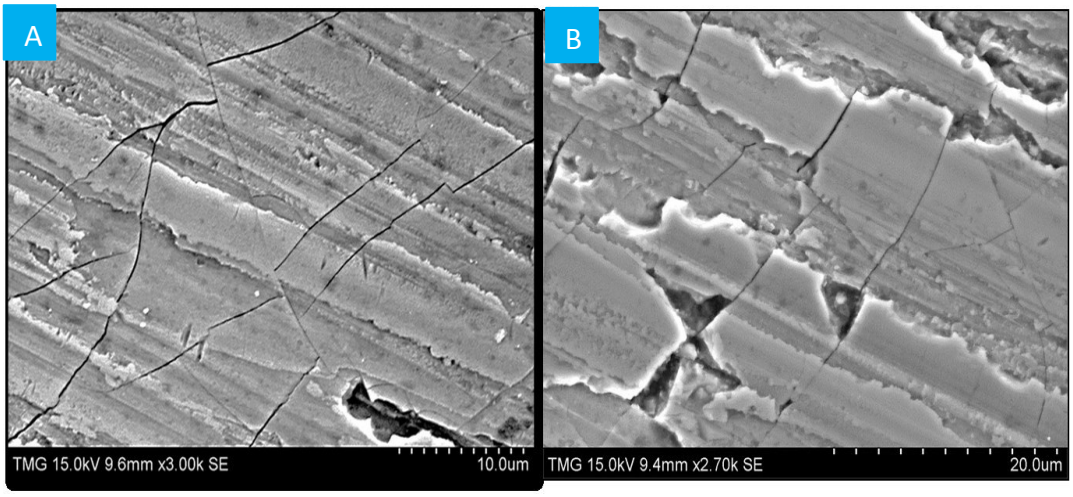

Figure 4-51 Crack formation on LPB treated samples

The features observed above suggest that there are two competing mechanisms at the early stage of the erosion for LPB-treated Ti64, which are the strain hardening and the compressive residual stress. The strain-hardened surface could decrease the erosion resistance due to the induced brittleness. However, the compressive residual stress layer is expecting to be beneficial for arresting the cracks that initiated at earlier stages of the erosion. These two mechanisms balance each other in the case of the LPB-treated Ti64, which results in the same LIE behavior for both LPB-treated and non-treated Ti64.

3) LIE mechanism at advanced stages

It can be seen from the previous SEM micrographs that the initial damage on LPB-treated and the non-treated Ti64 samples under water droplet impingement are distinct from each other. However, later stages of damage for both LPB and non-treated Ti64 samples exhibit very similar fracture modes. The similarity in behavior can be attributed to the detachment of the LPB-treated surface layer during the initial erosion.

One of the failure modes that usually occur in LIE is fatigue damage and it is shown as a set of concentric ridges around the location of the water droplet impact. Luiset et al. [88] reported similar behavior for stainless steel samples under erosion damage. Figure 4-52 shows an example of fatigue crack propagation inside the erosion craters of both non-treated Ti64 and LPB-treated samples.

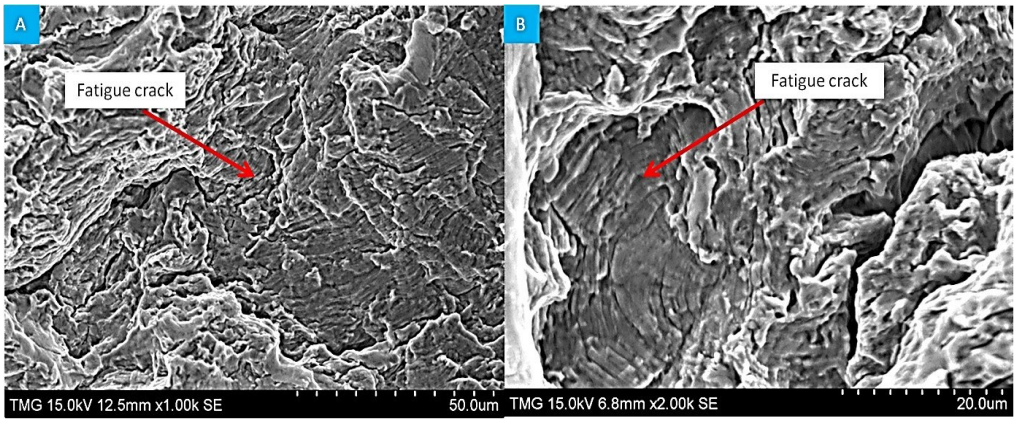

Figure 4-52 Fatigue stress waves on Ti64 non-treated and LPB-treated samples: (A) Ti64; (B) LPB.

Moreover, the propagation of the stress waves through the microstructure is faced with a discontinuity at the interface between α and β phases in the Ti64 microstructure, which causes the formation of microcracks. Similar behavior may imply that the crack propagation moves selectively along a weak path in the structure, which is normally the interface between different phases, in our case α and β phases. These microcracks can be seen in the erosion crater cross section in Figure 4-53, which could be correlated with stages 2 to 4 in Figure 2-2 [12]. Similar behavior was also reported by Huang *et. al* [21] when studying water droplet erosion of Ti64.

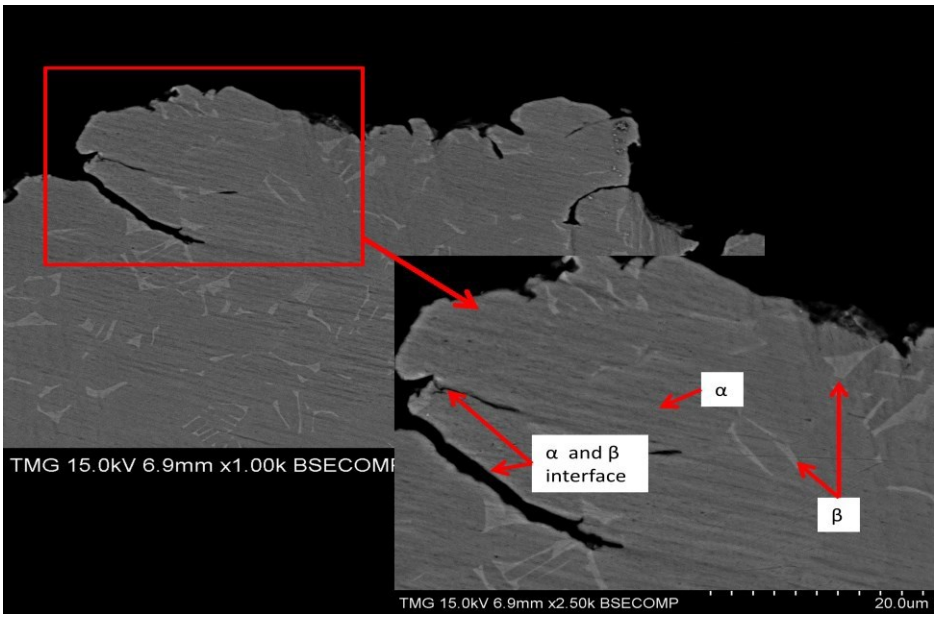

Figure 4-53 Erosion crater of the cross section

As these microcracks merge, large pieces of the material are pulled out and bigger voids are formed. Kong [11] mentioned that if imperfections are present at the grain boundaries the material is more vulnerable to damage under water erosion. Figure 4-54 [11] explains the triple split at the grain boundaries which is the mechanism that explains the erosion damage in Figure 4-55. In part (a) of the illustration in Figure 4-54, it assumes the presence of 4 grains attached at a random orientation, which refers to the feature observed in Figure 4-55 (a). The water droplet impacts produce a hammer pressure, which causes the detachment of grain no. 4 from the other three grains, producing a deep void as shown in part (b) of Figure 4-54, which is similar to the real damage in Figure 4-55 (b).

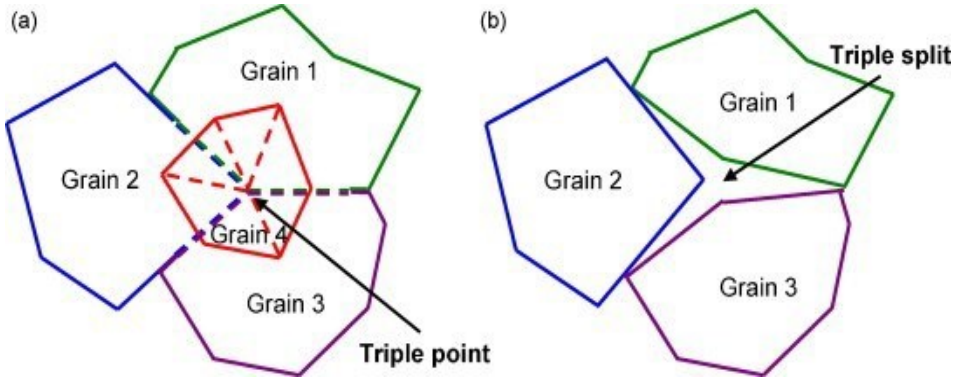

Figure 4-54 Illustration showing the triple split failure [11]

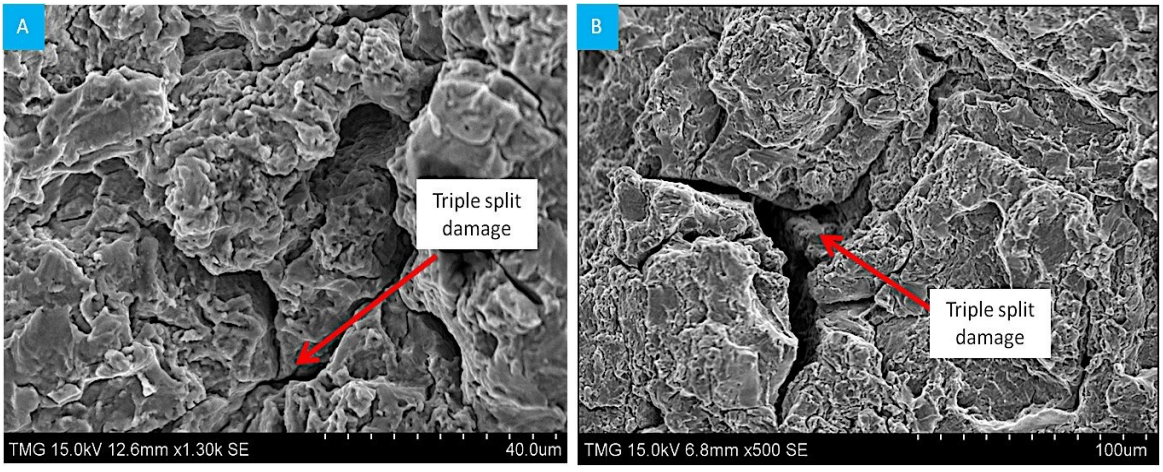

Figure 4-55 Triple split deformation on non-treated Ti64 and LPB treated samples

In addition to the previous failure modes, as the depth of erosion increased in the LPB samples, more ductile regions are encountered, where dimpled surfaces can be seen. This is an indication of ductile fracture as shown in Figure 4-56 for both treated and non-treated Ti64 samples.

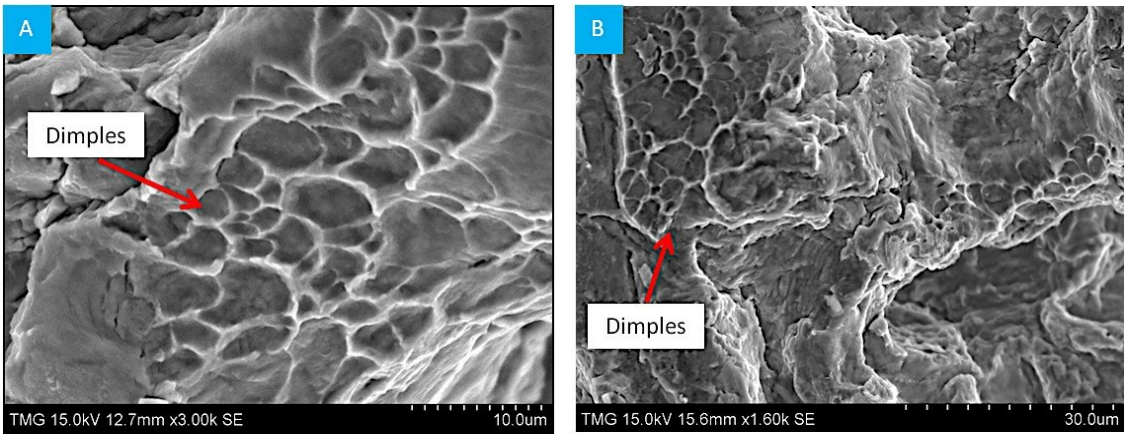

Figure 4-56 Dimples formation in the erosion crater: (A) non-treated Ti64 sample; (B) LPB-treated sample.

Chapter 5

Conclusions, Contributions and Suggestions for the Future Work

5.1 Conclusions

The purpose of this work is to study the effect of low plasticity burnishing on water erosion resistance. In order to achieve this, full factorial experiments were designed to study the effect of burnishing parameters on surface roughness, hardness and maximum value and depth of residual stress. The effect of these parameters on the water erosion behavior of burnished versus as-received Ti64 is discussed. Based on this research, the following conclusion can be drawn.

1. The LPB-treated Ti64 showed little or no improvement in erosion resistance under LIE conditions of 460 μm and 630 μm droplets at 250m/s and 350m/s impact speeds. This could be attributed to the two competing mechanisms of strain hardening and compressive residual stress that balance each other due to the LPB process of Ti64.

2. The present work characterized the first three stages of LIE, which are the incubation, acceleration and the maximum rate. The damage mechanisms in the initial stages of LIE were observed to be in the form of microvoid nucleation, growth and coalescence and slip bands due to stress wave propagation. While in the evolved stages, the microcracks grow along the interface of α and β phases. Moreover, the formation of dimples, fatigue like failure and large material removal were observed.

3. LIE tests with larger droplet size led to more severe erosion damage at constant impact speed due to the increased kinetic energy induced by larger droplets. With the same size of the water droplets, the tested samples show worse performance at higher impact

speed due to higher intensity of stress waves.

4. The feed rate of the LPB process is the only dominant effect on the surface roughness of Ti64. A better surface finish of Ti64 can be obtained using the low level of the burnishing feed rate (0.06 mm/revolution).

5. The surface microhardness of Ti64 is significantly affected by the three-factor interaction effect of the feed rate, number of passes and LPB pressure. In order to obtain an LPB-treated Ti64 surface with improved microhardness, it is preferred to increase two of the factors amongst the feed rate, number of passes and pressure of LPB, and decreasing the third factor simultaneously.

6. The hydraulic pressure of LPB process plays the most important role in both the maximum magnitude and the total depth of the induced compressive residual stress. A Ti64 substrate burnished with high pressure has a larger and deeper layer of compressive residual stress. Moreover, the most intense levels of compression do not occur at the surface but at depths within the range of 80 μm to 160 μm. At depths beyond the compressive peak, stresses are seen to decay, returning to the tensile sub-surface coupon stresses at depths between 300 μm and 660 μm.

7. The nano-crystalline structure and high levels of compressive residual stress induced by LPB process could result in discontinuity for the stress wave propagation in the Ti64 during the LIE process, which leads to the presence of tensile stress waves and subsurface microcracks initiation.

5.2 Contributions and suggestions for the future work

5.2.1 Contributions

LIE performance of LPB-treated Ti64 with different droplets sizes at different impact speeds is investigated for the first time in this work. The associated erosion mechanisms are well described in the present study.

5.2.2 Suggestions for the future work

1. Deign of experiment could be applied to study the effects of the parameters of the water erosion experiment on the LIE performance of the materials.

2. Modeling of LPB process would be beneficial for investigating the effect of the LPB process parameters on the distribution of the compressive residual stress. The process could be optimized by obtaining more detailed information from the LPB modeling results.

3. LIE tests could be performed with more droplet sizes at different impact speeds to acquire more data about the erosion performance of the LPB-treaded Ti64.

4. More studies of the LIE performance of LPB-treated Ti64 could be done on the aerofoil samples since the geometry and dimension is more similar to the edge of the compressor blade. And this could affect the distribution of the compressive residual stresses applied by LPB.

References:

[1] C. B. Meher-Homji and T. R. Mee: Gas Turbine Power Augmentation by Fogging of Inlet Air. *ASME International*, 1999.

[2] Http://www.turbineinletcooling.org/, as on 13th May, 2014.

[3] Http://www.mdscoating.com/technology/index.html, as on 13th May 2014.

[4] Energy Information. Agency: *Database of the U.S. Department of Energy*, 2005.

[5] Http://www.power-technology.com/contractors/powerplantequip/meeindustries/meeindustries3.html, as on 13th May 2014.

[6] M. Ahmad: Experimental Assessment of Droplet Impact Erosion of Low-pressure Steam Turbine Blades. PhD Thesis, University of Stuttgart (Germany) 2009.

[7] J. R. Khan: Fog Cooling, Wet Compression and Droplet Dynamics in Gas Turbine Compressors. PhD Thesis, University of New Orleans (United States) 2009.

[8] F. Heymann: Liquid Impingement Erosion. *ASM Handbook*, vol. 18, 1992.

[9] F. Hammitt and F. Heymann: Liquid-erosion Failures. *ASM Handbook*, pp. 164–171, 1986.

[10] P. V. Rao and D. H. Buckley: Empirical Relations for Cavitation and Liquid Impingement Erosion Processes. *NASA Technical Paper 2339*, 1984.

[11] M. C. Kong, D. Axinte and W. Voice: Aspects of Material Removal Mechanism in Plain Waterjet Milling on Gamma Titanium Aluminide. *Journal of Materials Processing Technology*, Vol. 210, No. 3, pp. 573–584, 2010.

[12] M. Haag: Untersuchungen zur Schädigungsentwicklung an Dampfturbinenwerkstoffen infolge von Wassertropfenerosion. PhD Thesis, Technische Universität Kaiserslautern (Germany) 2012.

[13] W. F. Adler: The Mechanics of Liquid Impact. *Materials Science and Technology*, pp. 132–140, 1979.

[14] K. H. Jolliffe: The Development of Erosion Damage in Metals by Repeated Liquid Droplet Impacts. *Proceedings of the Royal Society of London. Series A: Mathematical and Physical Sciences*, Vol. 303, pp. 193, 1968.

[15] L. Meng, P. Geskin, E.S. Leu, M. C. Li and F. Tismeneskiy: Analytical and Experimental Study of Cleaning with Moving Waterjets. *Journal of Manufacturing Science and Engineering*, Vol. 120, pp. 580–589, 1998.

[16] E. F. Tobin, T. M. Young, D. Raps and O. Rohr: Comparison of Liquid Impingement Results from Whirling Arm and Water-jet Rain Erosion Test Facilities. *Wear*, Vol. 271, No. 9–10, pp. 2625–2631, 2011.

[17] ASTM G73 - 10: Standard Test Method for Liquid Impingement Erosion Using Rotating Apparatus. *ASTM* International, 2010.

[18] B. Lee, K. Riu, S. Shin and S. Kwon: Development of a Water Droplet Erosion Model for Large Steam Turbine Blades. *KSME International Journal*, Vol. 17, No. 1, pp. 114–121, 2003.

[19] S. Hattori: Effects of Impact Velocity and Droplet Size on Liquid Impingement Erosion. *International Symposium on the Ageing Management & Maintenance of Nuclear Power Plants*, pp. 58–7, 2010.

[20] S. Hattori and G. Lin: Effect of Droplet Diameter on Liquid Impingement Erosion. *Proceedings of American Institute of Physics Conference*, Vol. 198, pp. 191–198, 2012.

[21] L. Huang, J. Folkes, P. Kinnell and P. H. Shipway: Mechanisms of Damage

Initiation in a Titanium Alloy Subjected to Water Droplet Impact During Ultra-high Pressure Plain Waterjet Erosion. *Journal of Materials Processing Technology*, vol. 212, No. 9, pp. 1906–1915, 2012.

[22] G. F. Schmitt: Liquid and Solid Particle Impact Erosion. Technical Report AFML-TR-79-4122, 1979.

[23] Y. I. Oka, S. Mihara and H. Miyata: Effective Parameters for Erosion Caused by Water Droplet Impingement and Applications to Surface Treatment Technology. *Wear*, Vol. 263, No. 1–6, pp. 386–394, 2007.

[24] T. Ikohagi and S. Ebara: Advanced Wall Thinning Prediction of Liquid Droplet Impingement Erosion. *International Symposium on the Ageing Management & Maintenance of Nuclear Power Plants,* pp. 47–57, 2010.

[25] C. R. F. Azevedo and A. Sinátora: Erosion-fatigue of Steam Turbine Blades. *Engineering Failure Analysis*, Vol. 16, No. 7, pp. 2290–2303, 2009.

[26] O. G. Engel: Erosion Damage to Solids Caused by High Speed Collision with Rain. *Journal of Research of the National Bureau of Standards*, Vol. 61, No. 1, pp. 47, 1958.

[27] M. Ahmad, M. Casey and N. Sürken: Experimental Assessment of Droplet Impact Erosion Resistance of Steam Turbine Blade Materials, *Wear*, Vol. 267, No. 9–10, pp. 1605–1618, 2009.

[28] T. Wang and T. S. Dhanasekaran: Calibration of CFD Model for Mist/Steam Impinging Jets Cooling. *Prceedings ASME Tubo Expo 2008*, Vol. 4, pp.9-13, 2008.

[29] Z. Ruml and F. Straka: A New Model for Steam Turbine Blade Materials Erosion. *Wear*, Vol. 187, pp. 421–424, 1995.

[30] J. E. Field: ELSI Conference : Invited Lecture Liquid Impact : Theory, Experiment, Applications. *Wear*, pp. 1–12, 1999.

[31] J. Kaspar, J. Bretschneider and S. Jacob: Microstructure, Hardness and Cavitation Erosion Behaviour of Ti6Al4V Laser Nitrided Under Different Gas Atmospheres. *Surface Engineering,* Vol. 23, No. 2, pp. 99–106, 2007.

[32] B. Staniša and V. Ivušić: Erosion Behaviour and Mechanisms for Steam Turbine Rotor Blades. *Wear*, Vol. 187, 1995.

[33] J. Xiong, S. Koshizuka, M. Sakai and H. Ohshima: Investigation on Droplet Impingement Erosion During Steam Generator Tube Failure Accident. *Nuclear Engineering and Design*, Vol. 249, pp. 132–139, 2012.

[34] K. Schiffner and C. D. gen Helling: Simulation of Residual Stresses by Shot Peening. *Computers & Structures*, Vol. 72, pp. 329–340, 1999.

[35] K. Scheel: Effects of Polishing Shot-Peened Surfaces on Fretting Fatigue Behavior of Ti6Al4V. MSc Thesis, Air Force Institute of Technology (United States) 2004.

[36] S. Martinez and S. Sathish: Residual Stress Distribution on Surface-treated Ti6Al4V by X-ray Diffraction. *Experimental Mechanics*, pp. 141–147, 2003.

[37] J. Robinson and R. Reed: Water Droplet Erosion of Laser Surface Treated Ti6Al4V. *Wear*, Vol. 187, pp. 360–367, 1995.

[38] P. Prevéy, N. Jayaraman, and J. Cammett: Overview of Low Plasticity Burnishing for Mitigation of Fatigue Damage Mechanisms. *Fatigue and Fracture of Steels*, pp. 1–6, 2005.

[39] P. Zhang and J. Lindemann: Effect of Roller Burnishing on the High Cycle Fatigue Performance of the High-Strength Wrought Magnesium Alloy AZ80. *Scripta*

Materialia, Vol. 52, no. 10, pp. 1011–1015, 2005.

[40] P. Prevéy: Fatigue Life Extension of Steam Turbine Alloys Using Low Plasticity Burnishing (LPB). *Proceedings of ASME Turbo Expo 2010: Power for Land, Sea and Air*, pp. 13–15, 2010.

[41] N. H. Loh, S. C. Tam and S. Miyazawa: Surface Hardening by Ball Burnishing. *Tribology International*, Vol. 23, No. 6, pp. 413–417, 1990.

[42] M. Salahshoor and Y. B. Guo: Process Mechanics in Ball Burnishing Biomedical Magnesium–calcium Alloy. *The International Journal of Advanced Manufacturing Technology*, Vol. 64, No. 1–4, pp. 133–144, 2012.

[43] Http://www.lambdatechs.com/low-plasticity-burnishing-LPB.html, as on 13th May 2014.

[44] N. S. M. El-Tayeb, K. O. Low and P. V. Brevern: Enhancement of Surface Quality and Tribological Properties Using Ball Burnishing Process Machining Science and Technology, Vol. 12, No. 2, pp. 234–248, 2008.

[45] P. Prevéy and J. Cammett: Low Cost Corrosion Damage Mitigation and Improved Fatigue Performance of Low Plasticity Burnished 7075-T6. *Journal of Materials Engineering and Performance*, Vol. 10, No. 5, pp. 548–555, 2001.

[46] Z. Tang, W. Xia and F. Li: Application of Response Surface Methodology in the Optimization of Burnishing Parameters for Surface Integrity. *The Natural Science Foundation of China*, No. 50975095, pp. 5–8, 2010.

[47] P. Babu, K. Ankamma, P. SIVA, A. Raju and N. Prasad: Optimization of Burnishing Parameters and Determination of Select Surface Characteristics in Engineering Materials. *Indian Academy of Sciences*, Vol. 37, pp. 503–520, 2012.

[48] H. Luo, J. Liu, L. Wang and Q. Zhong: The Effect of Burnishing Parameters on Burnishing Force and Surface Microhardness. *International Journal of Advanced Manufacturing Technology*, Vol. 28, No. 7–8, pp. 707–713, 2005.

[49] F. Gharbi, S. Sghaier, K. J. Al-Fadhalah and T. Benameur: Effect of Ball Burnishing Process on the Surface Quality and Microstructure Properties of AISI 1010 Steel Plates. Journal of Materials Engineering and Performance, Vol. 20, No. 6, pp. 903–910, 2010.

[50] M. Sayahi, S. Sghaier and H. Belhadjsalah: Finite Element Analysis of Ball Burnishing Process: Comparisons Between Numerical Results and Experiments. *International Journal of Advanced Manufacturing Technology*, Vol. 67, No. 5–8, pp. 1665–1673, 2012.

[51] P. Prevéy: Case studies of fatigue life improvement using low plasticity burnishing in gas turbine engine applications. Lambda Technologies, No. 513, 2003.

[52] N. Loh, S. Tam and S. Miyazawa: Statistical Analyses of the Effects of Ball Burnishing Parameters on Surface Hardness. *Wear*, Vol. 129, pp. 235–243, 1989.

[53] J. Scheel, D. Hornbach and N. Jayaraman: Preventing Stress Corrosion Cracking of Nuclear Weldments via Low Plasticity Burnishing. Lambda Technologies, pp. 1–8.

[54] M. Shepard, P. Prevey and N. Jayaraman, –Effects of Surface Treatment on Fretting Fatigue Performance of Ti6Al4V. *International Journal of Fatigue*, 2004.

[55] P. S. Prevéy, R. A. Ravindranath, M. Shepard and T. Gabb: Case Studies of Fatigue Life Improvement Using Low Plasticity Burnishing in Gas Turbine Engine Applications. *Journal of Engineering for Gas Turbines and Power*, Vol. 128, No. 4, pp. 865, 2006.

[56] M. Mhaede and L. Wagner: Effect of Coverage in Ball-Burnishing on Fatigue Performance of Al2024-T4. *Proceedings of the 11th International Conference*, pp. 5–10.

[57] F. Klocke, V. Bäcker and H. Wegner: Influence of Process and Geometry Parameters on the Surface Layer State after Roller Burnishing of IN718. *Production Engneering Research and Development*, 2009.

[58] W. Zhuang and B. Wicks, –Mechanical Surface Treatment Technologies for Gas Turbine Engine Components,‖ J. Eng. Gas Turbines Power, Vol. 125, No. 4, pp. 1021, 2003.

[59] P. Prevéy, D. Hornbach, J. Cammett and R. Ravindranath: Damage Tolerance Improvement of Ti-6-4 Fan Blades with Low Plasticity Burnishing. *Lambda Technologies*, No. 513, 2002.

[60] P. Sartkulvanich, T. Altan F. Jasso, and C. Rodriguez: Finite Element Modeling of Hard Roller Burnishing: An Analysis on the Effects of Process Parameters Upon Surface Finish and Residual Stresses. *Journal of Manufacturing Science and Engineering*, Vol. 129, No. 4, pp. 705, 2007.

[61] D. Hornbach: Residual Stress : Tools For Optimizing Component Performance. *Lambda Technologies*, 2013.

[62] M. S. Mirza, C. M. Sellars, K. Karhausen and P. Evans: Multipass Rolling of Aluminium Alloys: Finite Element Simulations and Microstructural Evolution. *Journal of Materials Science & Technology*, Vol. 17, No. 7, pp. 874–879, 2001.

[63] A. M. Hassan, H. F. Al-Jalil and A. A. Ebied: Burnishing force and Number of Ball Passes for the Optimum Surface Finish of Brass Components. *Journal of Materials*

Science & Technology, Vol. 83, No. 1–3, pp. 176–179, 1998.

[64] W. Zhuang and B. Wicks: Multipass Low-plasticity Burnishing Induced Residual Stresses: Three-Dimensional Elastic-Plastic Finite Element Modeling. *Proceedings of the Institution of Mechanical Engineers, Part C: Journal of Mechanical Engineering Science*, Vol. 218, pp. 663–668, 2004.

[65] R. Nalla, I. Altenberger, U. Noster, G. Liu, B. Scholtes and R. Ritchie: On the Influence of Mechanical Surface treatments—Deep Rolling and Laser Shock Peening—on the Fatigue Behavior of Ti6Al4V at Ambient and Elevated Temperatures. *Materials Science and Engineering A*, Vol. 355, No. 1–2, pp. 216–230, 2003.

[66] P. R. Prabhu, S. M. Kullkarni and S. Sharma: Influence of Deep Cold Rolling and Low Plasticity Burnishing on Surface Hardness and Surface Roughness of AISI 1040 Steel. *World Academy of Science, Engineering and Technology*, 2010.

[67] A. A. Ibrahim: An investigation into ball burnishing process of carbon Steel on a lathe. Mechanical Engineering Department, Shoubra faculty of Engineering, Benha University, pp. 1–13, 2010.

[68] L. N. López de Lacalle, A. Lamikiz, J. A. Sánchez and J. L. Arana: The Effect of Ball Burnishing on Heat-treated Steel and Inconel 718 Milled Surfaces. *International Journal of Advanced Manufacturing Technology*, Vol. 32, pp. 958–968, 2007.

[69] K. O. Low and K. J. Wong: Influence of Ball Burnishing on Surface Quality and Tribological Characteristics of Polymers under Dry Sliding Conditions. *Tribology International*, Vol. 44, pp. 144–153, 2011.

[70] P. S. Dabeer and G. K. Purohit: Effect of Ball Burnishing Parameters on Surface Roughness Using Surface Roughness Methodology. *Advances in Production Engineering & Management*, Vol. 5, pp. 111–116, 2010.

[71] C. Y. Seemikeri, P. K. Brahmankar and S. B. Mahagaonkar: Investigations on Surface Integrity of AISI 1045 Using LPB Tool. *Tribology International*, 2008.

[72] N. Jayaraman, P. S. Prevéy and M. W. Mahoney: Fatigue Life Improvement of an Aluminum Alloy FSW with Low Plasticity Burnishing. *TMS Annual Meeting*, 2003.

[73] I. Altenberger, E. a. Stach, G. Liu, R. K. Nalla and R. O. Ritchie: An In Situ Transmission Electron Microscope Study of the Thermal Stability of Near-surface Microstructures Induced by Deep Rolling and Laser-shock Peening. *Scripta Materialia*, Vol. 48, No. 12, pp. 1593–1598, 2003.

[74] I. Altenberger, R. K. Nalla, Y. Sano, L. Wagner and R. O. Ritchie: On the Effect of Deep-rolling and Laser-Peening on the Stress-controlled Low- and High-cycle Fatigue Behavior of Ti6Al4V at Elevated Temperatures up to 550°C. *International Journal of Fatigue*, Vol. 44, pp. 292–302, 2012.

[75] E. Maawad, H.-G. Brokmeier, L. Wagner, Y. Sano and C. Genzel: Investigation on the Surface and Near-Surface Characteristics of Ti–2.5Cu after Various Mechanical Surface Treatments. *Surface and Coatings Technology*, Vol. 205, No. 12, pp. 3644–3650, 2011.

[76] I. Altenberger, R. Nalla and U. Noster: Fatigue Behavior and Associated Effect of Residual Stresses in Deep-Rolled and Laser Shock Peened Ti-6Al-4V Alloys at Ambient and Elevated Temperatures. *International Journal of Fatigue*, 2002.

[77] Http://www.aerospacemetals.com/titanium-ti-6al-4v-ams-4911.html, as on 13th

May 2014.

[78] M. Wenzelburger, D. López and R. Gadow: Methods and application of residual stress analysis on thermally sprayed coatings and layer composites. *Surface and Coatings Technology*, Vol. 201, pp. 1995–2001, 2006.

[79] Http://www.npl.co.uk/science-technology/engineered-materials/services/residual-stress-and-strain-measurement, as on 13th May 2014.

[80] Http://www.veqter.co.uk/residual-stress-measurement/centre-hole-drilling, as on 13th May 2014.

[81] Http://www.stresscraft.co.uk/index.htm, as on 13th May 2014.

[82] D. Montgomery: *Design and Analysis of Experiments*, John Wiley and Sons, New York, 1997, pp. 233-249.

[83] G. Box, J. Hunter and W. Hunter: *Statistics for Experimenters*, John Wiley and Sons, New York, 2005, pp. 173-181.

[84] P. V. Grant, J. D. Lord and P. S. Whitehead, ―The measurement of Residual Stresses by the Incremental Hole Drilling Technique,‖ *National Physical Laboratory Good Practice Guide*, Vol. 53, No. 2, 2006.

[85] ASTM G73 - 10: Standard Test Method for Liquid Impingement Erosion Using Rotating Apparatus. *ASTM International*, Vol. 03.02, 2010.

[86] M. Ahmad, M. Schatz and M. V. Casey: Experimental Investigation of Droplet Size Influence on Low Pressure Steam Turbine Blade Erosion. *Wear*, Vol. 303, No. 1–2, pp. 83–86, 2013.

[87] J. Field, M. Lesser and J. Dear: Studies of Two-dimensional Liquid-wedge Impact and their Relevance to Liquid-drop Impact Problems. *Proceedings of the Royal*

Society of London. Series A: Mathematical and physical sciences, Vol. 401, No. 1821, pp. 225–249, 1985.

[88] B. Luiset, F. Sanchette, A. Billard and D. Schuster: Mechanisms of Stainless Steels Erosion by Water Droplets. *Wear*,Vol. 303, No. 1–2, pp. 459–464, 2013.

Appendix A

This incremental hole drilling method was carried out to determine the distributions of residual stresses in sixteen LPB-treated Ti64 coupons. Results from individual gauges are shown in Appendix B Figures B-1 to B-16.

One CEA-06-062UL-120 target gauge was installed on the surface of each coupon with elements 1 and 3 aligned (indicated by the arrow marking) as shown at the bottom part of each page in Appendix B. These directions also refer to stresses σ1 and σ3 in the subsequent results sheets.

Each coupon in turn was cemented to an angle plate. Gauges were drilled using a miniature PC controlled orbital drilling machine. The orbital hole drilling procedure was carried at 16 drill depth increments, recording the relaxed strains at each increment. Hole drilling depth increments were set at 4 x 32 μm + 4 x 64 μm + 8 x 128 μm, giving a completed hole depth of 1408 μm. Residual stresses were calculated from relaxed strains using the Integral Method developed to evaluate stresses, which vary with depth.

Appendix B

Gauge Type = 062UL Hole diameter = 1.94 mm **Gauge No. #1**

depth	Relaxed Strains (με)					
	measured			smoothed		
μm	ε1	ε2	ε3	ε1	ε2	ε3
32	10	6	7	15	11	12
64	39	31	32	41	34	34
96	75	66	64	76	67	66
128	116	106	105	116	106	105
192	196	184	186	193	180	182
256	262	247	250	255	241	244
320	301	284	288	298	281	285
384	328	310	314	326	308	313
512	367	349	354	364	346	351
640	393	374	380	391	372	378
768	409	391	396	407	389	395
896	418	399	406	417	398	405
1024	422	404	412	422	404	411
1152	426	408	415	425	408	415
1280	427	410	417	427	410	417
1408	428	412	419			

[Stresscraft RS INT v5.6] *PSW* MAY05

depth	Residual Stresses (MPa)				
	principal		direct		shear
μm	σmax	σmin	σ1	σ3	τ13
16	-267	-358	-338	-287	-38
48	-461	-526	-521	-466	-18
80	-610	-648	-648	-610	1
112	-653	-662	-658	-656	-4
160	-541	-567	-549	-560	-12
224	-347	-362	-354	-356	-8
288	-141	-151	-148	-144	-4
352	-24	-27	-25	-27	1
448	7	0	7	1	2
512	5	-1	5	0	2
640	3	-2	2	-1	2
768	23	18	22	18	1
896	32	27	32	27	1
1024	42	37	42	37	1

direction 1
direction 3

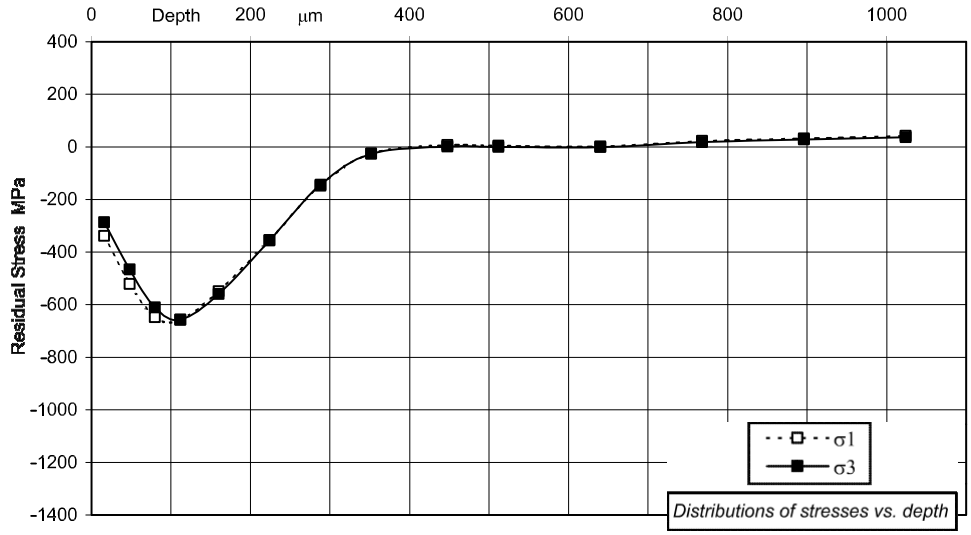

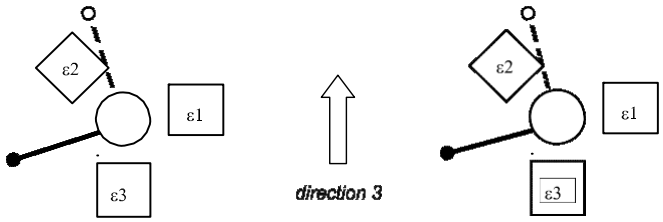

Stress directions at depth 512 μm *Stress directions at depth 1024 μm*

Young's Modulus = 115.0 GPa Poisson's ratio = 0.320 **Gauge No. #1**

Figure B-1 Residual stress measurement of LPB sample #1

Gauge Type = 062UL Hole diameter = 1.93 mm ***Gauge No. #2***

depth	Relaxed Strains (με)					
	measured			smoothed		
μm	ε1	ε2	ε3	ε1	ε2	ε3
32	11	8	11	17	13	15
64	45	34	36	48	37	38
96	89	70	70	90	71	72
128	135	109	111	135	109	112
192	226	189	199	224	186	195
256	309	255	272	300	248	265
320	356	294	316	352	291	312
384	386	319	342	384	317	340
512	428	356	377	422	352	374
640	447	378	398	446	376	396
768	461	391	410	460	390	409
896	469	401	417	468	400	416
1024	473	406	421	473	406	421
1152	476	410	425	476	410	425
1280	477	412	427	477	412	427
1408	477	414	428			

[Stresscraft RS INT v5.6] *PSW* MAY05

depth	Residual Stresses (MPa)				
	principal		direct		shear
μm	εmax	εmin	ε1	ε3	ε13
16	-325	-433	-397	-361	-51
48	-493	-637	-619	-511	-47
80	-631	-784	-768	-647	-47
112	-665	-786	-756	-695	-52
160	-578	-694	-644	-628	-57
224	-387	-483	-445	-425	-47
288	-158	-208	-189	-176	-24
352	-7	-13	-12	-9	3
448	58	29	44	43	15
512	57	28	44	40	14
640	55	27	45	38	13
768	59	35	51	44	11
896	61	39	53	47	11
1024	63	43	56	50	10

direction 1
direction 3

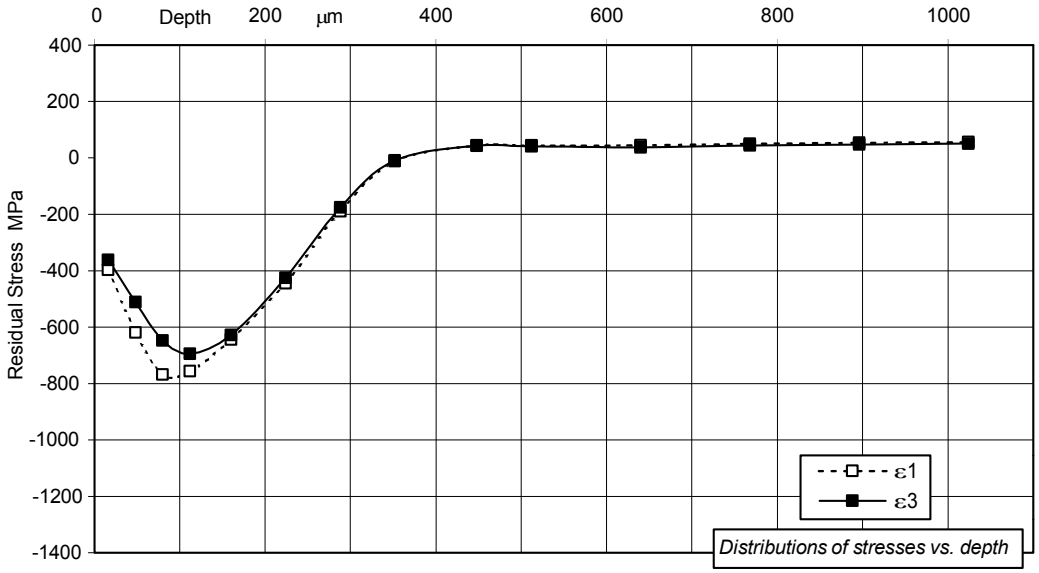

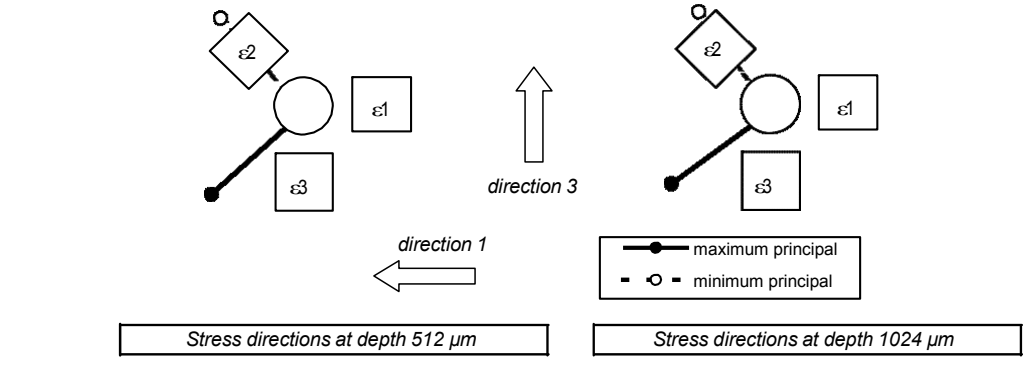

Young's Modulus = 115.0 GPa Poisson's ratio = 0.320 ***Gauge No. #2***

Figure B-2 Residual stress measurement of LPB sample #2

Gauge Type = 062UL Hole diameter = 1.95 mm ***Gauge No. #3***

depth	Relaxed Strains (με)					
	measured			smoothed		
μm	ε1	ε2	ε3	ε1	ε2	ε3
32	18	14	11	22	18	15
64	53	44	37	56	48	40
96	98	88	76	99	89	77
128	145	135	120	145	136	121
192	241	234	215	238	229	211
256	325	313	292	318	305	285
320	380	361	341	375	357	337
384	415	394	374	412	392	371
512	463	441	419	459	437	415
640	494	470	447	491	467	445
768	512	488	465	511	487	464
896	525	500	477	524	499	476
1024	534	508	486	533	507	485
1152	538	513	491	538	513	491
1280	543	517	495	542	517	494
1408	545	520	497			

[Stresscraft RS INT v5.6] *PSW* MAY05

depth	Residual Stresses (MPa)				
	principal		direct		shear
μm	εmax	εmin	ε1	ε3	ε13
16	-375	-495	-494	-376	-8
48	-530	-641	-641	-530	3
80	-680	-763	-758	-685	19
112	-714	-767	-752	-729	24
160	-636	-661	-648	-650	12
224	-434	-458	-453	-440	-10
288	-188	-236	-222	-201	-22
352	-37	-55	-46	-46	-9
448	20	14	20	14	2
512	17	12	16	12	1
640	13	10	13	10	0
768	17	13	17	14	-1
896	19	15	19	15	-1
1024	21	17	21	17	-1

direction 1
direction 3

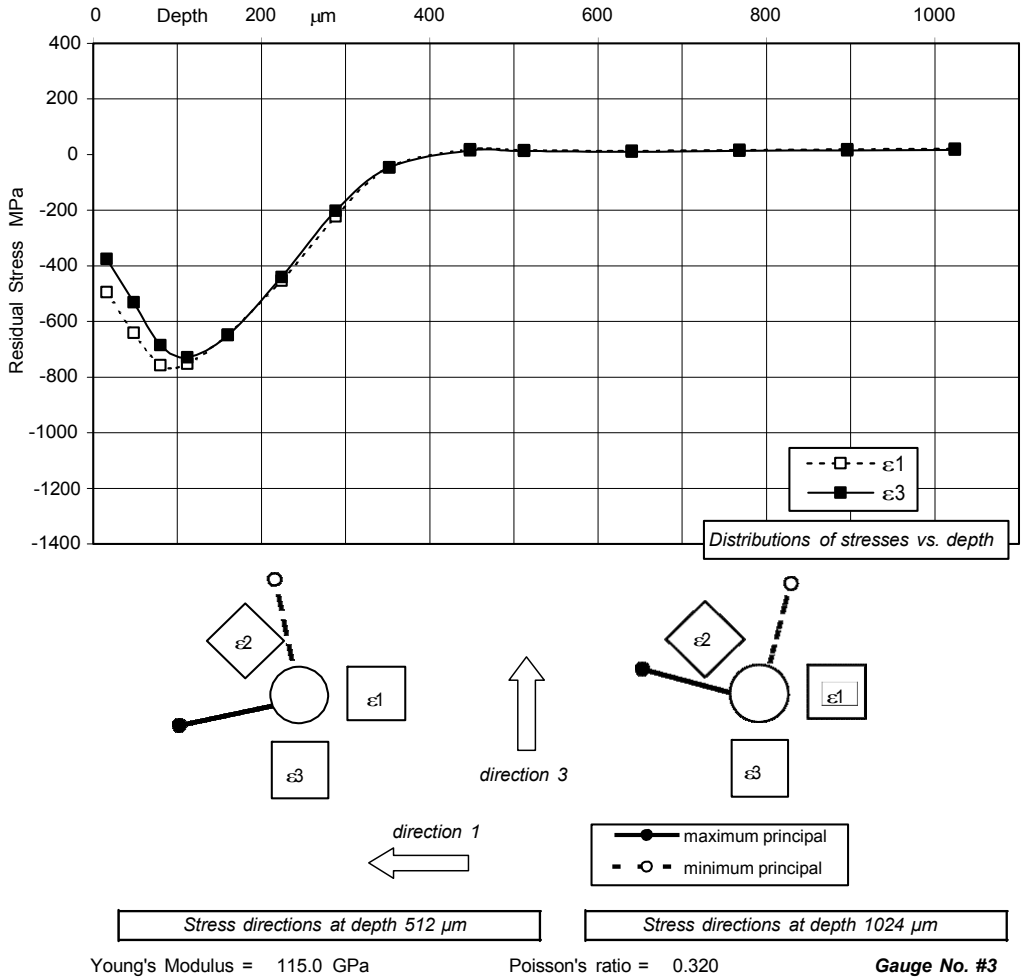

Young's Modulus = 115.0 GPa Poisson's ratio = 0.320 ***Gauge No. #3***

Figure B-3 Residual stress measurement of LPB sample #3

Gauge Type = 062UL Hole diameter = 1.97 mm ***Gauge No. #4***

depth	Relaxed Strains (με)					
	measured			smoothed		
μm	ε1	ε2	ε3	ε1	ε2	ε3
32	24	14	15	30	19	19
64	70	48	46	72	51	48
96	124	93	86	125	94	88
128	181	142	132	180	142	133
192	287	240	230	283	236	225
256	375	323	309	367	315	301
320	430	373	355	424	368	351
384	461	402	384	458	400	381
512	502	440	421	498	437	417
640	526	465	443	524	462	441
768	540	479	456	539	478	455
896	548	487	465	548	487	464
1024	554	493	470	553	492	470
1152	556	496	474	556	496	474
1280	558	498	477	558	498	476
1408	560	500	478			

[Stresscraft RS INT v5.6] *PSW* MAY05

depth	Residual Stresses (MPa)				
	principal		direct		shear
μm	εmax	εmin	ε1	ε3	ε13
16	-444	-675	-641	-478	-82
48	-587	-806	-791	-603	-56
80	-711	-894	-889	-716	-30
112	-736	-848	-845	-740	-20
160	-646	-674	-671	-649	-8
224	-422	-437	-435	-425	5
288	-159	-176	-174	-161	5
352	18	4	17	5	4
448	76	58	75	59	5
512	67	49	64	52	6
640	58	41	54	44	7
768	58	45	57	47	4
896	58	47	58	48	2
1024	59	49	59	49	1

direction 1
direction 3

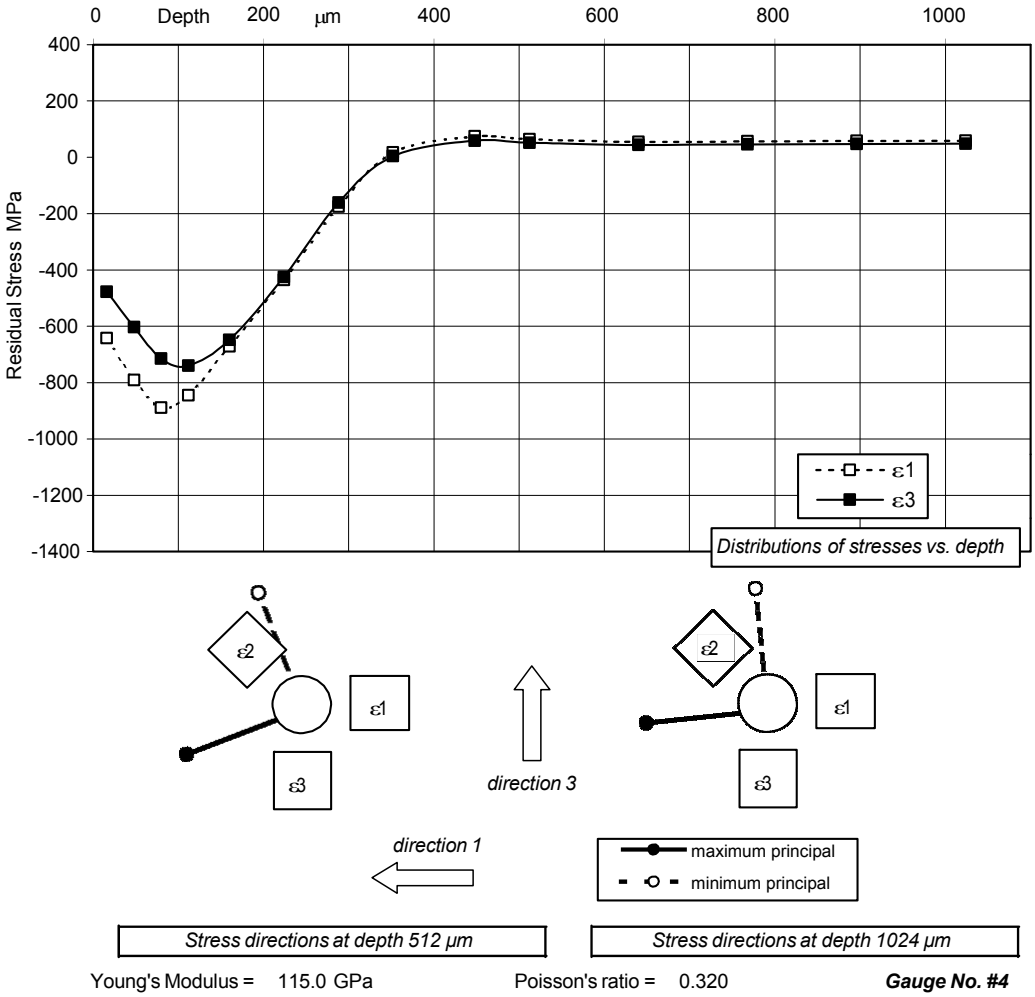

Young's Modulus = 115.0 GPa Poisson's ratio = 0.320 ***Gauge No. #4***

Figure B-4 Residual stress measurement of LPB sample #4

Gauge Type = 062UL Hole diameter = 1.92 mm ***Gauge No. #5***

depth	Relaxed Strains (με)					
	measured			smoothed		
μm	ε1	ε2	ε3	ε1	ε2	ε3
32	22	10	10	28	16	14
64	67	42	35	70	45	36
96	122	85	65	125	87	67
128	190	135	103	189	136	106
192	317	242	199	315	244	204
256	434	356	315	430	354	314
320	535	460	426	532	456	421
384	625	549	516	618	541	508
512	751	666	628	734	650	612
640	808	720	677	801	714	672
768	838	751	706	835	748	703
896	856	769	723	854	768	722
1024	865	784	734	864	783	733
1152	871	793	742	871	792	742
1280	876	799	748	875	798	747
1408	879	803	752			

[Stresscraft RS INT v5.6] *PSW* MAY05

depth	Residual Stresses (MPa)				
	principal		direct		shear
μm	εmax	εmin	ε1	ε3	ε13
16	-367	-653	-624	-395	-86
48	-517	-817	-811	-522	-39
80	-635	-987	-986	-635	-10
112	-720	-1041	-1040	-721	-19
160	-802	-918	-914	-806	-19
224	-743	-803	-744	-802	-7
288	-601	-709	-601	-709	-3
352	-427	-482	-427	-482	2
448	-177	-190	-189	-178	3
512	-83	-94	-90	-87	6
640	15	-2	8	4	8
768	61	36	54	42	11
896	84	54	77	61	13
1024	108	73	100	80	14

direction 1
direction 3

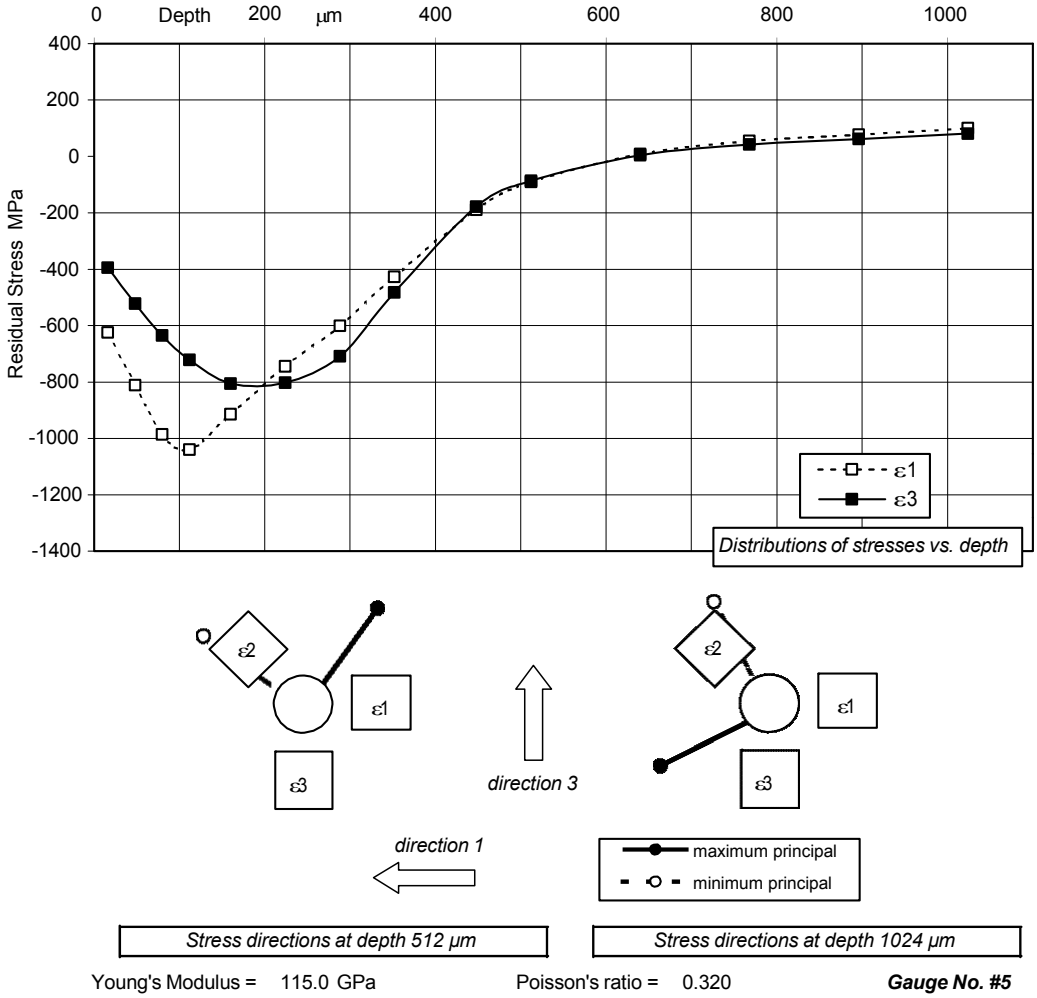

Young's Modulus = 115.0 GPa Poisson's ratio = 0.320 ***Gauge No. #5***

Figure B-5 Residual stress measurement of LPB sample #5

Gauge Type = 062UL Hole diameter = 1.94 mm **Gauge No. #6**

depth	Relaxed Strains (με)					
	measured			smoothed		
μm	ε1	ε2	ε3	ε1	ε2	ε3
32	27	10	13	33	16	18
64	78	43	45	80	46	47
96	137	89	86	138	91	89
128	199	141	140	200	143	142
192	328	259	266	323	257	265
256	438	370	387	434	366	382
320	531	466	487	529	462	480
384	614	544	559	607	537	551
512	720	644	642	706	631	632
640	769	693	683	765	689	679
768	801	724	709	799	721	707
896	823	744	727	820	743	726
1024	834	758	739	834	757	738
1152	843	767	748	842	766	747
1280	848	773	752	847	772	752
1408	851	776	756			

[Stresscraft RS INT v5.6] *PSW* MAY05

depth	Residual Stresses (MPa)				
	principal		direct		shear
μm	εmax	εmin	ε1	ε3	ε13
16	-411	-805	-730	-486	-154
48	-605	-940	-900	-645	-109
80	-785	-1026	-1007	-805	-66
112	-890	-1022	-995	-916	-53
160	-867	-948	-883	-932	-33
224	-674	-766	-674	-766	-1
288	-495	-546	-500	-541	15
352	-275	-338	-322	-290	27
448	-34	-111	-98	-47	28
512	2	-52	-41	-9	22
640	40	5	16	29	16
768	45	24	33	36	11
896	49	32	41	39	8
1024	53	39	50	42	6

direction 1
direction 3

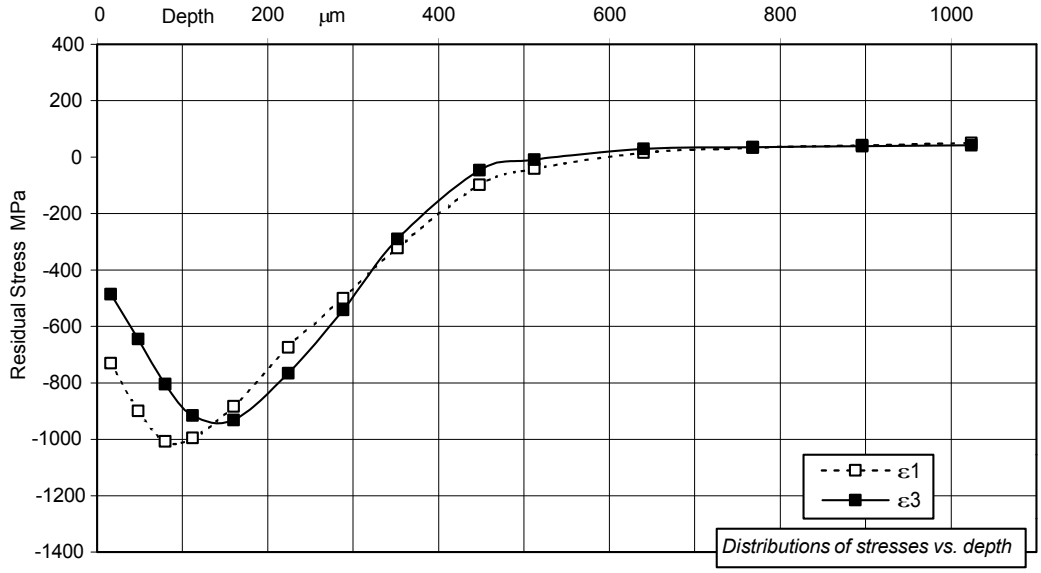

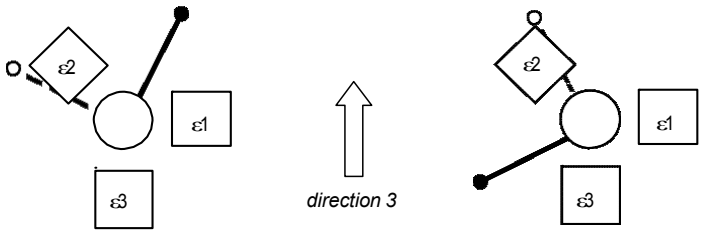

direction 1

maximum principal
minimum principal

Stress directions at depth 512 μm

Stress directions at depth 1024 μm

Young's Modulus = 115.0 GPa Poisson's ratio = 0.320 **Gauge No. #6**

Figure B-6 Residual stress measurement of LPB sample #6

Gauge Type = 062UL Hole diameter = 1.92 mm **Gauge No. #7**

depth	Relaxed Strains (με)					
	measured			smoothed		
μm	ε1	ε2	ε3	ε1	ε2	ε3
32	42	25	21	47	29	23
64	103	65	50	105	67	52
96	171	113	87	173	115	89
128	245	167	133	244	168	135
192	385	284	241	380	283	241
256	506	396	350	502	392	347
320	612	492	448	608	489	443
384	701	574	527	693	567	519
512	813	678	622	799	665	610
640	870	730	669	865	726	665
768	906	765	700	902	762	697
896	927	786	720	926	785	719
1024	943	802	734	941	801	733
1152	951	812	742	950	811	741
1280	956	818	747	956	817	747
1408	960	822	751			

[Stresscraft RS INT v5.6] *PSW* MAY05

depth	Residual Stresses (MPa)				
	principal		direct		shear
μm	εmax	εmin	ε1	ε3	ε13
16	-638	-1075	-1051	-663	-100
48	-650	-1109	-1096	-663	-76
80	-731	-1164	-1154	-741	-64
112	-807	-1129	-1118	-818	-58
160	-824	-941	-934	-830	-26
224	-714	-734	-719	-730	-8
288	-550	-582	-554	-578	-11
352	-351	-369	-351	-369	3
448	-91	-120	-104	-108	15
512	-38	-64	-48	-55	12
640	15	-8	8	-2	10
768	38	15	33	20	10
896	50	26	45	31	10
1024	62	38	57	43	9

direction 1
direction 3

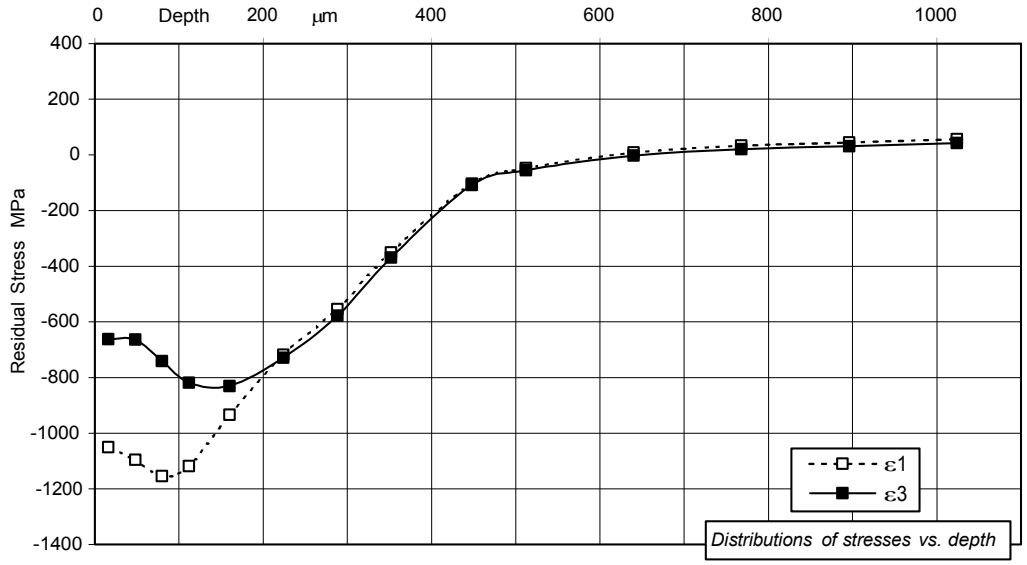

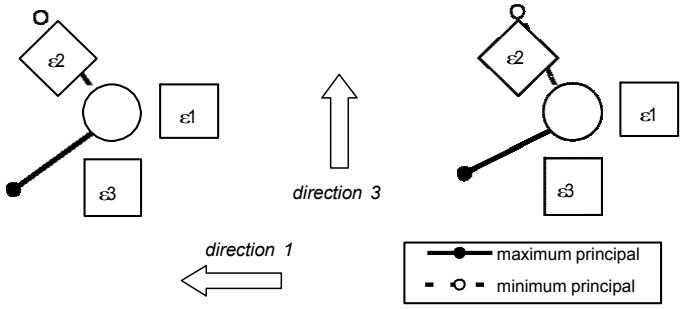

Stress directions at depth 512 μm *Stress directions at depth 1024 μm*

Young's Modulus = 115.0 GPa Poisson's ratio = 0.320 **Gauge No. #7**

Figure B-7 Residual stress measurement of LPB sample #7

Gauge Type = 062UL Hole diameter = 1.91 mm ***Gauge No. #8***

depth	Relaxed Strains (με)					
	measured			smoothed		
μm	ε1	ε2	ε3	ε1	ε2	ε3
32	42	23	15	46	27	19
64	99	63	44	99	64	45
96	157	107	77	158	108	79
128	217	153	116	217	154	118
192	336	253	208	330	253	210
256	431	351	308	429	349	306
320	519	441	399	517	438	394
384	597	517	471	591	510	465
512	706	616	563	691	604	551
640	756	665	608	753	661	604
768	792	698	638	788	695	635
896	812	718	656	811	716	655
1024	826	730	668	824	729	667
1152	833	737	674	832	736	674
1280	836	741	679	837	741	678
1408	841	744	681			

[Stresscraft RS INT v5.6] *PSW* MAY05

depth	Residual Stresses (MPa)				
	principal		direct		shear
μm	εmax	εmin	ε1	ε3	ε13
16	-556	-1032	-1018	-570	-80
48	-609	-1018	-1013	-615	-46
80	-659	-987	-985	-662	-27
112	-688	-917	-912	-692	-32
160	-711	-772	-767	-717	-17
224	-579	-660	-580	-659	8
288	-463	-543	-466	-540	15
352	-330	-362	-335	-357	11
448	-129	-141	-140	-129	3
512	-70	-79	-76	-73	4
640	-9	-20	-12	-16	5
768	23	15	22	16	3
896	39	32	39	32	2
1024	56	49	56	49	1

direction 1
direction 3

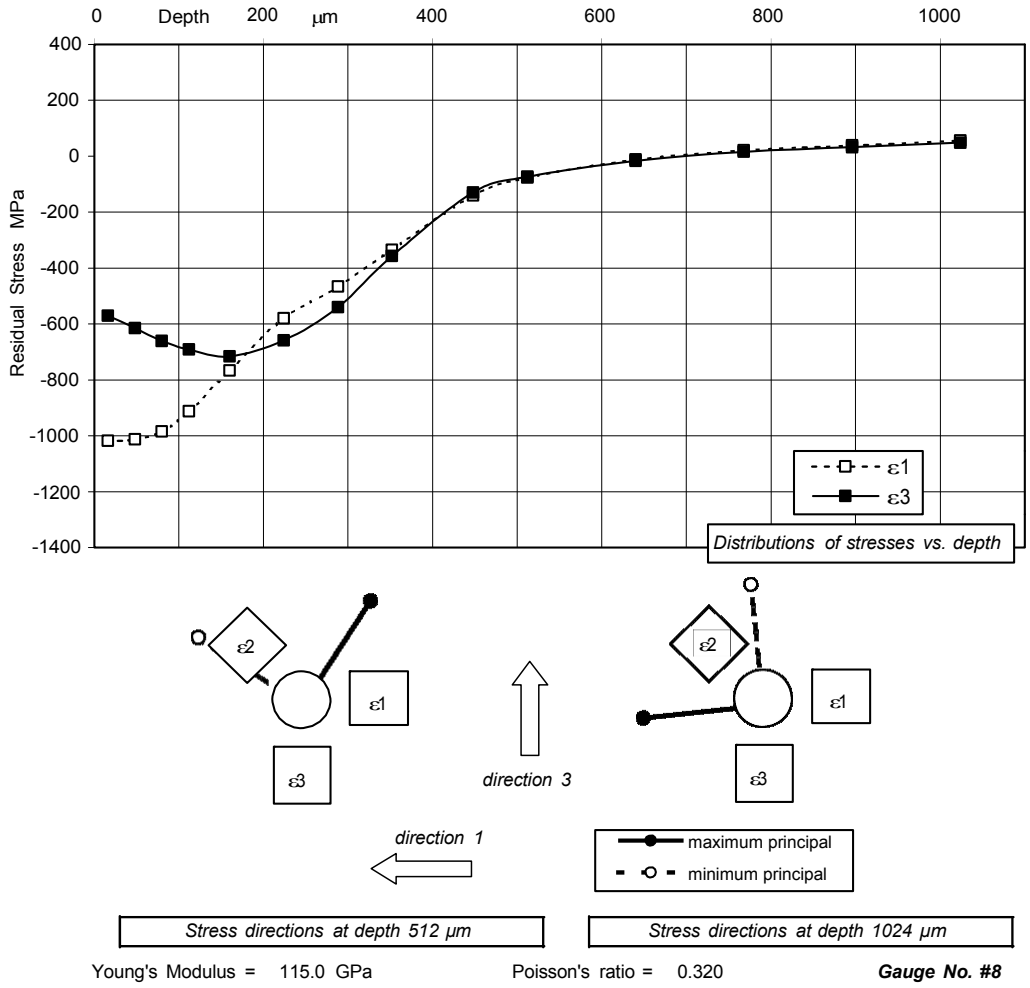

Young's Modulus = 115.0 GPa Poisson's ratio = 0.320 ***Gauge No. #8***

Figure B-8 Residual stress measurement of LPB sample #8

Gauge Type = 062UL Hole diameter = 1.93 mm ***Gauge No. #9***

depth	Relaxed Strains (με)					
	measured			smoothed		
μm	ε1	ε2	ε3	ε1	ε2	ε3
32	27	24	17	31	29	24
64	69	68	62	70	70	65
96	116	121	119	118	122	120
128	170	176	181	172	177	181
192	291	290	308	289	287	305
256	405	392	424	400	388	420
320	499	478	525	492	473	519
384	563	544	600	556	536	591
512	631	615	675	623	606	666
640	667	650	715	664	647	712
768	689	672	742	687	670	740
896	703	685	759	702	684	758
1024	712	693	771	712	692	770
1152	720	698	778	719	697	778
1280	722	700	784	722	700	783
1408	724	701	788			

[Stresscraft RS INT v5.6] *PSW* MAY05

depth	Residual Stresses (MPa)				
	principal		direct		shear
μm	εmax	εmin	ε1	ε3	ε13
16	-604	-725	-719	-610	26
48	-799	-842	-804	-837	14
80	-876	-1002	-876	-1002	-5
112	-890	-1024	-903	-1010	-41
160	-812	-961	-870	-903	-72
224	-647	-790	-712	-725	-71
288	-460	-559	-495	-524	-47
352	-215	-258	-216	-257	-8
448	33	7	25	15	12
512	43	29	40	32	6
640	54	48	54	48	0
768	57	46	54	49	-5
896	60	44	55	49	-7
1024	62	42	55	49	-10

direction 1
direction 3

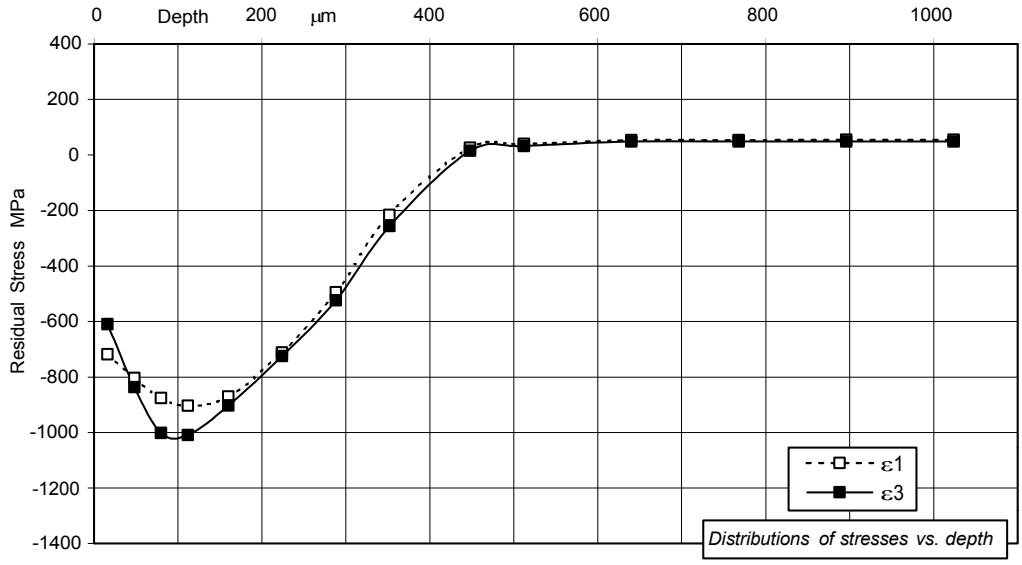

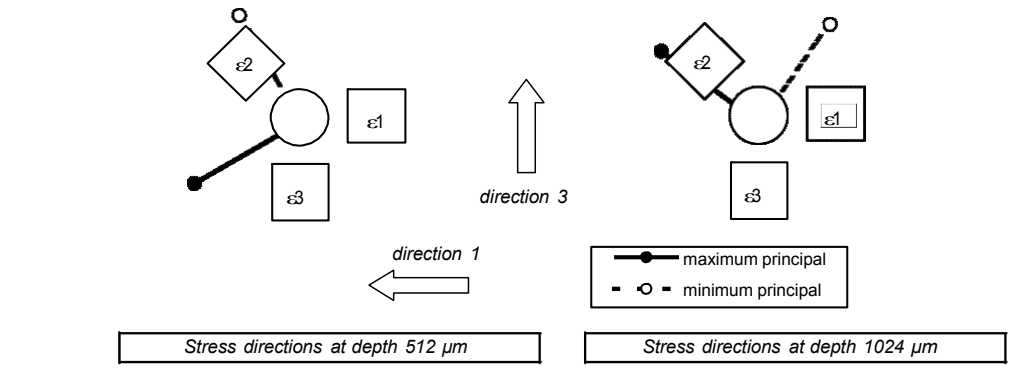

Young's Modulus = 115.0 GPa Poisson's ratio = 0.320 ***Gauge No. #9***

Figure B-9 Residual stress measurement of LPB sample #9

Gauge Type = 062UL Hole diameter = 1.91 mm ***Gauge No. #10***

depth	Relaxed Strains (με)					
	measured			smoothed		
μm	ε1	ε2	ε3	ε1	ε2	ε3
32	17	7	4	23	13	10
64	58	38	32	60	40	34
96	108	78	68	108	79	70
128	158	123	113	159	125	115
192	267	231	222	267	230	221
256	374	333	328	370	329	322
320	463	418	409	457	412	402
384	527	479	462	519	472	455
512	593	541	514	585	534	509
640	626	575	544	624	572	541
768	650	596	562	648	594	561
896	664	610	574	662	609	573
1024	671	619	582	671	619	582
1152	678	626	588	677	625	587
1280	682	630	591	681	629	591
1408	683	632	594			

[Stresscraft RS INT v5.6] *PSW* MAY05

depth	Residual Stresses (MPa)				
	principal		direct		shear
μm	εmax	εmin	ε1	ε3	ε13
16	-287	-529	-515	-301	-57
48	-541	-760	-748	-553	-50
80	-719	-887	-877	-728	-39
112	-804	-869	-861	-812	-22
160	-810	-845	-811	-844	-5
224	-675	-698	-677	-697	-5
288	-451	-484	-483	-452	6
352	-167	-224	-216	-176	21
448	47	12	21	38	15
512	50	26	34	42	11
640	53	40	46	47	6
768	54	43	50	47	5
896	55	44	52	47	5
1024	56	45	54	47	4

direction 1
direction 3

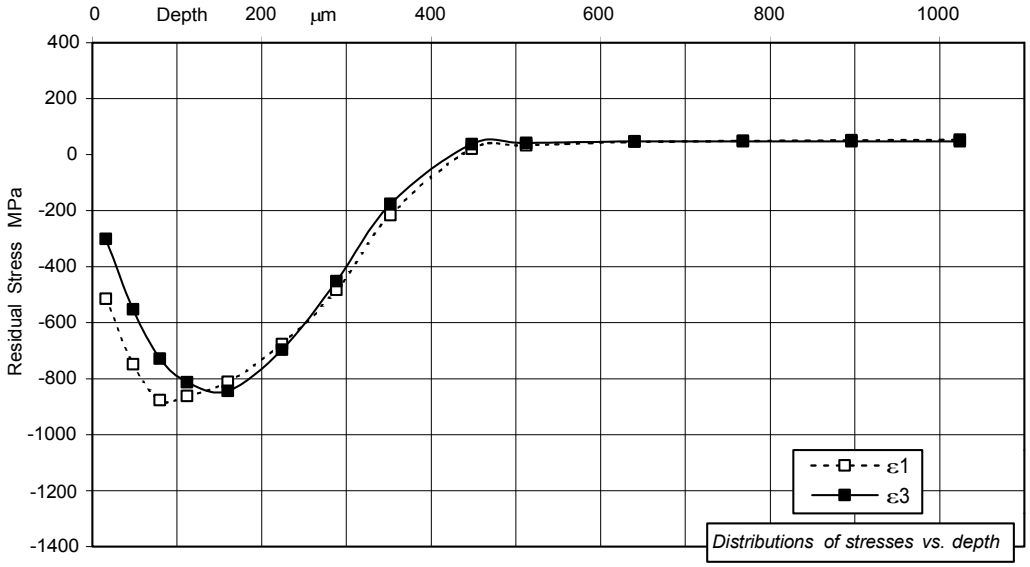

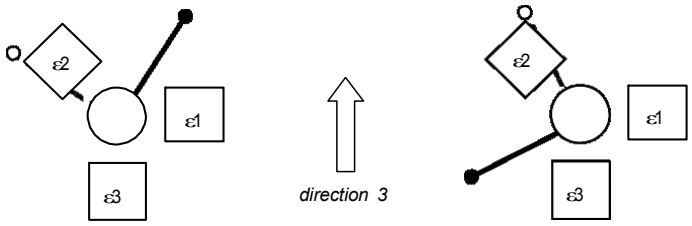

direction 1

maximum principal
minimum principal

Stress directions at depth 512 μm

Stress directions at depth 1024 μm

Young's Modulus = 115.0 GPa Poisson's ratio = 0.320 ***Gauge No. #10***

Figure B-10 Residual stress measurement of LPB sample #10

Gauge Type = 062UL Hole diameter = 1.88 mm **Gauge No. #11**

depth	Relaxed Strains (με)					
	measured			smoothed		
μm	ε1	ε2	ε3	ε1	ε2	ε3
32	22	4	7	27	9	12
64	65	29	33	68	33	37
96	121	69	73	122	71	75
128	181	116	121	181	117	124
192	303	218	237	301	218	239
256	417	321	361	415	318	357
320	521	413	467	515	409	461
384	599	488	549	591	480	540
512	692	575	640	680	564	628
640	737	617	684	733	614	680
768	765	645	712	763	643	709
896	785	664	729	783	663	728
1024	798	677	742	796	676	741
1152	804	685	750	804	685	750
1280	811	692	756	809	691	755
1408	812	695	760			

[Stresscraft RS INT v5.6] *PSW* MAY05

depth	Residual Stresses (MPa)				
	principal		direct		shear
μm	εmax	εmin	ε1	ε3	ε13
16	-283	-718	-632	-369	-174
48	-530	-907	-843	-594	-142
80	-764	-1063	-1017	-809	-107
112	-869	-1081	-1033	-917	-89
160	-857	-1030	-929	-958	-85
224	-742	-894	-777	-859	-64
288	-587	-687	-608	-666	-41
352	-345	-381	-345	-381	2
448	-52	-88	-66	-75	17
512	-5	-38	-18	-25	16
640	42	12	29	25	15
768	50	23	39	35	13
896	54	29	44	40	13
1024	58	35	49	44	12

direction 1
direction 3

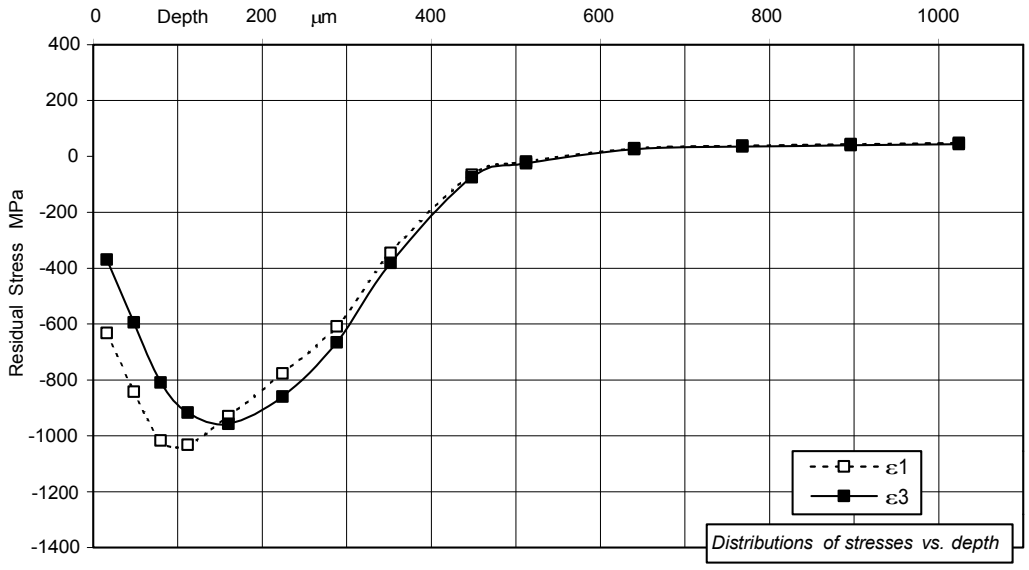

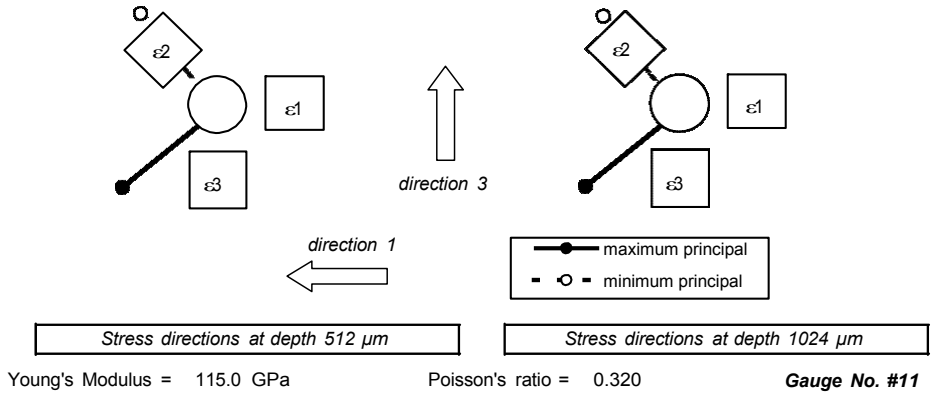

Young's Modulus = 115.0 GPa Poisson's ratio = 0.320 **Gauge No. #11**

Figure B-11 Residual stress measurement of LPB sample #11

Gauge Type = 062UL Hole diameter = 1.91 mm **Gauge No. #12**

depth	Relaxed Strains (με)					
	measured			smoothed		
μm	ε1	ε2	ε3	ε1	ε2	ε3
32	31	13	12	36	20	17
64	83	53	43	86	56	46
96	145	106	84	145	107	85
128	205	162	130	206	164	133
192	332	287	244	329	287	245
256	448	411	363	445	408	359
320	553	522	467	547	516	461
384	634	607	547	626	598	538
512	729	707	637	718	695	626
640	778	757	683	774	752	679
768	809	787	712	806	785	710
896	828	808	732	827	806	731
1024	841	822	747	840	821	746
1152	849	831	756	848	831	755
1280	854	838	762	854	837	761
1408	858	842	766			

[Stresscraft RS INT v5.6] *PSW* MAY05

depth	Residual Stresses (MPa)				
	principal		direct		shear
μm	εmax	εmin	ε1	ε3	ε13
16	-463	-855	-820	-498	-111
48	-659	-971	-967	-662	-31
80	-792	-1054	-1051	-796	29
112	-835	-1010	-996	-849	47
160	-850	-936	-895	-891	43
224	-721	-821	-742	-800	41
288	-563	-640	-580	-623	32
352	-319	-373	-332	-360	23
448	-54	-81	-62	-73	12
512	-18	-33	-20	-30	6
640	21	14	21	14	0
768	33	22	33	22	0
896	40	27	40	27	0
1024	46	31	46	31	0

direction 1
direction 3

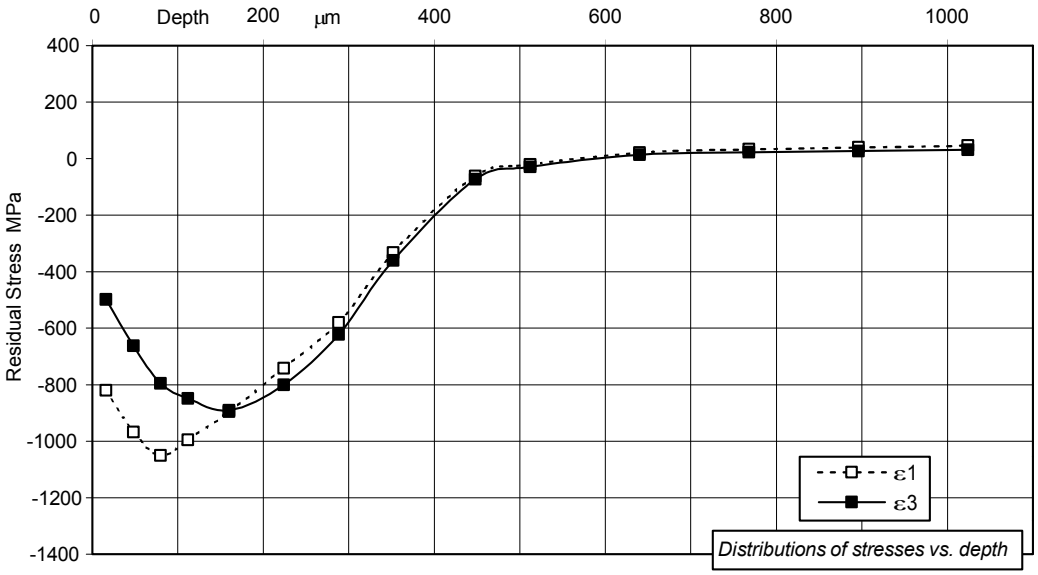

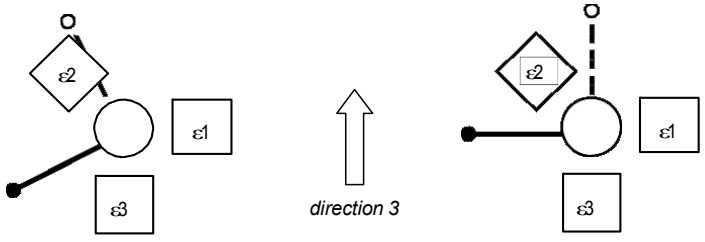

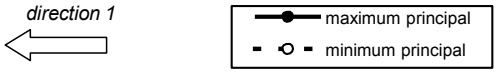

Stress directions at depth 512 μm *Stress directions at depth 1024 μm*

Young's Modulus = 115.0 GPa Poisson's ratio = 0.320 **Gauge No. #12**

Figure B-12 Residual stress measurement of LPB sample #12

Gauge Type = 062UL Hole diameter = 1.91 mm ***Gauge No. #13***

depth	Relaxed Strains (με)					
	measured			smoothed		
μm	ε1	ε2	ε3	ε1	ε2	ε3
32	16	12	14	20	17	20
64	48	45	50	50	47	52
96	86	87	95	88	89	97
128	132	136	146	131	136	146
192	216	230	249	212	226	243
256	283	309	327	275	300	318
320	317	351	368	314	347	364
384	340	378	393	338	376	391
512	370	414	427	368	410	424
640	390	435	447	388	433	445
768	402	448	459	401	447	458
896	408	457	467	408	456	466
1024	412	461	472	412	461	472
1152	415	465	475	415	465	475
1280	417	467	476	415	467	476
1408	414	469	477			

[Stresscraft RS INT v5.6] *PSW* MAY05

depth	Residual Stresses (MPa)				
	principal		direct		shear
μm	εmax	εmin	ε1	ε3	ε13
16	-450	-533	-495	-487	-41
48	-625	-685	-628	-682	-15
80	-740	-829	-741	-828	6
112	-749	-844	-750	-843	11
160	-596	-702	-600	-698	18
224	-343	-427	-358	-412	32
288	-82	-138	-104	-116	28
352	52	22	33	41	15
448	71	57	59	69	5
512	59	47	48	58	3
640	47	37	37	47	1
768	51	45	45	50	2
896	53	48	49	52	2
1024	56	51	54	54	3

direction 1
direction 3

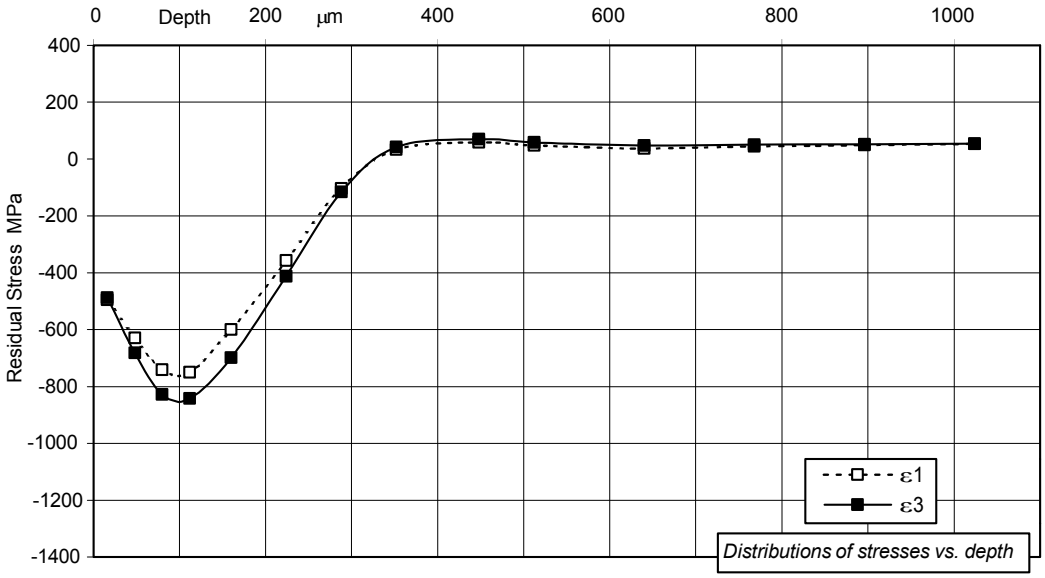

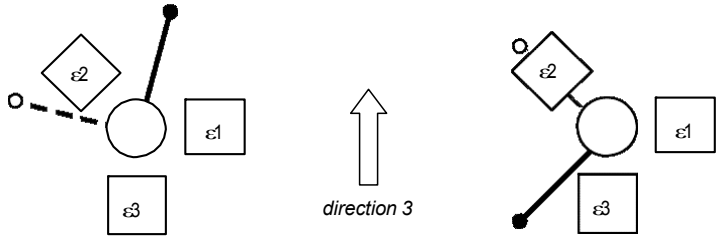

Stress directions at depth 512 μm *Stress directions at depth 1024 μm*

Young's Modulus = 115.0 GPa Poisson's ratio = 0.320 ***Gauge No. #13***

Figure B-13 Residual stress measurement of LPB sample #13

Gauge Type = 062UL Hole diameter = 1.92 mm ***Gauge No. #14***

depth	Relaxed Strains (με)					
	measured			smoothed		
μm	ε1	ε2	ε3	ε1	ε2	ε3
32	15	9	9	20	15	14
64	49	40	38	51	43	41
96	92	82	79	93	83	80
128	137	126	124	136	125	123
192	215	206	205	208	200	198
256	265	261	257	259	255	251
320	291	290	284	290	288	282
384	311	310	303	309	309	302
512	337	338	329	335	336	327
640	353	356	345	351	354	343
768	362	367	354	361	366	353
896	367	374	359	367	374	359
1024	371	380	363	371	379	363
1152	373	383	365	372	383	365
1280	372	384	366	372	384	365
1408	372	385	365			

[Stresscraft RS INT v5.6] *PSW* MAY05

depth	Residual Stresses (MPa)				
	principal		direct		shear
μm	εmax	εmin	ε1	ε3	ε13
16	-354	-476	-462	-368	-39
48	-579	-648	-646	-582	-13
80	-748	-771	-771	-748	-2
112	-720	-733	-720	-732	-3
160	-488	-526	-492	-522	12
224	-221	-269	-234	-256	21
288	-23	-53	-36	-40	15
352	44	35	40	40	5
448	56	49	53	52	4
512	50	41	46	45	5
640	45	33	39	38	6
768	51	38	45	44	7
896	55	40	48	46	7
1024	58	43	51	49	8

direction 1
direction 3

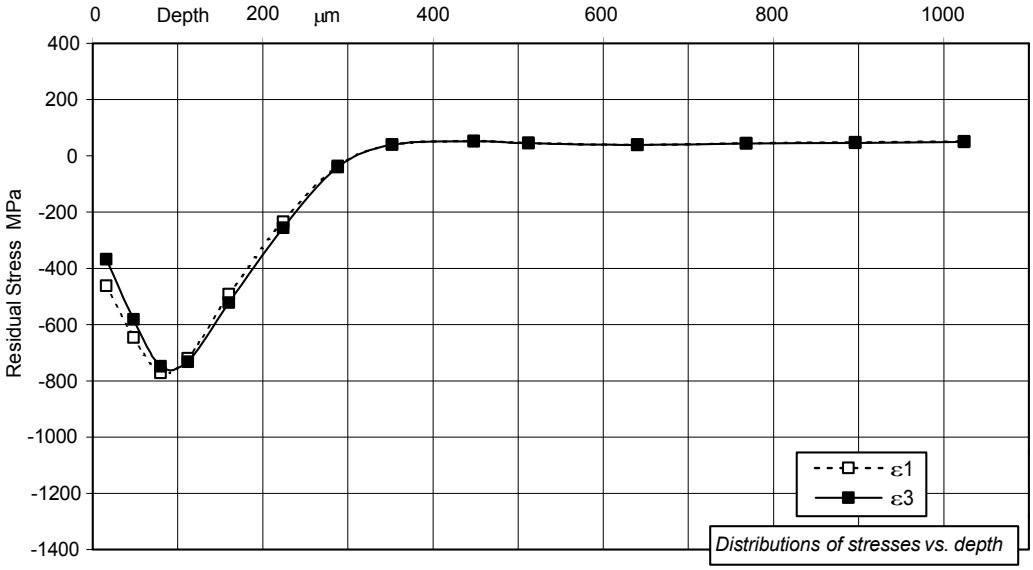

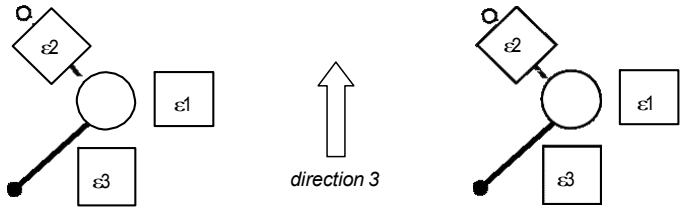

Stress directions at depth 512 μm *Stress directions at depth 1024 μm*

Young's Modulus = 115.0 GPa Poisson's ratio = 0.320 ***Gauge No. #14***

Figure B-14 Residual stress measurement of LPB sample #14

Gauge Type = 062UL Hole diameter = 1.93 mm ***Gauge No. #15***

depth	Relaxed Strains (με)					
	measured			smoothed		
μm	ε1	ε2	ε3	ε1	ε2	ε3
32	13	6	7	18	11	13
64	47	32	37	49	34	40
96	89	66	78	88	66	79
128	128	101	121	126	100	119
192	188	161	193	181	154	184
256	218	192	230	215	189	227
320	235	209	253	235	208	252
384	252	223	270	250	222	269
512	272	244	294	271	243	292
640	289	260	310	287	259	309
768	298	271	321	298	270	320
896	305	278	327	304	278	326
1024	309	284	330	308	283	330
1152	310	286	333	310	286	333
1280	311	288	334	311	290	334
1408	311	296	335			

[Stresscraft RS INT v5.6] *PSW* MAY05

depth	Residual Stresses (MPa)				
	principal		direct		shear
μm	εmax	εmin	ε1	ε3	ε13
16	-291	-461	-421	-332	-73
48	-511	-693	-628	-576	-87
80	-638	-822	-729	-732	-92
112	-570	-715	-612	-672	-66
160	-333	-420	-337	-416	-19
224	-112	-162	-112	-162	1
288	10	-6	9	-6	-1
352	31	28	29	30	1
448	44	27	35	36	8
512	34	17	25	27	8
640	24	7	14	17	8
768	34	13	23	25	11
896	40	16	27	28	12
1024	45	19	31	32	13

direction 1
direction 3

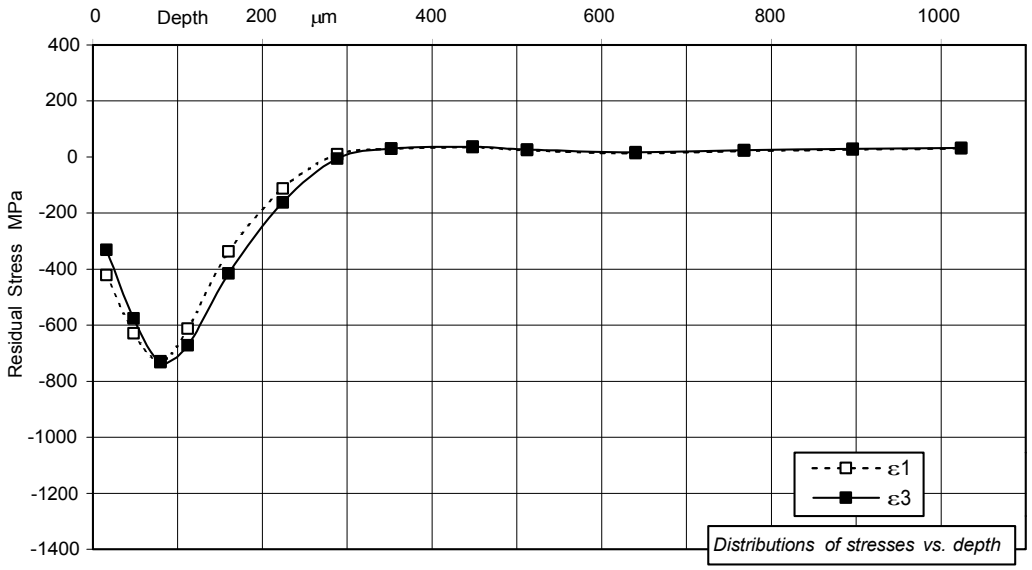

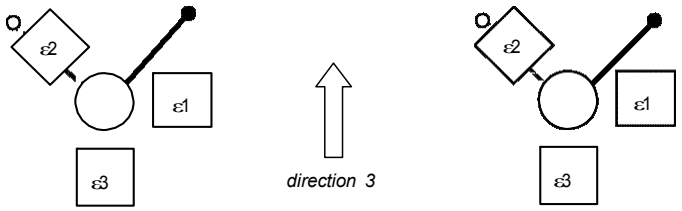

direction 1

maximum principal
minimum principal

Stress directions at depth 512 μm

Stress directions at depth 1024 μm

Young's Modulus = 115.0 GPa Poisson's ratio = 0.320 ***Gauge No. #15***

Figure B-15 Residual stress measurement of LPB sample #15

Gauge Type = 062UL Hole diameter = 1.92 mm ***Gauge No. #16***

depth	Relaxed Strains (με)					
	measured			smoothed		
μm	ε1	ε2	ε3	ε1	ε2	ε3
32	13	7	12	19	13	17
64	51	38	43	54	41	46
96	101	82	85	101	83	86
128	151	130	132	150	129	132
192	241	220	226	236	216	221
256	312	292	298	305	285	290
320	353	334	339	349	330	335
384	379	360	365	377	358	363
512	414	397	402	411	394	399
640	437	422	425	435	420	424
768	452	438	442	451	437	440
896	461	448	452	460	448	451
1024	467	456	458	466	455	458
1152	470	460	462	470	460	461
1280	471	463	463	471	462	463
1408	472	464	464			

[Stresscraft RS INT v5.6] *PSW* MAY05

depth	Residual Stresses (MPa)				
	principal		direct		shear
μm	εmax	εmin	ε1	ε3	ε13
16	-356	-523	-460	-419	-81
48	-598	-734	-710	-622	-51
80	-774	-874	-870	-779	-21
112	-783	-812	-812	-783	-3
160	-604	-637	-605	-637	2
224	-362	-393	-366	-389	11
288	-119	-138	-126	-131	9
352	23	7	18	12	7
448	56	40	53	44	7
512	43	29	40	33	6
640	29	18	26	21	5
768	38	26	35	30	6
896	43	30	39	35	6
1024	48	34	43	40	7

direction 1
direction 3

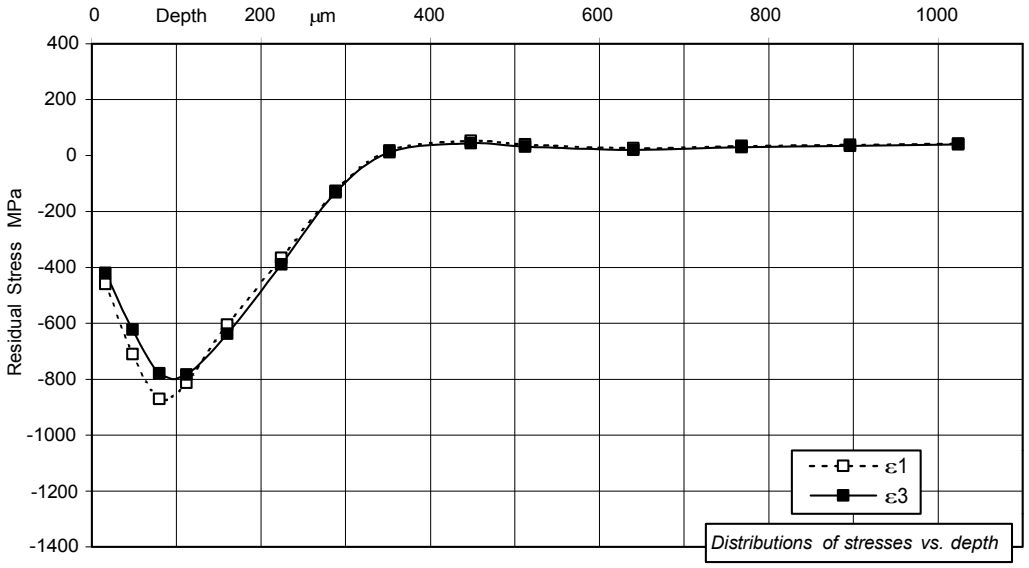

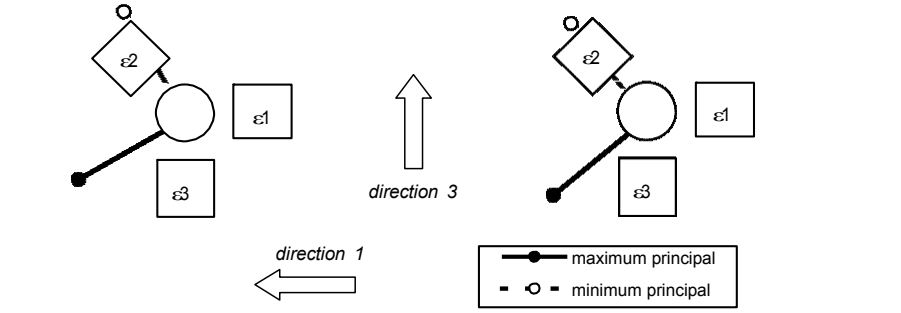

Stress directions at depth 512 μm *Stress directions at depth 1024 μm*

Young's Modulus = 115.0 GPa Poisson's ratio = 0.320 ***Gauge No. #16***

Figure B-16 Residual stress measurement of LPB sample #16